at fixed rotor speed and blade pitch. Note that maximum power, B, does not occur at the maximum power coefficient point, C. At fixed pitch, maximum power occurs in the stall region when the lift coefficient is near its peak value over much of the blade.

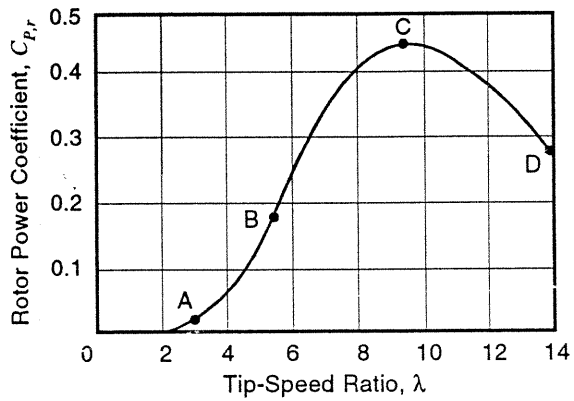

Figure 5-5. Typical plot of rotor power coefficient *vs.* tip-speed ratio for a HAWT with a fixed blade pitch angle.

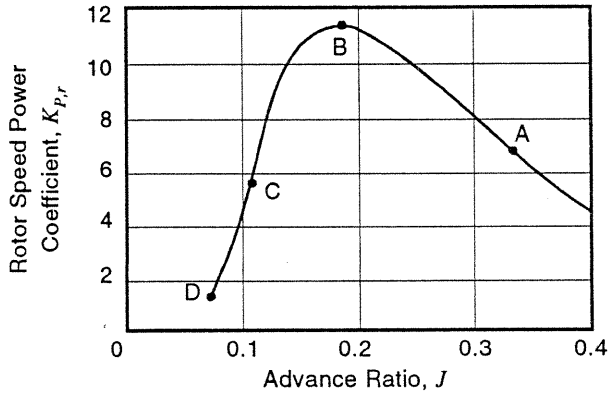

Figure 5-6. Rotor speed power coefficient *vs.* advance ratio for the same HAWT. Operating points A, B, C, and D are the same as in Figure 5-5.

Testing Methods

There are three basic methods of testing wind turbine rotors, each method having its own advantages and disadvantages. *Wind tunnel testing*, the mainstay of the aircraft industry, has been of limited value in wind turbine rotor development, although it is useful for obtaining basic two-dimensional airfoil lift and drag data. While tests in a facility such as the NASA Ames Research Center's *40-ft by 80-ft Wind Tunnel* could provide useful rotor data, financial limits have restricted the size of tunnels that the wind industry can afford. *Scaling* and *blockage* problems occur in most wind turbine tests in wind tunnels. For the test and full-scale *Reynolds Numbers* to be approximately equal, a large test model is wanted (Eq. (2-17)). However, because the rotor wake expands, the *blockage ratio* (swept area/cross-sectional area of the wind tunnel) should be small, preferably less than 1/10.

Tow testing, whereby the wind turbine is pulled or pushed through static air, can relieve the scaling and blockage problems of wind tunnels, but the rotor size is limited. The tow testing of a 15-m diameter wind turbine, for example, would be a formidable task. Tow testing also shares with wind tunnel testing the problem of failing to subject the wind turbine to the unsteady nature of the wind.

Field testing presents the proper wind environment, but it brings new challenges in measuring and recording test data. Field test data acquisition and recording vary with the type of test to be made. For *load tests*, it is desirable to sample the wind at several circumferential stations upwind of the rotor (*e.g.* with an array of anemometers as shown in Fig. 3-25), with time resolution sufficient to distinguish *small-scale turbulence*. Load measurement is made with *strain gages*, using a sampling rate sufficiently fast to determine the *frequency response* of the rotor blades. *Performance tests*, in which the power output of the wind turbine is determined, use time-averaged measurements. Discussion of testing in this chapter focuses on performance data, since loads data are covered in later chapters.

Performance data from wind turbines are stored and plotted using the well-proven *method of bins* [Akins 1978]. Output power and free-stream wind speed are sampled over periods of time, on the order of 5 minutes, and average values for each period are stored in wind-speed "bins." The bins are on the order of 1 m/s in range. The power and wind speed samples in each bin are averaged for plotting. This method greatly smooths the resulting graph of power *vs.* wind speed or the *power curve*.

As a result of using time-averaged data, performance measured by field testing lacks the potential accuracy of wind tunnel or tow testing. At the same time, it contains the response of the turbine to turbulence, wind shear, and terrain features. The *reference wind speed* for performance testing is the wind speed measured at the elevation of the center of the swept area of the rotor. Because a rotor retards the wind flowing through it, the reference wind speed must be measured at a distance upwind, usually a minimum of about 1.5 to 2.0 rotor diameters. Performance test data based on a single reference wind speed measurement is the current industry standard, but two anemometers are usually used for redundancy [ASME 1988].

Annual Energy Output

One of the significant measures of the cost-effectiveness of a wind turbine is its production of energy. In the design and analysis of wind turbines, the *annual energy output* is calculated as illustrated by the flow chart in Figure 4-23. All of the steps in this process (except, possibly, for the prediction of downtime) are normally the responsibility of the aerodynamic specialist. Calculation of annual energy output requires a knowledge of the *wind speed frequency distribution* (probability that the wind speed will be within a given range) and the system power output of each turbine as a function of wind speed. Furthermore, every prediction of annual energy output is site-specific, depending on the local wind flow patterns and turbulence, the number and type of neighboring turbines, and the local air density.

The frequency distribution required is that of the wind speed at the elevation of the center of the rotor's swept area (*hub elevation* in a HAWT or *equatorial elevation* in a VAWT) at the site where the annual energy output is to be determined. When this frequency distribution is obtained from anemometer test data, it is usually expressed in the form of a *histogram*, which gives the number of hours per year that the wind speed is within each given range or *bin*. Bin width is usually 0.5 to 1.0 m/s. System output power as a function of wind speed is also needed, calculated using the *mean air density* at the

selected site. The general equation for calculating *gross annual energy output* (*i.e.* output exclusive of energy consumed for station-keeping, down-time losses, array effects, *etc.*) is

$$AEO_g = \sum_{k=1}^{K} \Delta E_{a,k} = \sum_{k=1}^{K} P_k \Delta t_k \qquad (5\text{-}8)$$

where

AEO_g = gross annual energy output (kWh/y)
k = index of wind speed bin, from 1 to K
$\Delta E_{a,k}$ = gross annual energy output in the kth wind speed bin (kWh/y)
P_k = average power output over the wind speed range ΔU_k (kW)
Δt_k = cumulative time the wind speed at the elevation of the center of the swept area is in the range ΔU_k (h/y)

Table 5-1 illustrates the application of Equation (5-8) using design performance data for the Boeing Mod-2 2.5-MW HAWT [ASME 1988]. Analytical expressions for the system power and for the wind frequency distribution (*e.g.* the single-parameter *Rayleigh distribution* and the two-parameter *Weibull distribution*) can sometimes produce closed-form expressions for annual energy production, but the tabular approach shown in Table 5-1 recommended because of its clarity and flexibility. The accuracy obtained in representing actual power curves and wind distributions by analytical expressions is often poor.

Table 5-1. Typical Calculation of Gross Annual Energy Output [ASME 1988]

Bin k	Wind speed range ΔU_k (m/s)	Duration Δt_k (h/y)	Power output [1] P_k (kW)	Energy output $\Delta E_{a,k}$ (MWh/y)
1	0.0 - 6.25	2,147	0	0
2	6.25 - 6.75	416	175	73
3	6.75 - 7.25	440	318	140
4	7.25 - 7.75	458	460	211
5	7.75 - 8.25	468	603	282
6	8.25 - 8.75	470	745	350
7	8.75 - 9.25	466	949	442
8	9.25 - 9.75	453	1,153	522
9	9.75 - 10.25	435	1,316	572
10	10.25 - 10.75	410	1,479	606
11	10.75 - 11.25	381	1,642	626
12	11.25 - 11.75	349	1,805	630
13	11.75 - 12.25	314	1,968	618
14	12.25 - 12.75	278	2,120	589
15	12.75 - 13.25	242	2,263	548
16	13.25 - 13.75	208	2,385	496
17	13.75 - 14.25	175	2,500	438
18	14.25 - 22.40	648	2,500	1,620
19	>22.40	2	0	0
	Totals:	8,760		8,763

AEO_g = 8,763 MWh/y

[1] at an air density of 1.15 kg/m^3

Actuator Disk Theory for Horizontal-Axis Wind Turbines

The simplest aerodynamic model of a HAWT is the *actuator disk model*, in which the rotor becomes a homogeneous disk that removes energy from the wind. Originated by Rankine [1895], the actuator disk concept was motivated by the development of the marine propeller. The actuator disk provides a rational basis for illustrating that the flow velocity at the rotor is different from the free-stream velocity. However well the actuator disk theory provides an understanding of the flow field, this theory fails to provide a link between rotor geometry and rotor performance.

Rankine-Froude Theory

The *axial momentum theory* [Rankine 1865, W. Froude 1878, R. Froude 1889] idealizes flow through the rotor of a wind turbine as shown in Figure 5-7. The free-stream wind speed is U, which is slowed by the wind device. Applying requirements for continuity, momentum balance, and energy balance to the flow, we may determine the *thrust* and *power* if the flow is assumed to be entirely *axial*, with no rotational motion. Two expressions for thrust may be obtained. First, from the momentum theorem, the thrust is

$$T = \dot{M}_a (U - V_1) = \rho A V (U - V_1) \qquad (5\text{-}9)$$

where T = thrust force on the disk (N)
$\dot{M}_a$ = air mass flow rate through the disk (kg/s)
V = wind velocity at the disk (m/s)
V_1 = wind velocity in the far wake (m/s)

Second, from consideration of the pressure drop caused by the wind machine,

$$T = A(p_u - p_d) \qquad (5\text{-}10)$$

where p_u, p_d = pressures upwind and downwind of the disk, respectively (N/m^2)

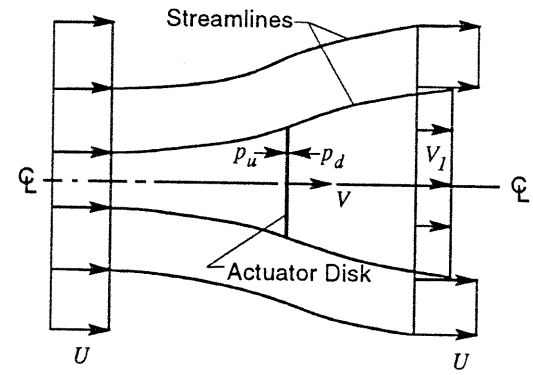

Figure 5-7. Idealized flow through a wind turbine represented by a non-rotating, actuator disk.

Now, the *Bernoulli equation* may be used between the free-stream and the upwind side of the turbine and again between the downwind side of the turbine and the far wake, so that Equation (5-10) becomes

$$T = 0.5\,\rho A\,(U^2 - V_1^2) \tag{5-11}$$

Combining Equations (5-9) and (5-11) we obtain

$$V = 0.5\,(U + V_1) \tag{5-12}$$

Thus, the wind velocity at the disk is the average of the free-stream and far-wake velocities, so the total velocity change from free-stream to far-wake is twice the change from free-stream to the disk. Let

$$U - V = a\,U \tag{5-13a}$$

Then

$$U - V_1 = 2\,a\,U \tag{5-13b}$$

The term a is known as the *axial induction factor* (or the *retardation factor*) and is a measure of the influence of the turbine on the wind. Because the minimum far-wake velocity is zero, the maximum value of the axial induction factor is 0.5. The thrust is not of immediate importance, but the power is. From the *first law of thermodynamics*, assuming isothermal flow and ambient pressure in the far wake, power is equal to

$$P = 0.5\rho A(U^2 - V_1^2)V = 0.5\rho A V(U + V_1)(U - V_1) \tag{5-14}$$

Combining Equations (5-13) and (5-14), the power coefficient for the actuator disk, according to the Rankine-Froude theory, is

$$C_P = \frac{P}{0.5\rho U^3 A} = 4a(1 - a)^2 \tag{5-15a}$$

which has a maximum when $a = 1/3$. Thus

$$C_{P,\max} = (16/27) = 0.593 \tag{5-15b}$$

When examining Equation (5-15a), note that the denominator is the kinetic energy of the free-stream wind contained in a *streamtube* with an area equal to the disk area. However, Equation (5-15b) does not represent maximum *efficiency* (power output/power input), since the mass flow rate through the disk is not ρAU but ρAV. Instead,

$$\eta_d = \frac{P}{0.5\rho U^2 V A} = 4a(1 - a) \tag{5-16}$$

where η_d = actuator disk efficiency.

The maximum efficiency is 100 percent at $a = 0.5$, which yields a power coefficient of 0.5. The disk efficiency is 88.8 percent at the maximum power coefficient of 0.593.

General Momentum Theory with Wake Rotation

Further idealized-flow modeling can be accomplished with the additional consideration of wake rotation. While the initial free-stream wind is not rotational, interaction with a rotating wind machine will cause the wake to rotate. In the case of a propeller, the wake rotates in the same direction as the blades. In the case of an energy-extracting device (such as a HAWT), the wake rotates in the opposite direction. If there is rotational kinetic energy in the wake in addition to translational kinetic energy, we may expect (from thermodynamic considerations) less power extraction than if the wake has translational kinetic energy only.

Joukowski [1918] considered the effect of wake rotation in the analysis of propellers. Adopting his notation to the analysis of wind turbines, the effect of wake rotation on power removal may be estimated. Using a streamtube analysis, equations can be written that express the relation between the wake velocities (both axial and rotational) and the corresponding wind velocities at the rotor disk. In addition, for certain special cases, an expression for the power coefficient can be obtained. The main outcome of this approach is a measure of the effects of rotation on the relative values of the induced (retarded) velocities at the rotor and in the wake.

Figure 5-8 illustrates the geometry of the *streamtube model* of wind flow through a HAWT. Assuming fluid drag is zero, the resulting equations are

Continuity:
$$V\,r\,dr = V_1\,r_1\,dr_1 \tag{5-17a}$$

Moment of momentum:
$$r^2\,\omega = r_1^2\,\omega_1 \tag{5-17b}$$

Energy:
$$0.5\,(U - V_1)^2 = \left(\frac{\Omega + \omega_1/2}{V_1} - \frac{\Omega + \omega/2}{V}\right) V_1\,\omega_1\,r_1 2 \tag{5-17c}$$

where

r, r_1 = radial coordinates at the rotor and at the far wake, respectively (m)
dr, dr_1 = radial thickness of the streamtube at rotor and far wake, respectively (m)
ω, ω_1 = angular velocity in the fluid at rotor and far wake, respectively (rad/s)

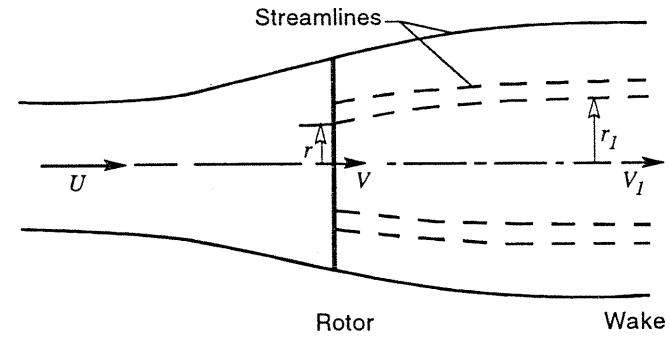

Figure 5-8. Geometry of the streamtube model of flow through a HAWT rotor.

Finally, an expression for the radial gradient in axial velocity may be obtained from Euler's equation:

$$\frac{d}{dr_1}\left(\frac{U^2 - V_1^2}{2}\right) = (\Omega + \omega_1)\frac{d}{dr_1}(\omega_1 r_1^2) \qquad (5\text{-}17d)$$

These four equations may be used to obtain the relationships among thrust, torque, and flow in the wake. Closure cannot be obtained without specification of one of the variables, say ω. When this is done, the flow is found to have the following features:

-- The pressure varies across the wake due to the rotational velocity.
-- The rotor and wake axial velocities vary radially.
-- The angular velocity of the fluid, which is opposite in direction to the rotation of the rotor, changes discontinuously at the rotor.

In the expression for the wake radial velocity gradient, Equation (5-17d), let us assume that $r^2\omega$ is constant (*i.e.*, the rotor wake is an *irrotational vortex*). Then, the wake axial velocity is constant along a radius, because this equation's right-hand-side is zero. Defining

$$V = U(1 - a) \qquad (5\text{-}18a)$$
$$V_1 = U(1 - b) \qquad (5\text{-}18b)$$

where a = axial induction (retardation) factor at the disk
b = axial induction (retardation) factor at the far-wake

We may obtain from Equation (5-17c)

$$a = \frac{b}{2}\left[1 - \frac{(1 - a)b^2}{4\lambda^2(b - a)}\right] \qquad (5\text{-}19a)$$

where, as before, λ is the tip-speed ratio. The power coefficient is given by

$$C_P = \frac{b^2(1 - a)^2}{b - a}$$

Examination of Equation (5-19a) shows that the axial velocity reduction at the disk is always approximately one-half the reduction in the far-wake for tip-speed ratios above 2, which is the same result reached when wake rotation was neglected. The above equation for the power coefficient requires some modification, since the assumption that $r^2\omega$ is constant produces infinite velocities near the axis. In lieu of an irrotational vortex wake, we may substitute a *Rankine vortex wake*, which contains a rotational core with a constant angular velocity equal to the maximum specified for the rotor. This leads to

$$C_P = \frac{b(1 - a)^2}{b - a}[b + (2a - b)\Omega/\omega_{max}] \qquad (5\text{-}19b)$$

where ω_{max} = angular velocity of the wake core (rad/s)

The maximum power coefficient for a rotor with a Rankine vortex wake is shown in Figure 5-9. As would be expected, the power coefficient is insensitive to ω_{max} at high tip-speed ratios, where the torque and consequently the wake rotation are the least.

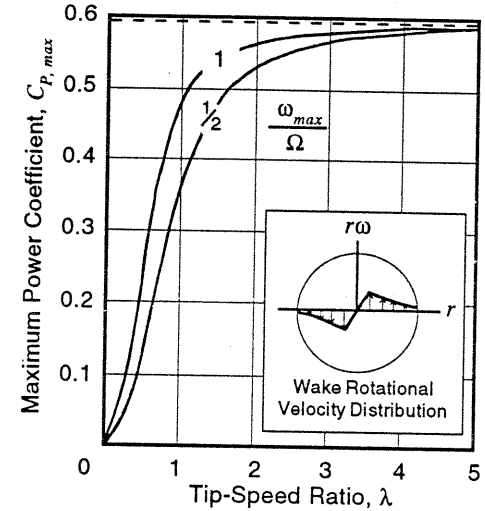

Figure 5-9. Maximum power coefficient for a HAWT rotor with a Rankine vortex wake, as a function of tip-speed ratio and the wake core rotational velocity.

Optimum Actuator Disk Theory

Glauert [1935] developed a simple model for the optimum HAWT rotor. The approach used is to treat the rotor as a rotating actuator disk (*i.e.*, a rotor with an infinite number of blades) and set up an integral for the power. The power integral is made stationary subject to an energy constraint and yields the maximum power output for a given tip-speed ratio. The power extracted from a streamtube (Fig. 5-8) is given by

$$dP = \Omega\, dQ = \Omega\, r\, \rho\, V(r\omega)(2\pi r\, dr) \qquad (5\text{-}20)$$

where dP = increment of power extracted from the streamtube (W)
Q = rotor torque (N-m)
dQ = increment of rotor torque extracted from the streamtube (N-m)

The first term in parenthesis is the gradient in tangential velocity, and the second term in parenthesis is the streamtube annulus area. The power coefficient equations may be written

$$C_P = \frac{8}{\lambda^2}\int_0^{\lambda}(1 - a)\, a'\, x^3\, dx$$

$$x = r\Omega/V \qquad (5\text{-}21)$$

$$a' = \frac{\omega}{2\Omega}\ ,\ \textit{rotational induction factor}$$

Since this integral for the power involves two dependent variables, another relation is required. This is the *momentum equation*, as follows:

$$a'(1 + a')x^2 = a(1 - a) \tag{5-22}$$

A unique way of illustrating this relation is to consider the velocities at the rotor *plane of rotation* of a HAWT, as shown in Figure 5-10. The flow is assumed to be uniform in annular streamtubes with no circumferential variations. Under these conditions, two-dimensional flow may be assumed. In the absence of drag, the velocity *induced* at the rotor must be caused by lift and, hence, be perpendicular to the relative velocity. Two expressions for the tangent of the angle from the plane of rotation to the relative wind vector may be developed under the condition that the *total* induced velocity is perpendicular to the relative velocity. These are

$$\tan\phi = \frac{(1 - a)U}{(1 + a')r\Omega} = \frac{(1 - a)}{(1 + a')x} \tag{5-23a}$$

$$\tan\phi = \frac{a'r\Omega}{aU} = \frac{a'}{a}x \tag{5-23b}$$

Equating the right-hand-sides of Equations (5-23) also produces Equation (5-22). The *Calculus of Variations* can now be used to solve Equation (5-21) with the constraint of Equation (5-22), obtaining the following relationship between the rotational and axial induction factors:

$$a' = \frac{1 - 3a}{4a - 1} \tag{5-24}$$

so that

$$x = (4a - 1)\sqrt{\frac{1 - a}{1 - 3a}} \tag{5-25}$$

Hence, *1/3 > a > 1/4*. A tabulation of variations in the parameters x, a, a', ϕ, and C_P is given in Table 5-2. Since high-speed rotors easily reach tip-speed ratios of 7 or more, it can be seen that most of an ideal rotor will operate with a = 1/3 and a rotational velocity distribution in the form of an *irrotational vortex*. The power coefficient for various tip-speed ratios is also given in Table 5-2, by equating λ to x. At low tip-speed ratios, power coefficients are low because of the large rotational kinetic energy in the wake. At high tip-speed ratios, the power coefficient approaches 0.593 and the wake rotation approaches zero.

Further information may be obtained from the Glauert optimum disk model using the *blade-element theory*. Blade-element theory equates the thrust on a radial increment of blade of length dr to the momentum change in a flow annulus (streamtube) of area $2\pi rdr$. The blade torque is then equated to the moment of momentum in a similar fashion. As the quantities a and a' are known for each radial position, the relative velocity and the angle ϕ may be determined. Figure 5-10 illustrates the velocities and forces in relation to the blade configuration. Of course, since we have assumed that the drag is zero, the only force that acts on the blade is lift.

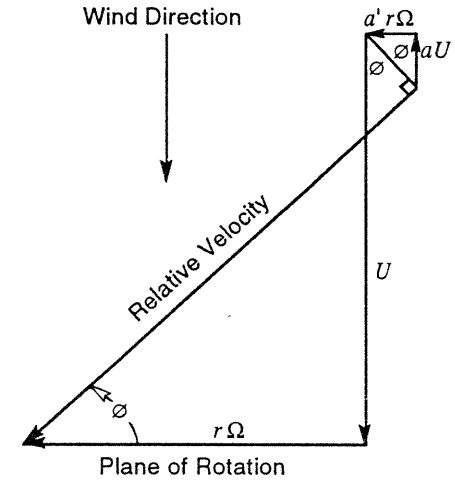

Figure 5-10. Flow velocity diagram at an annulus in a HAWT rotor disk.

Table 5-2.
Flow Conditions and Rotor Parameters for the Glauert Optimum HAWT Rotor

Velocity ratio x	Axial induction factor a	Rotational induction factor a'	Relative inflow angle ϕ (deg)	Rotor power coefficient $C_{P,r}$	Blade-element parameter $Bc\Omega C_L / 2\pi U$
0.25	0.280	1.364	50.6	0.176	0.3658
0.50	0.298	0.543	42.3	0.289	0.5205
0.75	0.310	0.294	35.4	0.364	0.5552
1.00	0.317	0.183	30.0	0.416	0.5359
1.25	0.322	0.124	25.8	0.451	0.4974
1.50	0.324	0.089	22.5	0.477	0.4551
1.75	0.326	0.067	19.8	0.496	0.4151
2.00	0.328	0.052	17.7	0.511	0.3791
2.50	0.330	0.034	14.5	0.532	0.3200
3.00	0.331	0.024	12.3	0.545	0.2750
3.50	0.331	0.018	10.6	0.555	0.2403
4.00	0.332	0.014	9.4	0.562	0.2129
4.50	0.332	0.011	8.4	0.566	0.1909
5.00	0.332	0.009	7.5	0.570	0.1729
5.50	0.332	0.007	6.9	0.573	0.1580
6.00	0.333	0.006	6.3	0.576	0.1453
7.00	0.333	0.004	5.4	0.580	0.1252
8.00	0.333	0.004	4.8	0.582	0.1099
9.00	0.333	0.003	4.2	0.584	0.0979
10.00	0.333	0.002	3.8	0.585	0.0883
11.00	0.333	0.002	3.5	0.586	0.0803
12.00	0.333	0.002	3.2	0.587	0.0737

The incremental thrust, dT, and torque, dQ, acting on an annulus are given by

$$dT = 0.5\,\rho\,V_r^2\,C_L\,c\,B\cos\phi\,dr \tag{5-26a}$$

$$dQ = 0.5\,r\,\rho\,V_r^2\,C_L\,c\,B\sin\phi\,dr \tag{5-26b}$$

where

V_r = relative wind velocity (m/s)
c = blade chord length at radius r (m)
B = number of rotor blades

Assuming that the far-wake axial induction is twice the axial induction at the rotor, momentum expressions yield

$$dT = 4\pi r\rho U^2(1-a)\,a\,dr \tag{5-27a}$$

$$dQ = 4\pi r^3\rho U\Omega(1-a)\,a'\,dr \tag{5-27b}$$

Combining Equations (5-26) and (5-27) then gives

$$\frac{a}{1-a} = \frac{B\,c\,C_L\cos\phi}{8\pi r\sin^2\phi} \tag{5-28a}$$

$$\frac{a'}{1+a'} = \frac{B\,c\,C_L}{8\pi r\cos\phi} \tag{5-28b}$$

Now, a, a', and ϕ are known as functions of x, so a dimensionless blade parameter equal to $(Bc\Omega C_L/2\pi U)$ may be determined. Results are listed in the right-hand column of Table 5-2. Note that an optimum blade for a given tip-speed ratio and constant C_L will have a chord that approaches a maximum at x approximately equal to 0.75.

To illustrate the use of Table 5-2 to determine an optimum blade shape, consider a two-bladed rotor designed to operate at $\lambda = 6$ with $C_L = 0.8$. The left-hand column of the table may be used to determine radial position along the blade, since

$$\frac{r}{R} = \frac{r\Omega/U}{R\Omega/U} = \frac{x}{\lambda} = \frac{x}{6} \tag{5-29a}$$

The required blade chord can be obtained from the right-hand column as follows:

$$\frac{c}{R} = \left(\frac{B\,c\,\Omega\,C_L}{2\pi U}\right)\frac{2\pi}{B\,C_L}\,\frac{U}{R\Omega} = 0.654\left(\frac{B\,c\,\Omega\,C_L}{2\pi U}\right) \tag{5-29b}$$

The required twist angle, β, of the *zero-lift line* (Fig. 5-10) can be obtained from the relationship $\beta = \phi - \alpha$, where α is the angle of attack. Assuming *ideal lift*, for which $C_L = 2\pi \sin\alpha$, the angle of attack is 7.3 degrees for $C_L = 0.8$. Thus

$$\beta = \phi - 7.3° \tag{5-29c}$$

Table 5-3.
Blade Chord and Twist Distribution for an Optimum Two-Bladed HAWT
(Lift coefficient = 0.8 and tip-speed ratio = 6)

Velocity ratio x	Radial position r/R	Chord ratio c/R	Twist angle β (deg)
0.75	0.125	0.363	28.1
1.50	0.250	0.298	15.2
3.00	0.500	0.180	5.0
4.50	0.750	0.125	1.0
6.00	1.000	0.095	-1.0

Thus, although the effects of finite blade number are not included, Table 5-3 gives an indication of the rotor geometry required to achieve maximum C_P at a tip-speed ratio of 6. The blade is noted to have *nonlinear taper and twist*. In order to determine the effects of finite blade number, drag, and operation at other tip-speed ratios, another approach is required.

Flow States

In the previous analysis, it was tacitly assumed that the wind turbine is operating as a power-extraction device that produces a downwind force and retards the free-stream wind speed. This requires that the axial induction factor be between zero and unity. Figure 5-11(a) shows flow patterns or *flow states* and thrust force vectors T associated with a wide range of induction factors [Lock *et al.* 1926, Wilson *et al.* 1976]. A *thrust coefficient*, which can also be used to characterize the different flow states of a rotor, is shown in Figure 5-11(b) as a function of the axial induction factor, and is defined as

$$C_T = \frac{T}{0.5\,\rho\,A\,U^2} \tag{5-30a}$$

By Momentum Theory: $$C_T = 4\,a\,|\,1-a\,| \tag{5-30b}$$

where C_T = rotor thrust coefficient

Wind turbines will normally operate in the *windmill state*, with $0 \le a \le 0.5$. For negative inductions ($a < 0$) it is simple to continue the analysis to show that the device will act as a propulsor producing an upwind force (*i.e.* $C_T < 0$) that adds energy to the wake. This is typical of the *propeller state*.

When a wind turbine rotor operates at tip-speed ratios appreciably above its design value, blade tips may be driven into the *turbulent wake state*. As illustrated by the data in Figure 5-11(b) obtained on wind turbines, autogiros, and helicopters, rotor thrust increases with increasing induction in the turbulent wake state, instead of decreasing as predicted by Equation (5-30b). Thus, momentum theory is considered to be invalid for induction factors larger than about 0.4. Glauert's empirical formula [1926] has been shown to be an acceptable model of rotor thrust behavior for induction factors from 0.4 to 1.0, or, equivalently, $0.96 < C_T < 2.0$ [Dugundji *et al.* 1978].

When the induction factor is somewhat over unity, the flow regime is called the *vortex ring state*, a condition which is experienced by helicopters during powered (slow) descent. A particularly interesting case occurs for axial inductions greater than unity, where the rotor

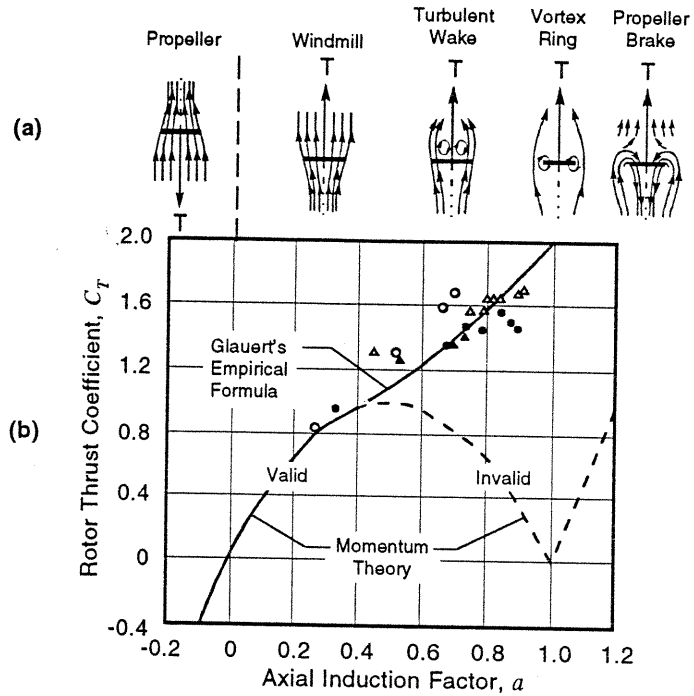

Figure 5-11. Relationship between the axial induction, flow state, and thrust of a rotor. [Lock *et al.* 1926, Wilson *et al.* 1976]

reverses the direction of flow. This may be physically modeled by considering a powered propeller with blades pitched so that they induce a forward flow. This is termed the *propeller brake state*, with power being added to the flow to create downwind thrust on the rotor. Further discussion of wind rotor states is given by Eggleston and Stoddard [1987].

Summary Comments on Actuator Disk Theory

The actuator disk models discussed in this section provide limiting values of rotor performance and a general understanding of the rotor configuration for a particular operating condition. For example, there is a maximum power coefficient of 16/27 for HAWTs, and this limit (called the *Betz* or *Lanchester-Betz* limit) can be approached when the wake rotation is low. Further, we noted that wind turbines operating at high values of induction develop forces that are considerably different from the axial forces predicted by the momentum relation, Equation (5-30). The assumptions of actuator disk theory, particularly the assumption of an infinite number of blades, restrict our understanding of the effect of rotor geometry (*i.e.* blade airfoil section, chord, and twist) on HAWT operation. Additionally, we find that the Betz limit is higher than the power coefficients achieved in practice, because actual rotors (1) have a finite number of blades and (2) are acted upon by drag forces.

Strip Theory for Horizontal-Axis Wind Turbines

In order to bridge the gap between actuator disk models of wind turbines and a rigorous *vortex theory*, an intermediate theory known as *strip theory* has been developed that relates rotor performance to rotor geometry. A particularly important prediction of strip theory is the effect of *finite blade number*. We find that performance-optimized HAWTs do have configurations similar to the Glauert-optimized rotor when finite blade number and drag are included. In the development of strip theory, the relation between the local induction and the local thrust coefficient in each streamtube is of paramount importance.

Background

A HAWT can be considered to be an *airscrew* that extracts kinetic energy from the driving air and converts it into mechanical energy. The similarity of a HAWT to a propeller (which puts energy into the air) enables the same theoretical development used for the propeller to be followed for the HAWT. Propeller theory was developed along two independent approaches: *Actuator disk theory* (which was discussed in the previous section) and *blade-element theory*. The strip theory presented here has been called *modified blade element theory*.

Blade-element theory was originated by Froude [1878] and later developed further by Drzewiecki [1892]. The approach of blade-element theory is opposite that of momentum theory since it is concerned with the forces produced by the blades as a result of the motion of the fluid. It was hampered in its original development by the lack of knowledge of sectional aerodynamics and the mutual interaction of blades. Modern rotor theory has developed from the concept of *free vortices* being shed from the rotating blades. These vortices define a *slipstream* and generate induced velocities. This rigorous theory can be attributed to the works of Lanchester [1907] and Flamm [1909], for the original concept; to Joukowski [1912], for induced velocity analysis; to Betz [1919], for optimization; to Prandtl [1919] and Goldstein [1929], for *circulation distribution* or *tip-loss* analysis; and to Glauert [1922a, 1922b, 1935], Pistolesti [1922], and Kawada [1926], for general improvements.

It has been found that strip-theory approaches are adequate for the analysis of wind machine performance. One reason is that a wind turbine wake expands rather than contracts. At high tip-speed ratios (*i.e.* low *advance ratios*), propellers and helicopter rotors have been observed to shed strong tip vortices. Since these wakes are contracting, the shed vortices are inboard of the tip and interact strongly with the flow through the rotor disk. The resulting radial distribution of aerodynamic forces is found to be appreciably different from that predicted by strip theory. Because most wind turbines operate at high tip-speed ratios, they might be expected to experience the same strong interaction. However, because of the expanding wake, the tip vortex moves outboard of the rotor, negating a strong interaction. From an outboard position, the tip vortex generates induced velocities that decrease local angles of attack and reduce aerodynamic loads.

Various forms of strip theory have been the standard methods of design and design analysis of HAWTs. Strip theories are easy to program, inexpensive to run, and readily adaptable to any size of computer. They are used with modest success to predict output power. However, it is important to note that the largest sources of error in power prediction have been in the airfoil lift and drag data, and these errors are frequently large enough to mask the inaccuracies of the theory.

Flow Model

The foremost assumption in strip theory is that individual *streamtubes* or *strips* (the intersection of a streamtube and the surface swept by the blades) can be analyzed independently of the rest of the flow. Such an assumption works well for cases where the circulation distribution over the blade is relatively uniform, so that most of the vorticity is shed at the blade root and the blade tip. The deployment of *control surfaces*, however, can violate this assumption. For example, the use of *partial-span pitch control* on a HAWT rotor introduces discontinuities in circulation, and appreciable vorticity can be shed near the junction between the inboard blade and the moveable tip. Fortunately, control surfaces are usually deployed to spill excess power at high wind speeds, when the induced velocity is relatively small. Thus, calculation errors that arise when strip theory methods are used to analyze rotors with deployed control surfaces are not usually significant.

A second assumption associated with the development of strip theory is that *spanwise flow* is negligible, and therefore airfoil data taken from two-dimensional section tests are acceptable. Strip theory does not predict any induced flows along the blades. However, when a blade is not perpendicular to the axis of rotation (*e.g.*, when the blade has a *coning angle*) the wind has a component that is directed along the span of the blade. This component is neglected and two-dimensional flow is assumed, adding some error to the airfoil data. A third assumption is that flow conditions do not vary in the circumferential direction. With this assumption, the "strip" to be analyzed is a uniform annular ring centered on the axis of revolution.

Figure 5-12 shows the strip geometry and the coordinate system used. Note that the coordinate s is measured along the blade and r is at right angles to the rotor axis. The wind velocity, U, is assumed to be constant in time and space and aligned with the axis of rotation, so that the *yaw error*, $\Delta\Psi$, is zero. When the rotor blades are coned, the velocity

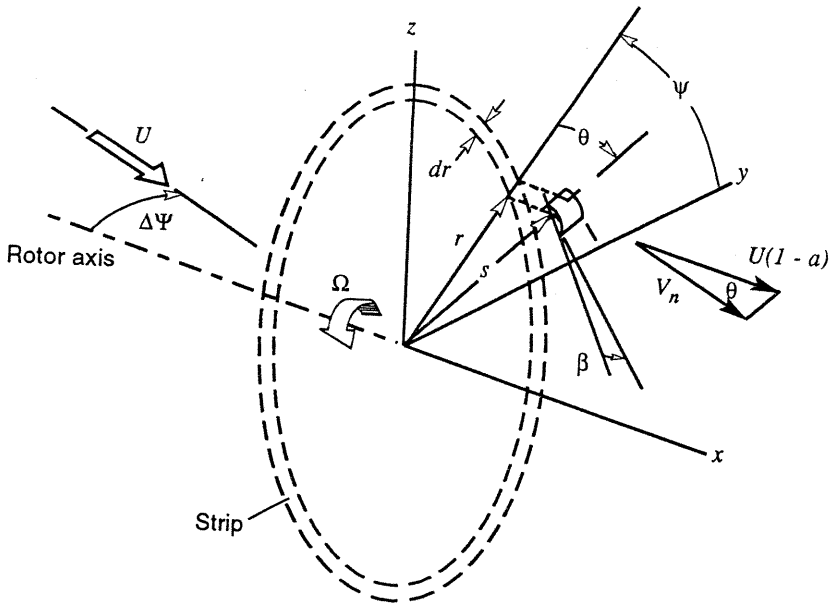

Figure 5-12. Strip geometry and coordinate system.

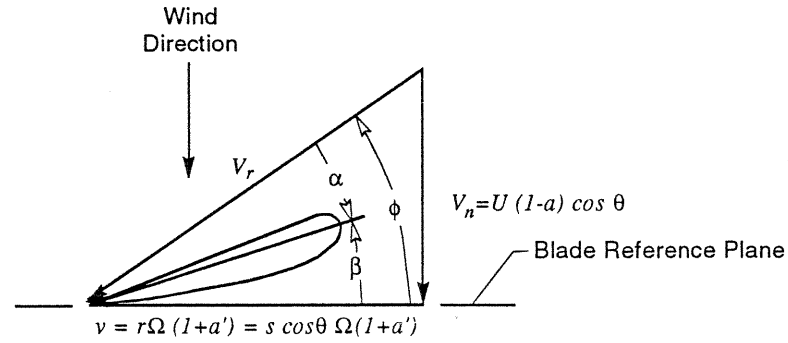

Figure 5-13. Flow velocity diagram at an annulus in a coned HAWT rotor disk.

diagram in Figure 5-10 is altered somewhat, to that shown in Figure 5-13. The wind velocity normal to the blade reference plane, V_n, is equal to the free-stream wind velocity reduced by the axial induction factor, a, and the cosine of the *coning angle*, θ. The cosine of the coning angle also appears in the tangential velocity, v, because the local radial distance to the axis, r, is equal to $s\cos\theta$. In addition, a *drag force, D,* is now included.

Annulus Flow Equations

Momentum and moment of momentum relations are used to obtain equations with which to determine the induced axial and tangential (rotational) velocities. The thrust coefficient in Equation (5-30) can be written for an individual streamtube as follows:

$$C_t = \frac{dT}{0.5\,\rho\,U^2\,(2\,\pi\,r\,dr)} \qquad (5\text{-}31a)$$

$$T = \int_0^R dT$$

where C_t = local value of the thrust coefficient, at radial coordinate r
dT = increment of axial thrust on the blade area within the streamtube (N)

Referring to Figure 5-13, the thrust increment, dT, for a rotor with B blades of chord c is

$$dT = 0.5\,\rho\,V_r^2\,B\,c\,(C_L\cos\phi + C_D\sin\phi)\,dr \qquad (5\text{-}31b)$$

Combining Equations (5-31a) and (5-31b),

$$C_t = \frac{B}{2\,\pi}\left(\frac{c}{r}\right)\left(\frac{V_r}{U}\right)^2 (C_L\cos\phi + C_D\sin\phi)$$

From Figure 5-13, we can express the velocity ratio in terms of the wind angle, ϕ, and the axial induction factor, a, and obtain

$$C_t = \frac{B}{2\pi}\left(\frac{c}{r}\right)(1-a)^2\left(\frac{\cos^2\theta}{\sin^2\phi}\right)(C_L\cos\phi + C_D\sin\phi) \qquad (5\text{-}32a)$$

where θ = coning angle, measured from the plane of rotation (rad)

Turning our attention to the tangential direction, examination of the fluid torque about the axis of rotation for the streamtube and the increment of rotor torque from lift and drag forces on the blade segment within the streamtube, it can be shown that Equation (5-22) is applicable, with a minor change to account for coning, as follows:

$$a'(1+a')x^2 = a(1-a)\cos^2\theta \qquad (5\text{-}32b)$$

Thus, Equations (5-32) are the relations that determine the dimensionless induced velocities a and a'. Before these equations can be used, however, the local thrust coefficient, C_t, must be modified to account for two effects: the departure of the local thrust coefficient from the momentum relation (as discussed in the previous section), and the non-uniformity of the induced velocities in the flow, particularly near its outer edges. These so-called *tip losses* will be discussed first.

The Tip-Loss Factor

Strip theory, as previously developed, does not account for the interaction of shed vorticity with the blade's *bound vorticity*. This effect is usually greatest near the blade tip, although strong vortex interaction can occur at deployed control surfaces. Denoting the *bound circulation* of all the blades by Γ, a *tip-loss factor* F is defined as

$$F = \Gamma/\Gamma_\infty \qquad (5\text{-}33)$$

where Γ_∞ = bound circulation of a rotor with $B \to \infty$ and $c \to 0$ (m^2/s)

Recalling that the induced rotational velocity is directly proportional to the local vorticity intensity, one can give a useful physical interpretation to F, which is that it is equal to the ratio of mean induced velocity in the flow annulus to the induced velocity at the blades.

The flow in the blade tip region significantly affects rotor torque and thrust. Focusing on these rather than the flow field, we can account for the diminished thrust and torque output of the tip regions by defining an *effective radius* of the rotor, which is about 3% smaller than the tip radius. In this empirical approach, we set

$$\begin{aligned} &F = 1 \quad \text{if} \quad 0 < r < r_e \\ &F = 0 \quad \text{if} \quad r_e \le r \le R \\ &r_e \approx 0.97R \end{aligned} \qquad (5\text{-}34)$$

and the interaction between shed and bound vorticity is like a light switch: either on or off.

Propeller development in the 1920s called for better flow models, and the behavior of the wake of the *optimum propeller* resulted in the development of two tip-loss models. The optimum propeller, as conceived by Betz [1919], has a *shed vortex sheet* that appears to move like a rigid body as it is convected away from the rotor. Prandtl [1919] noted that the flow at the edges of the Betz wake appeared to be like the flow over an infinite stack of round, parallel plates. He developed a simple and ingenious approximation for F expressed solely in terms of local flow parameters. While the Prandtl model was useful, questions as to its accuracy remained. Goldstein solved the problem of the flow about a lightly-loaded optimum rotor (with a constant wake diameter), and this "exact" solution was used as a test of the accuracy of the Prandtl model. Comparison showed that the Prandtl model gave results very close to the Goldstein solution at high tip-speed ratios, and qualitative agreement at all tip-speed ratios.

Comparisons between the Betz and Prandtl tip-loss models have been made for wind turbines [Wilson and Lissaman 1974], and agreement was also good. However, since an expanding wind turbine wake is different from the constant-diameter wake of an optimum propeller, it is not apparent which model is more accurate. In the absence of test data on local flow quantities near HAWT blade tips, the Prandtl tip-loss model is recommended. This recommendation is based on the following:

- The Prandtl model predicts a continuous change in circulation, in qualitative agreement with the behavior of wind turbine rotors.
- Calculations of rotor power and thrust made with the Prandtl model are in good agreement with test data.
- Strip theory calculations made with the Prandtl model show good agreement with calculations made with *free wake vortex theory.*
- The Prandtl model is easier to program and use.

In Prandtl's tip-loss model, the *vortex sheets* generated by the blades are replaced (for purposes of analysis) with a series of parallel planes at a uniform spacing equal to the normal distance between successive vortex sheets at the slipstream boundary. Thus

$$\Delta z = \frac{2\pi R}{B}\sin\phi_R$$

where Δz = axial spacing between planes representing vortex sheets (m)
ϕ_R = angle between relative wind vector and plane of rotation at the tip (rad)

Using this spacing, the expression obtained by Prandtl for the tip-loss factor is

$$F = \frac{2}{\pi}\arccos\left(\exp\left[-\frac{B(R-r)}{2R\sin\phi_R}\right]\right)$$

In practice, Prandtl's expression is modified to be

$$F = \frac{2}{\pi}\arccos\left(\exp\left[-\frac{B(R-r)}{2r\sin\phi}\right]\right) \qquad (5\text{-}35)$$

since, as the tip-loss factor F goes to zero at the tip, the tip flow angle ϕ_R goes to the blade pitch angle at the tip, which may be zero. Equation (5-35) avoids a potential tip singularity and, more significantly, produces good results when compared with theoretical approaches.

The tip-loss factor F enters the determination of the induced flow calculation through the local thrust coefficient, C_t. Recall from Figure 5-11 that the overall thrust coefficient departs from the momentum theory value of $4a(1 - a)$ when a exceeds about 0.4. It has been shown [Wilson and Walker 1984] that the following formulation for the local thrust coefficient compares well with vortex theory calculations and produces good results in the correlation of calculated and measured performance and loads:

$$\begin{aligned} C_t &= 4aF(1-a) && \text{if} \quad a \le a_c \\ C_t &= 4F\left[a_c^2 + (1-2a_c)a\right] && \text{if} \quad a > a_c \\ a_c &\approx 0.2 \end{aligned} \tag{5-36}$$

The second equation is a linear extrapolation of the first from the junction point $a = a_c$. In summary, the set of equations used to determine the induced velocities in accordance with strip theory is composed of Equations (5-23a), (5-32), (5-35), and (5-36).

Cascade Effects on Lift and Drag Coefficients

Lift and drag coefficients, C_L and C_D, are functions of the angle of attack, α, as follows:

$$\begin{aligned} C_L &= C_L[\alpha] \\ C_D &= C_D[\alpha] \\ \alpha &= \phi - \beta + \Delta\alpha_c \end{aligned} \tag{5-37}$$

where $\Delta\alpha_c$ = cascade correction to angle of attack (rad)

At a given radial position on the blades, the circumference can be unrolled and represented as a sequence or *cascade* of airfoils, as shown in Figure 5-14. An expression for the so-called *cascade correction* will be derived using the flow geometry shown in this figure. In the strip theory developed to this point, we have used a *lifting line* approach, where the flow distortions caused by the rotor width and blade thickness are ignored. Near the root of a thick blade, however, flow distortion can be significant.

The distance between the blades is the circumference divided by the number of blades. As the flow traverses the path shown, two distinct effects occur to change the flow pattern from that of the actuator disk which was used to develop strip theory: (1) An increase in tangential velocity occurs between the leading and trailing edges of the airfoil, so that the flow follows a curved path, and (2) the axial component of the flow increases because the *airfoil thickness* reduces the size of the flow path. We will treat these two effects separately, developing the equation

$$\Delta\alpha_c = \Delta\alpha_1 + \Delta\alpha_2 \tag{5-38a}$$

where $\Delta\alpha_1$ = effect of finite airfoil thickness (rad)
$\Delta\alpha_2$ = effect of finite airfoil width (rad)

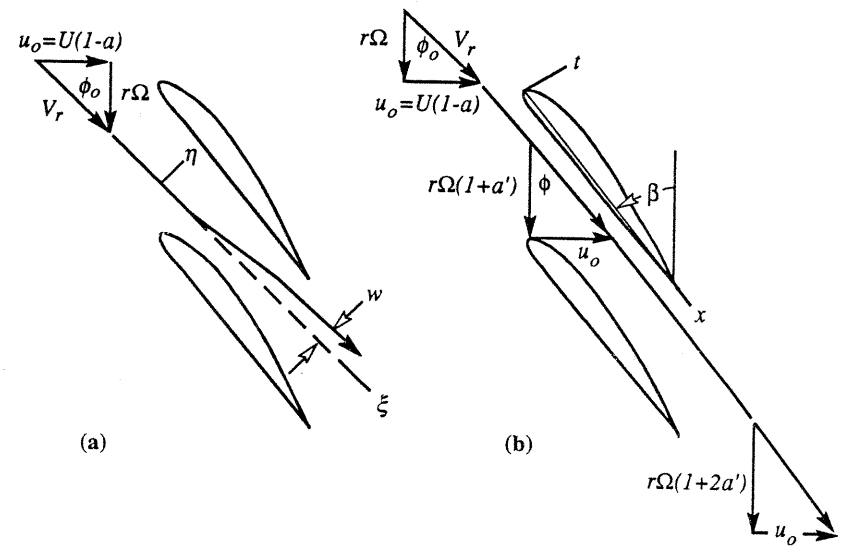

Figure 5-14. Cascade effects on angle of attack. (a) Streamline displacement caused by finite blade thickness (b) Streamline curvature caused by the finite blade width

Because of *blockage* by the blade thickness, axial velocity between the blades is increased, which in turn increases the wind angle, ϕ. This causes flow streamlines to be displaced in a direction normal to the blade chord by an amount w, as shown in Figure 5-14(a). The circumferential spacing between the blades in this figure is greatly reduced for purposes of illustration. The actual spacing-to-chord ratio is large, so we may employ a one-dimensional flow model. Using the requirement for flow continuity, an increment of the displacement, dw, is expressed in terms of the blade thickness as follows:

$$dw = \frac{B\cos\phi_o}{2\pi r}\frac{t}{\cos\alpha}d\xi = \frac{B\cos\phi_o}{2\pi r}t\,dx$$

where ϕ_o = flow angle prior to rotational induction (*i.e.*, $a' = 0$) (rad)
t = local thickness of airfoil, normal to chord line (m)
ξ = coordinate in the direction of the relative wind (m)
x = airfoil chordwise coordinate, measured from leading edge (m)

The flow displacement w causes an increase in the apparent angle of attack of magnitude

$$\Delta\alpha_1 = \frac{w}{c} = \frac{1}{c}\int_0^c\left(\frac{dw}{dx}\right)dx = \frac{B\cos\phi_o}{2\pi r c}\int_0^c t\,dx$$

The latter integral is the airfoil cross-sectional area, A_a. Using the thickness distribution functions for the *NACA four-digit series* of airfoils,

$$A_a \approx 0.68\, c\, t_{max}$$

where t_{max} = maximum thickness of the airfoil (m)

Therefore, the increase in angle of attack caused by the finite thickness of the blades is

$$\Delta\alpha_1 = 0.11\, B \left(\frac{c}{R}\right)\left(\frac{t}{c}\right)_{max} \frac{\lambda}{\sqrt{(1-a)^2 + \left(\frac{r}{R}\right)^2 \lambda^2}} \qquad (5\text{-}38b)$$

The curvature of the flow caused by the finite blade width, illustrated in Figure 5-14(b), results in a change in the circulation developed by the blades. It is assumed that the induced tangential velocity is developed linearly along the blade, from a value of zero at the leading edge to its final value of $2\,a' r\Omega$ at the trailing edge. Note that blade coning is ignored in this development. The change in ϕ from a leading edge to a trailing edge is

$$\Delta\phi = \arctan\left[\frac{(1-a)x}{(1+2a')}\right] - \arctan\left[(1-a)x\right]$$

This change in flow angle occurs in a time period of $\Delta\tau = c/V_r$, so there is an *effective pitch rate* of the blades, $d\beta/dt$. Airfoil pitching is assumed to occur about an axis through the *1/4-chord point*, so the effective change in angle of attack from a finite blade width is

$$\Delta\alpha_2 = \arcsin\left(\frac{\Delta\tau}{4}\frac{d\beta}{dt}\right) \approx \frac{\Delta\phi}{4} \qquad (5\text{-}38c)$$

Note that for the conditions illustrated in Figure 5-14, $\Delta\alpha_1 > 0$ and $\Delta\alpha_2 < 0$.

Gap Correction

Another modification of the strip theory approach is the *gap correction* required to account for the effects of a space along the span of a HAWT blade. Such spaces occur, for example, on blades with *partial-span pitch control*, to accommodate the actuating mechanism. Gaps can effect both lift and drag forces, so corrections are expressed as

$$\Delta C_{P,G} = \Delta C_{P,GL} + \Delta C_{P,GD} \qquad (5\text{-}39a)$$

where $\Delta C_{P,G}$ = total reduction in power coefficient caused by a gap in the airfoil
$\Delta C_{P,GL}$ = reduction in power coefficient caused by the loss of lift in the gap
$\Delta C_{P,GD}$ = reduction in power coefficient caused by the increased drag in the gap

Gap Lift Correction

A gap in the span of the blade causes the circulation to drop to zero locally. As a result, vorticity is shed in the wake, with vorticities of opposite sign being present. That is, the vorticity shed outboard of the gap is of the opposite sign of the vorticity shed inboard of the gap. The effect of this shed vorticity can be modeled as a *semi-infinite vortex doublet* extending downwind of the gap. A linear doublet is employed in lieu of a

helical vortex because the extent of the velocity field of a doublet is smaller. The influence of the doublet falls off inversely as the square of the downwind distance, while the extent of the velocity field of a vortex diminishes inversely with distance.

The local circulation deficit from such a doublet can be calculated by considering its local *downwash* and employing linear aerodynamics. We find that the effect of the gap is approximated by deleting the lift contribution to the power coefficient for a distance along the span of the rotor of

$$s_{g,e} = 2\,c\sqrt{\frac{s_g}{c}}$$

where $s_{g,e}$ = effective spanwise width of the gap (m)
s_g = actual spanwise width of the gap (m)

We can approximate the effect of lost lift by assuming that no power is extracted from the streamtube enclosing the effective width of the gap, which gives

$$\Delta C_{P,GL} = 2\,B\cos^2\theta \left(\frac{r}{R}\right)\left(\frac{c}{R}\right)^2 \sqrt{\frac{s_g}{c}}\,\frac{\lambda}{\pi}\,\frac{V_r}{U}\,C_L(1-a) \qquad (5\text{-}39b)$$

where r and c are the radius and airfoil chord, respectively, at the gap.

Gap Drag Correction

Because no power is extracted from the streamtube containing the gap, the relative velocity causing drag is equal to the local tangential velocity, $r\Omega$. Neglecting the rotational induction factor, the gap drag effect on power coefficient is

$$\Delta C_{P,GD} = \frac{B\,C_{D,g}\,\lambda^3}{\pi}\left(\frac{r}{R}\right)^3\left(\frac{s_g}{R}\right)\left(\frac{t_g}{R}\right)\cos^3\theta \qquad (5\text{-}39c)$$

where $C_{D,g}$ = drag coefficient of the structure in the gap
t_g = average thickness of the structure in the gap (m)

An aerodynamic *fairing* usually covers some or all of the components in the gap, in order to reduce $C_{D,g}$ to a minimum. Otherwise, the lost power could be significant.

Comparison of Strip Theory with Free-Wake Analysis

Two methods of predicting HAWT performance will now be compared. The *strip theory* (modified blade-element theory) approach developed previously is compared with *lifting line, free-wake vortex* calculations performed with the *VORTEX* code, a steady-state analysis developed at the Massachusetts Institute of Technology under sponsorship of the U.S. Department of Energy [Gohard 1978]. The sample cases also offer an opportunity for a controlled comparison of the flow fields predicted by both methods. The rotor configuration for this comparative analysis has two, untwisted, constant-chord blades with a 20% *root cutout* (*i.e.*, no airfoil inboard of $r/R = 0.2$) and no hub interference. The aerodynamic lift

and drag properties of the blade airfoil are simple linear and quadratic functions of the angle of attack, respectively, with approximations for the effects of stall.

Table 5-4 gives rotor thrust and power coefficients calculated using the two analysis methods for four cases that include two tip-speed ratios and three blade pitch angles. Only eight *nodes* (*i.e.*, blade stations) were used in the free-wake analysis, and this does not really warrant reporting the results with three significant figures. Nevertheless, the free-wake calculations do represent the best theoretical predictions currently available of a HAWT flow field. Examination of these results shows that the strip theory predictions of thrust are about one percent lower and predictions of power coefficients are about four percent lower than coefficients calculated using the VORTEX free-wake analysis code.

Table 5-4.
Comparison of HAWT Rotor Coefficients Calculated by Two Analytical Methods

Case	Tip-Speed Ratio, λ	Pitch Angle β (deg)	Thrust Coefficient, C_T		Power Coefficient, C_P	
			Strip Theory [1]	Free-Wake Analysis [2]	Strip Theory	Free-Wake Analysis
1	6.49	0	1.051	1.077	0.421	0.443
2	"	2	0.910	0.920	0.430	0.443
3	"	4	0.758	0.769	0.406	0.422
4	9.52	2	1.036	1.042	0.322	0.338

[1] [Wilson and Walker 1984] [2] [Gohard 1978]

The circulation developed by the blade is a key item associated with the flow field. Figure 5-15 illustrates the circulation distributions along the span of the blade as calculated according to the strip theory and the free-wake methods for Cases 1 and 4. These two cases had similar thrust coefficients but different power coefficients. The graphs show good agreement, with both methods predicting a fairly uniform circulation distribution in both cases. The two methods agree on the circulation in the stalled inboard region in Case 1.

Comparison of Strip Theory with Test Results

Anderson *et al.* [1982] conducted wind tunnel tests of a 3-m diameter HAWT at a variety of wind speeds over a wide range of rotor speeds, with tip-speed ratios from 8 to 14. The rotor had two tapered and twisted blades with an *NACA 4412* airfoil section and a solidity of 4.58%. Test data included local axial and tangential velocities near the rotor, measured using *hot-film anemometry*, and rotor power and thrust. Angles of attack experienced by the blades where below those for stall, so *linear aerodynamics* (*i.e.*, lift coefficient directly proportional to angle of attack) could be employed. *Reynolds numbers*, N_R, for the tests of this turbine at a free-stream wind speed of 10 m/s ranged from 240,000 at a tip-speed ratio of 8 to 420,000 at a tip-speed ratio of 14. (Because of the taper in the blade planform, Reynolds number is almost constant over the outer 70% of these blades.) Lift and drag test data for the NACA 4412 airfoil below stall over this Reynolds-number range have been reported by Jacobs and Sherman [1936].

The turbine tests were performed in a wind tunnel with a blockage ratio of 0.12. Corrections were made to the test data to account for blockage due to wake expansion. At higher tip speeds, blockage corrections were very sensitive to the induction ratio used. This

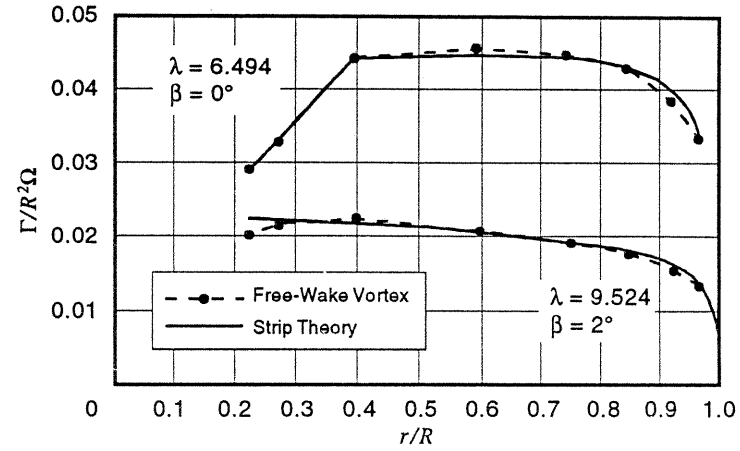

Figure 5-15. Circulation distributions calculated by two different analytical methods. [Wilson and Walker 1984, and Gohard 1978]

was not the case, however, at lower tip speeds. Since the blockage correction has a very large effect at the higher tip-speed ratios, comparison of experimental and theoretical results will be limited to those obtained at a tip-speed ratio of 8. The slope of the lift curve ($dC_l/d\alpha$) was modified by the *Prandtl-Glauert rule* to account for local *Mach number*, which reached 0.26 at this tip-speed ratio.

Figure 5-16 shows the local axial induction factors measured behind the rotor at various radial stations at a tip-speed ratio of 8, compared with factors predicted using modified strip theory. Predicted induction factors show good agreement with test data for the inboard stations out to about 80 percent of the blade's span, but they are higher near the tip. However,

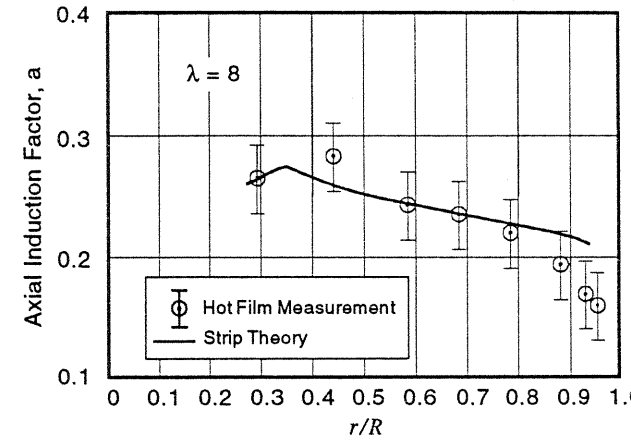

Figure 5-16. Comparison of experimental and theoretical axial induction factors for a 3.5-m, two-bladed HAWT tested in a wind tunnel. [data from Anderson *et al.* 1982]

numerical integration of the local axial induction factors yields an overall rotor thrust coefficient that is consistent with the measured thrust coefficient, as shown in Table 5-5. Differences between measured and predicted power coefficients listed in this table fall within the reported range of experimental error (± 2.5%). On the basis of wind tunnel tests such as these on small-scale HAWTs and field tests of larger turbines, we conclude that performance calculations based on strip theory adequately model test results. The tip loss model at peak power may require further refinement.

Table 5-5.
Comparison of Predicted and Measured Rotor Parameters for a 3-m HAWT [1]

Tip-speed ratio λ	Axial Induction Factor, a [2]		Thrust Coefficient, C_T		Power Coefficient, C_P	
	Strip theory	Wind tunnel test	Strip theory	Wind tunnel test	Strip theory	Wind tunnel test
8.0	0.24	0.23	0.69	0.70	0.44	0.42

[1] Test data from [Anderson *et al.* 1982] [2] Average for 0.25 < r/R < 0.95

Rotor Configuration Effects

A large number of variables exist in the design of a HAWT rotor, including *taper, twist, solidity*, and *number of blades*. As taper and twist are intimately associated with and often controlled by manufacturing techniques, we will consider the aerodynamic effects on performance of only solidity and blade number.

Rotor Solidity and Number of Blades

Solidity, defined as the *total blade planform area* divided by the *swept area* of the rotor is typically less than 0.10 for modern wind turbines. The rotor solidities of the NASA/DOE Mod-0, Mod-1, and Mod-2 two-bladed experimental HAWTs were 0.029, 0.042, and 0.036, respectively, while typical Danish three-bladed HAWTs have solidities between 0.070 and 0.080. (See Chapters 3 and 4 for descriptions of these wind turbines.)

As the solidity of a wind turbine rotor is increased, the tip-speed ratio for maximum power coefficient is reduced. This effect can be explained by considering a rotor of a given solidity at its peak power coefficient and associated tip-speed ratio, producing its optimum axial induction. If the solidity of this rotor is increased and all other parameters are held constant, both lift and drag forces will increase and, as a result, the axial induction factor will increase beyond its optimum value. To restore optimum axial induction, aerodynamic forces on the blade must be decreased, which is accomplished by reducing the tip-speed ratio. Additionally, the *peak power* of a fixed-pitch rotor increases as solidity is increased. These effects of solidity on power and power coefficient occur regardless of whether the solidity is changed by increasing the number of blades or by increasing the chord dimensions of each blade or both.

A different situation occurs when solidity is held constant and the number of blades is changed. In this case, performance changes are caused by two opposing effects, which are the effect of blade *Reynolds number* and the effect of *tip losses*. As the number of blades is increased, chord dimensions decrease (to keep solidity constant), which reduces the

blade's Reynolds number. Rotor power decreases, as a result, since modern wind turbines usually have *turbulent flow* over their blades, which is a regime in which a lower Reynolds number produces lower lift and higher drag. The effect of increasing the number of blades on tip losses is the opposite: Reducing the tip chord dimensions decreases the total tip loss, and rotor power is increased.

Empirical Equation for Maximum Power Coefficient

Because of the many configuration variables that must be considered in the design of a wind turbine rotor, it is often useful to be able to quickly estimate the *maximum* or *peak power coefficient* that can be achieved with a potential rotor configuration. This was done previously for a drag-driven translator (Eq. (5-3)), a lifting translator (Eq. 5-5)), the Rankine-Froude actuator disk (Eq. (5-15b), and the Glauert optimum HAWT rotor (Table 5-2). With the added effects of finite blade number, B, and realistic airfoil lift and drag properties, C_L and C_D, estimates of maximum power coefficient are best done with empirical equations such as the following [Wilson *et al.* 1976]:

$$C_{P,\max} = 0.593\left[\frac{\lambda B^{0.67}}{1.48 + \left(B^{0.67} - 0.04\right)\lambda + 0.0025\lambda^2} - \frac{1.92\lambda^2 B}{1 + 2\lambda B}\,D/L\right] \quad (5\text{-}40)$$

where D/L = ratio of C_D to C_L at the design angle of attack; drag-to-lift ratio

Figure 5-17 illustrates the application of Equation 5-40. The Glauert ideal HAWT performance ($B \rightarrow \infty$ and $D/L = 0$; data from Table 5-2) forms an upper bound.

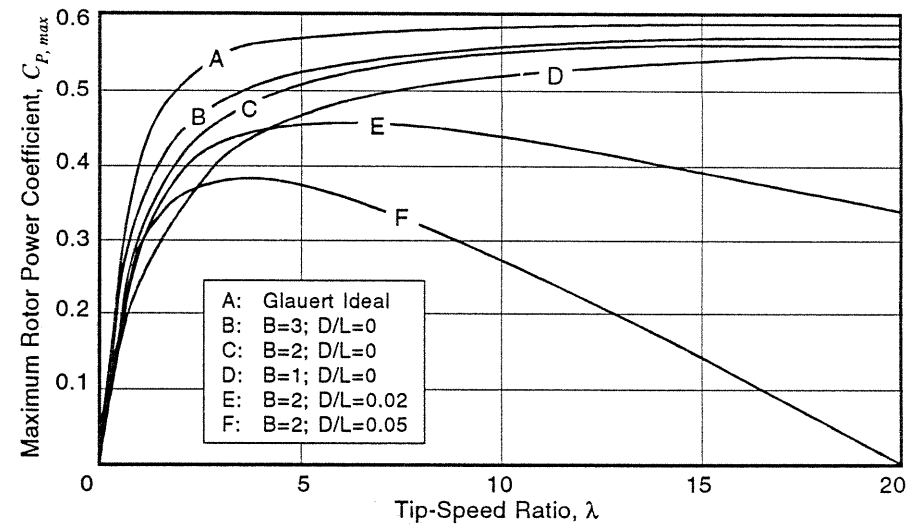

Figure 5-17. Typical effects of the number of blades and the design drag-to-lift ratio on the maximum power coefficient of a HAWT. Equation (5-40); [Wilson *et al.* 1976]

Aerodynamic Behavior of HAWTs in Operation

The operation of modern HAWTs includes a number of important features, such as the use of a *teetered rotor, yaw response, aerodynamic controls, transient aerodynamics,* and *vortex generators*. The aerodynamic qualities of these features are discussed in this section, along with examples of HAWT performance and aerodynamic loads.

Teetered Rotors

The rotor of an operating HAWT is continually subjected to wind conditions that cause significant variations in the local air loads along its blades. These conditions include *wind shear* (vertical and/or horizontal gradients in wind speed), *yaw error* (rotor disk not perpendicular to the wind), *tower shadow* (reduction in wind speed caused by tower blockage), and *small-scale turbulence* (perturbations above and below the mean wind speed over areas smaller than the swept area).

Wind shear, for example, can cause the blade at the topmost position to experience a higher wind speed than the blade closest to the ground. If the blade is held rigidly at the hub, this difference in wind speed will induce a cyclic variation in local angles of attack. As a result, each blade will experience *cyclic flatwise bending* (also called *flapwise* or *out-of-plane* bending), with a dominant frequency of once per rotor revolution or *1P*. Similar cyclic loading at a 1P frequency occurs with yaw error. The effects of tower shadow and turbulence are more complex, causing significant fluctuations in the aerodynamic loading on the blades not only at the *1P* frequency but also at higher harmonic frequencies (*i.e. 2P, 3P, etc.*).

Cyclic flatwise bending moments on the blades of a two-bladed HAWT are greatly reduced by allowing the rotor to oscillate like a see-saw about a *teeter axis* or *teeter hinge* through the outboard end of the turbine shaft, as illustrated in Figure 5-18. The teeter hinge prevents unbalanced out-of-plane aerodynamic loads from being transmitted to the turbine shaft, while still allowing in-plane torque loads to be carried. The effectiveness of teetering in reducing blade bending loads can be shown by the following analysis.

Equilibrium of out-of-plane moments about the teeter axis requires that

$$0 = \int_{-R}^{R} p_{a,x}\, r\, dr - \gamma'' \int_{-R}^{R} m_b r^2\, dr - \gamma \Omega^2 \int_{-R}^{R} m_b r^2\, dr \qquad (5\text{-}41a)$$

where $p_{a,x}$ = axial air pressure loading per unit of blade span (N/m)
m_b = blade mass per unit of span (kg/m)
γ, γ'' = teeter deflection (rad) and acceleration (rad/s^2), respectively

The limits -*R* to *R* indicate that the integration is over both blades. The first term is the net (unbalanced) aerodynamic moment on the rotor, the second is the inertial moment, and the third is the moment of centrifugal forces which oppose the teetering motion. We can analyze the *rigid-body motion* of the rotor by rewriting Equation (5-41a) as an *equation of motion* and setting the aerodynamic forces to zero (*i.e.* teetering in a vacuum), which gives

$$I_{tt}\gamma'' + I_{tt}\Omega^2\gamma = M_{a,net} = 0 \qquad (5\text{-}41b)$$

where I_{tt} = mass moment of inertia of the rotor about the teeter axis (kg-m^2)
$M_{a,net}$ = unbalanced aerodynamic out-of-plane moment on the rotor (N-m)

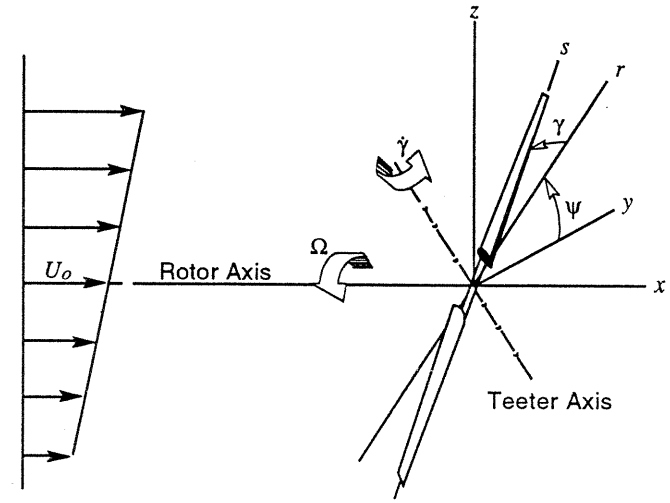

Figure 5-18. Schematic diagram of a teetered, two-bladed HAWT rotor.

Equation (5-41b) describes simple harmonic motion, with a frequency equal to Ω (*1P*), so

$$\gamma = \gamma_1 \sin\Omega t + \gamma_2 \cos\Omega t = \gamma_1 \sin\psi + \gamma_2 \cos\psi \qquad (5\text{-}41c)$$

where γ_1 , γ_2 = teeter amplitudes determined by the wind speed spatial distribution (rad)
ψ = blade azimuth (rad)

Returning to a consideration of air loads, the teeter motion will cause a wind velocity component *opposing the motion*, which can reduce or eliminate variations in wind speed across the rotor. To illustrate this, assume a vertical, linear wind shear gradient. The axial wind velocity, V_x , seen by the teetering blade is

$$V_x = \left(U_0 + \frac{\Delta U}{2R} r \sin\psi\right)(1 - a) - r\Omega(\gamma_1 \cos\psi - \gamma_2 \sin\psi) \qquad (5\text{-}42a)$$

where U_0 = free-stream wind velocity at hub elevation (m/s)
ΔU = vertical change in wind velocity across the rotor diameter (m/s)

Variations in wind speed from U_0 are eliminated at the rotor by a small teetering motion that is 90 degrees out-of-phase with the wind shear gradient, with the component amplitudes

$$\gamma_1 = 0 \qquad \gamma_2 = -\frac{(1 - a)}{2\lambda}\frac{\Delta U}{U} \qquad (5\text{-}42b)$$

In practice, teeter deflections are restrained by *teeter stops* that prevent the blade from hitting the tower during extreme gusts or during starting and stopping. Teetered rotors may also be *coned*, and sometimes the teeter axis is not perpendicular to the blade axis (the angle of inclination is called the δ_3 angle). While these modifications complicate the aerodynamic analysis, the benefits of teetering remain the same: reductions in cyclic loads on the blades and, most importantly, on the nacelle and tower. Analysis of rotor loads must include teeter motion, but mean power output can be determined without including teetering.

Yaw Behavior of HAWT Rotors

All HAWTs operate for some fraction of the time with their rotor axis misaligned with the wind azimuth. It is common for a rotor to encounter yaw angles of 30 deg for periods as long as several minutes. Active-yaw-controlled rotors typically respond to a time-averaged wind direction with averaging times of several minutes. Some free-yaw rotors which have been designed to operate with the rotor downwind of the tower have been observed with the rotor operating upwind of the tower for extended periods. Many HAWTs operate continuously with a small yaw error. Others have experienced high rates of yaw rotation which have caused fatigue failures induced by gyroscopic loadings.

Historically, yaw-related problems have been one of the leading causes of turbine downtime in California wind power stations. These problems are of two types: loss of *yaw stability*, and excessive *yaw-induced loads*. Yaw stability is particularly important for free-yaw HAWTs which rely on aerodynamic forces to achieve proper orientation with respect to the wind. The wind turbines of the 1930s used a tail vane in order to obtain yaw stability. However, a modern free-yaw HAWT, with its rotor downwind of the tower, obtains its yaw stability from the aerodynamic forces on the rotor.

The presence of a yaw error causes changes in the aerodynamic forces normal to and tangential to the airfoils as the blades rotate. In a rigid-hub wind turbine, both the normal and tangential forces can contribute to a moment about the yaw axis. In a HAWT with a teetered rotor, the tangential forces are dominant in producing this yaw moment. A yaw moment arises from blade-to-blade differences in aerodynamic loading. Thus, when making analytical estimates of the yaw moment, greater accuracy is required than in the determination of rotor thrust or rotor torque, because the aerodynamicist must now evaluate small differences between large numbers.

Aerodynamic Analysis of a Yawed Rotor

The aerodynamic behavior of a yawed wind turbine has been examined by Glauert [1935a], Miller [1979], de Vries [1985], and Hansen [1992]. Additionally, a recent, extensive review article by Hansen and Butterfield [1993] contains a discussion of yaw aerodynamics. Aerodynamic analysis of the power extracted from the wind stream by a yawed rotor is complicated by the fact that the wake is skewed, so that wake cross-sections are elliptical rather than round. This modifies the induced velocity at the rotor. Large cyclic changes also occur in blade angles-of-attack because of yaw error, and this has been shown to cause dynamic stall [Hansen 1992]. Yaw moments are particularly sensitive to dynamic stall because of the asymmetry produced by stall hysteresis. Additionally, tower shadow, and wind shear (both vertical and horizontal) are known to contribute to the differential blade loading that causes yaw misalignment.

Glauert's contribution to the aerodynamic analysis of a yawed rotor is expressed as a modification of the momentum equation, Equation (5-9), as follows:

$$dT = 2\,a\,\rho\,U\,U'\,dA$$

$$U' = \sqrt{(U\cos\Delta\Psi - a\,U)^2 + U^2\sin^2\Delta\Psi} \qquad (5\text{-}43)$$

where U' = component of the free-stream wind speed shown in Figure (5-19) (m/s)

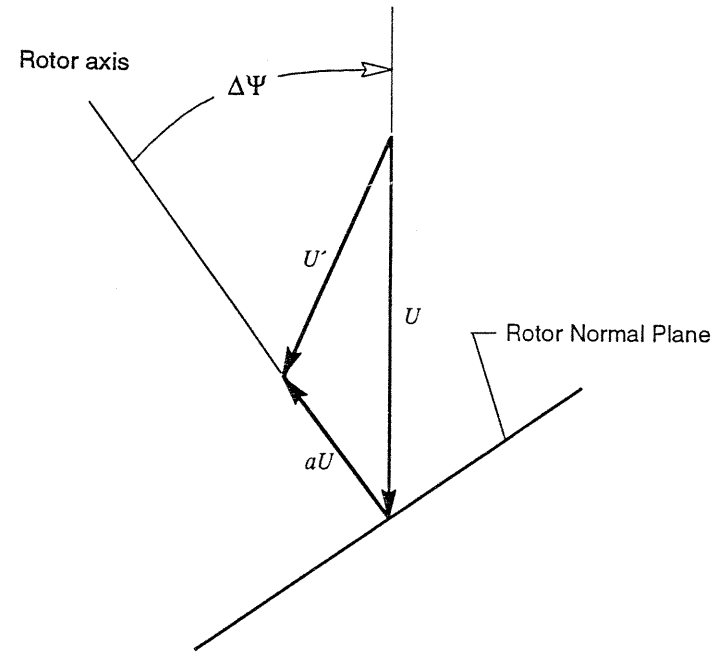

Figure 5-19. The wind velocity component U' in the Glauert modification of the momentum equation accounting for yaw heading error. [Glauert 1935a]

When Equation (5-43) is incorporated into the strip theory which was discussed previously, the loads, yaw motions, and power performance calculated for a free-yaw HAWT (an *ESI-80* machine) agree well with test data [Wilson *et al.* 1994].

Yaw Error and Power Output

It has been observed that even relatively small yaw errors (± 10 deg or less) can reduce the power output of a HAWT significantly. Anderson *et al* [1982] measured the power output of a 3-m, two-bladed HAWT in a wind tunnel at various angles of yaw. The results are shown in Figure 5-20, in the form of ratios of power with yaw error to power without yaw error. Tests were run at three different tip-speed ratios. For comparison, power reductions predicted in accordance with strip theory are also shown in the figure. Generally, strip theory predicts too large a loss in power from yaw error. Performance was

found to vary as the cube of the cosine of the yaw error, which means the effective normal wind speed is $U\cos\Psi$. It should be noted that turbulence can also result in yaw error and a corresponding power loss.

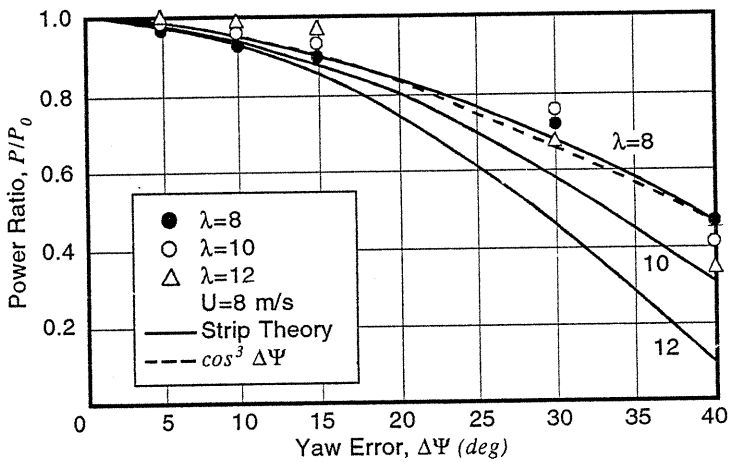

Figure 5-20. Measured and calculated effects of yaw error on the power output of a 3-m HAWT. Test data from [Anderson *et al.* 1982]

Aerodynamic Controls

The operation of a HAWT involves starting the wind turbine from rest, stopping the wind turbine under a wide range of normal and abnormal conditions, and modulating system power and loads while the turbine is running. The starting of many current wind turbines is accomplished by running the generator as a motor. For large-scale HAWTs aerodynamic control surfaces are employed to assist in delivering the large *starting torques* needed. *Loss-of-load emergencies* and wind speeds above the operating range require a reliable means of stopping the turbine. Aerodynamic controls are particularly attractive for stopping the rotor, and almost all current HAWTs employ some type of aerodynamic control to prevent *rotor overspeed.* A third control function, that of regulating power output and/or system loads, has been accomplished historically by use of aerodynamic control surfaces.

Full-Span Blade Pitch Control

First on the list of aerodynamic controls is full-span blade pitch control. Figure 5-21 shows a typical blade pitch angle schedule required to produce a *ramp-plateau power curve.* The power plateau, at the turbine's *rated power*, has the advantage of restricting the power and loads at high wind speeds to cost-effective levels. The ramp portion of this power curve represents operations at below-rated wind speeds, during which blade pitch is usually held constant. The control systems in some HAWTs change pitch angle slightly along the ramp (either continuously or by a mid-ramp change) in order to optimize energy capture. In practice, the blade pitch changes required at the "knee" of the power curve represent a problem area, particularly under gusty wind conditions that can cause power "spikes," since the sharp change in the power curve is accomplished by corresponding sharp changes in the blade pitch rate. Control strategies are often used that "round off" these sharp knees.

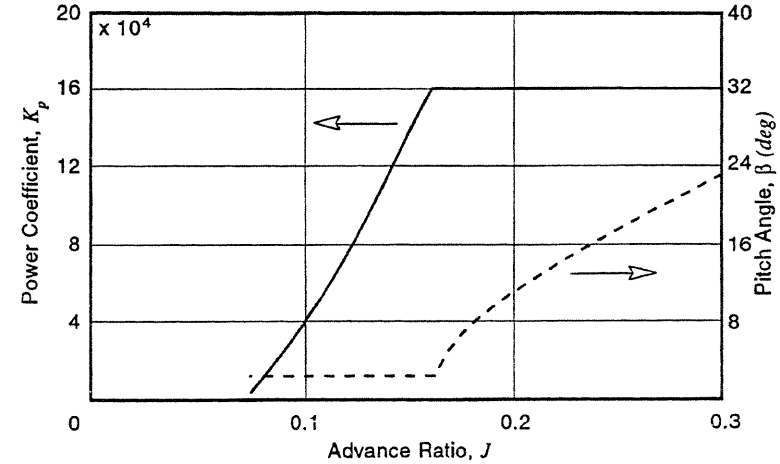

Figure 5-21. Dimensionless power curve and associated full-blade pitch angles for a typical HAWT. Blade pitch is held constant until rated power is produced.

Partial-Span Pitch Control

Pitching the entire blade requires large bearings and substantial actuators, both of which tend to increase rotor weight and cost. One approach that retains the advantages of full-span blade-pitch control and yet decreases the complexity of the hub is partial-span pitch control. This is particularly advantageous for a teetered rotor, permitting designers to separate the teeter-axis bearings and supporting structure from the pitch-axis bearings and pitch actuators. The multimegawatt Boeing Mod-2 and Mod-5B HAWTs (Figs. 3-39 and 4-5) are two examples of turbines with partial-span blade pitch control for starting, power regulation, and stopping. Typically, only the outer third of the blade span is pitched on this type of rotor. The gap between the movable tip and the fixed inboard portion of the blade can cause power losses, as discussed earlier. Fairings are used when possible to minimize these losses.

Passively-deployed pitchable tips are used for overspeed control in a number of normally fixed-pitch HAWTs (see Chapter 4). Centrifugal forces are used to deploy short tips at angles up to 90 deg when the rotor speed exceeds its operating limit. Data on the effectiveness of these so-called *air brakes* have been presented by Jensen *et al.* [1986]. *Tip plates*, also deployed by centrifugal force, have been employed for overspeed control on several medium-scale HAWTs, including the *ESI* and *Enertech* machines.

Aileron Control

Aileron control surfaces (sometimes referred to as *flaps*) are a potentially cost-effective means of rotor control. These devices have been investigated both theoretically and experimentally at the NASA Lewis Research Center for application to medium- and large-scale HAWTs [Miller and Sirocky 1985]. This work began in 1979, when aileron control was first evaluated as an alternative to blade-pitch control on DOE/NASA experimental HAWTs [Wentz *et al.* 1980]. The concept selected for study consisted of incorporating a movable control surface into the trailing edge of the rotor blade, in a manner analogous to the placement of ailerons and flaps in the trailing edge of an airplane wing. Control surfaces on an aircraft wing usually deflect toward the high-pressure (lower) surface to

increase lift during takeoff and landing. On a wind turbine blade, ailerons deflect toward the low-pressure (downwind) surface of the airfoil to reduce lift and produce a braking effect.

Figure 5-22 shows cross-sectional diagrams of two typical aileron configurations evaluated for HAWT rotor control. The hinge line is on the downwind side of the blade, so that the aileron can be deflected toward the low-pressure surface. The primary difference between the two configurations illustrated is the chord length of the high-pressure control surface, c_{hp}. The configuration without a high-pressure control surface, referred to as a *plain aileron*, was found to have the best aerodynamic braking characteristics of all of the configurations tested. If the aileron has both a low-pressure and a high-pressure control surface it has been referred to as a *balanced aileron.*

Ailerons change the lift and drag characteristics of the basic blade airfoil as a function of the *aileron deflection angle*, producing corresponding changes in rotor torque and thrust loads. The changes in torque can be controlled by regulating the deflection angle, which in turn enables the regulation of rotor speed and/or rotor power output. A considerable amount of information on the aerodynamic behavior of HAWT rotors with ailerons has been obtained from full-scale turbine tests and wind tunnel tests of airfoils with ailerons [*e.g.* Miller and Corrigan 1984, Savino *et al.* 1985, Ensworth 1985].

One question of considerable importance is the potentially detrimental effect of *aileron gaps* on the aerodynamic performance of a rotor blade when the ailerons are not deflected. Since ailerons are located in the most productive spanwise portion on the blade, the question arises as to performance penalties caused by leakage from high-pressure to low-pressure surfaces through gaps between the aileron and the and the main structure of the blade. Figure 5-23 [Savino *et al.* 1985] shows the measured effect of aileron gap on the lift coefficient of a 7.3-m segment of a medium-scale HAWT blade with an undeflected aileron 6.1 m long. Normal gaps were found to reduce the chordwise (in-plane) force coefficient by about 0.01 to 0.02 at angles of attack below stall and to have no measurable post-stall effect. Drag coefficients below stall were not affected by normal aileron gaps. Some power loss may result when an aileron is deployed and a rapid negative gust occurs.

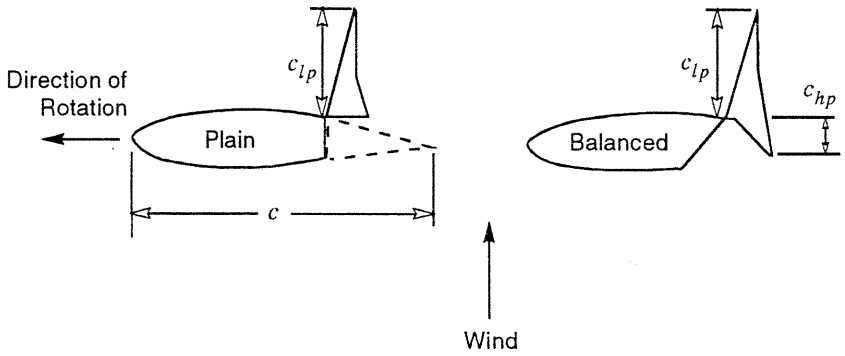

Figure 5-22. Schematic diagrams of typical aileron configurations for HAWT aerodynamic control. Ailerons are shown in the fully-deflected position for braking the rotor. [Miller and Sirocky 1985]

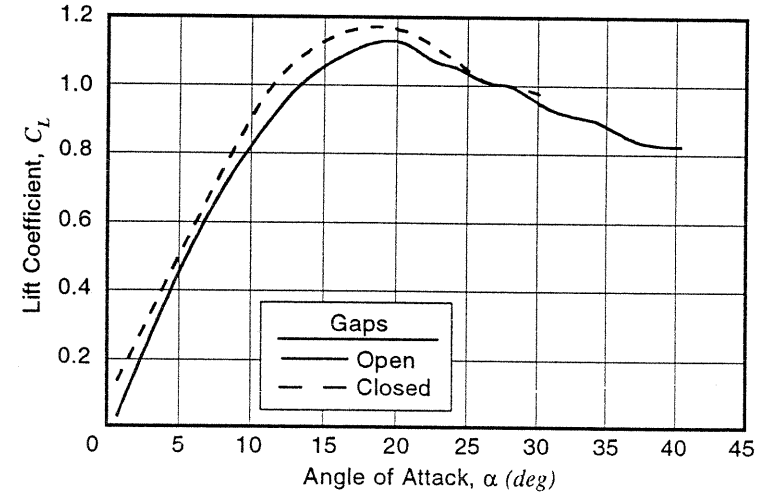

Figure 5-23. Effect of normal aileron gaps on the lift coefficient of a medium-scale HAWT blade when the aileron is not deflected. Wind tunnel test data. [Savino *et al.* 1985]

Transient Aerodynamics

Current state-of-the-art approaches use *steady-state aerodynamics* to determine aerodynamic forces, although the transient processes are well known. When *aerodynamic transients* occur during blade pitch changes, large-scale gusts or coherent turbulence (enveloping the whole rotor), or small-scale turbulence (smaller than the swept area) the question arises as to the *time history* of aerodynamic forces experienced by the rotor. If the initial force is F_1 and the final force is F_2, do transient forces ever fall outside the range between F_1 and F_2? The answer this question if definitely yes, because several processes are at work. First, pitch motion and/or gusts will induce a circulation (and, therefore, a force) which varies with the *pitch rate* and/or the *gust strength.* Second, during a transient, vorticity is shed parallel to the blade that interacts with the blade to dampen the forced response. Finally, there is vorticity trailing the blade, perpendicular to the span, which induces a flow that alters the angle of attack experienced by the blade.

Time Scales

Some insight into the relative importance of these force-producing processes can be inferred from their time scales. Let τ_g, τ_β, τ_{sv}, and τ_{tv} be the time scales associated with *gusts, pitch changes, shed vorticity,* and *trailing vorticity*, respectively. The gust time scale, τ_g, is a function of the site (through its *turbulence scale*) and the size of the rotor. The pitch-change time scale, τ_β, is specific to a particular control system. The change in lift coefficient induced by a pitch change at the rate $d\beta/dt$ is as follows:

$$\Delta C_{L,\beta} \approx \left(\frac{\pi}{2}\right)\left(\frac{c}{r}\right)\left(\frac{d\beta/dt}{\Omega}\right)$$

While the time scale τ_β is a significant parameter, the induced change in lift coefficient appears to be small, since $c << r$ and $d\beta/dt << \Omega$.

The third time scale, τ_{sv}, is associated with the shed vorticity that is convected downstream. This vorticity is initially parallel to the blade-pitch axis and yields a force response of the type $[1 - exp(- t/\tau_{sv})]$, as exhibited by the classical *Wagner gust function*. In broad terms, $\tau_{sv} \approx 5c/V_r$, so it can be seen that it varies with rotor size, tip-speed ratio, and position on the blade, since blades are usually tapered and

$$V_r \approx R\,\Omega$$

The fourth time scale, τ_{tv}, is associated with vorticity trailing downstream from the rotor. A simple actuator disk model of this process yields $\tau_{tv} = R/V$, where V is the wake velocity near the rotor.

Sample calculations of τ_{sv} and τ_{tv} will illustrate their relative durations. Assume a HAWT of radius R operating in a free-stream wind speed of 20 m/s, with a tip-speed ratio of 5.7, an axial induction factor of 0.2, and a chord-to-radius ratio of 0.045. Evaluating the shed vorticity time scale at 3/4 span, the results are as follows:

Shed vorticity: $\tau_{sv} = 0.0026\,R$
Trailing vorticity: $\tau_{tv} = 0.0625\,R$

where τ is in seconds and R is in meters. It can be seen that the time scale associated with shed vorticity is much shorter than that associated with trailing vorticity, and that both scales increase linearly with rotor size. From this example, it is evident that the first focus on aerodynamic transients should be on the trailing vorticity process. Further, the second focus should be to determine the nature of τ_g and τ_β.

The way in which an aerodynamic force approaches its steady-state value during a transient can be discussed qualitatively using an example in which a blade initially at pitch angle β_1 is suddenly brought to pitch angle $\beta_2 < \beta_1$. Since decreasing pitch increases angles of attack, the aerodynamic force then goes from one positive value to a higher positive value. The shed vorticity effect dies out in a time period of $2\tau_{sv}$ to $3\tau_{sv}$. This leaves the blade with the final pitch angle but the *initial* induced velocity, since τ_{tv} (which is also the time scale of induction changes) is much longer than τ_{sv}. Hence, the aerodynamic forces will first exceed the final forces and then decrease to them asymptotically as the added induced velocity develops from the wake vorticity. In every case of sudden pitch change, transient forces will go outside the range of the initial and final forces. Similar arguments can be used to examine gust responses.

Dynamic Stall

Transient aerodynamics has another facet called *dynamic stall*, which is related to changes in the lift curve near its peak and in the first stages of stall, resulting from oscillations in the angle of attack. These changes often produce a *hysteresis loop* in the lift coefficient which can, in turn, lead to cyclic pressure loadings that are not predictable from conventional lift and drag data obtained at steady angles of attack. Increased excitation of blade structural-dynamic modes becomes a possibility during dynamic stall. Analytical investigations of the potential scope of these cyclic loads have been conducted using the *Gormont* model [1973]. Dynamic stall effects have been measured and analyzed for HAWT rotors by Hansen [1992] and Hansen and Butterfield [1993], and these have also been analyzed by Berg [1983] for VAWT rotors.

Vortex Generators

Wind turbine blade designers, often faced with an undesirable tradeoff between thin airfoils with superior performance but inferior strength and moderately thick airfoils with superior strength but inferior performance, have recognized the benefit from some sort of *boundary-layer control* to increase the resistance of the boundary layer on a thicker airfoil to *adverse pressure gradients*. This would delay separation and stall, and perhaps allow a moderately-thick airfoil to reach a higher lift coefficient without a large drag penalty.

Re-energizing the boundary layer on a wind turbine blade can be achieved by mixing the boundary layer air with faster-moving air from the free stream. This mixing occurs naturally in a *turbulent boundary layer*, and one simple "fix" used to extend the performance of a number of airfoils is to add a *trip strip* (a small step or band of roughness perpendicular to the flow direction) to the low-pressure surface, to force the transition of a previously laminar boundary layer to a turbulent one. However, the rate of momentum transfer in a turbulent boundary layer is limited by the magnitude of the turbulence. If the turbulence could be increased, the mixing rate would also increase, and there would be the potential for performance improvements greater than those possible with trip strips.

Vortex generators provide a simple method of increasing this mixing rate. These devices were first developed at the *United Aircraft Corporation* and are credited largely to Taylor [1947] and Bruynes [1951]. In their simplest form, they consist of small vanes projecting normal to the low-pressure surface of the airfoil at an angle of attack to the incoming flow (Fig. 5-24). In this configuration they behave like half-wings and generate trailing vortices from their tips. These vanes can be parallel to one another or arranged with alternate positive and negative angles of incidence, producing *corotating* or *counterrotating* vortices, respectively. They have been used to suppress or delay separation in diffusers, pipe bends, and wings. It should be noted that by creating an energetic vortex, vortex generators necessarily incur a *drag penalty* when separation is not imminent.

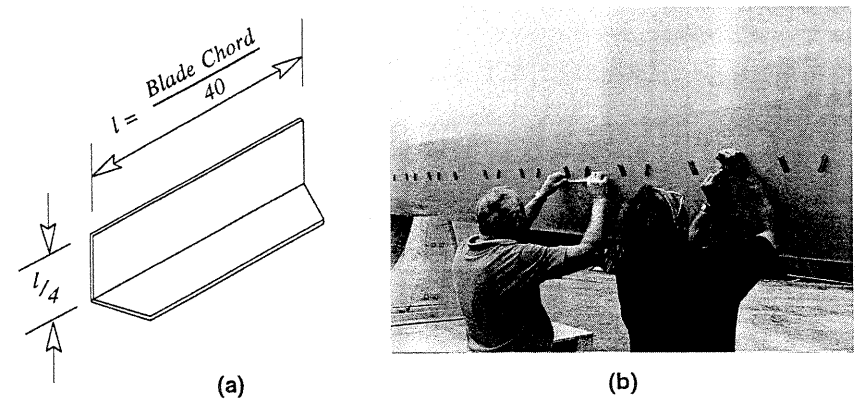

Figure 5-24. Vortex generators on the 3.2-MW Mod-5B HAWT. (a) Typical vane dimensions (b) Installing counter-rotating pairs of VGs on the low pressure side of the blade, with ± 20 deg angles of incidence at 10% of chord

The first application of vortex generators to wind turbine blades was performed by the Boeing Engineering and Construction Company on the 2.5-MW Mod-2 HAWT [Boeing 1982]. This installation and that on the later 3.2-MW Mod-5B HAWT were of the counterrotating type. Wind tunnel tests verified that vortex generators would delay stall and increase the maximum lift coefficient of the moderately-thick airfoils used in these rotors. In addition, vortex generators helped solve a control instability problem in the Mod-2 caused by intermittent stalling of the airfoil sections near the gap between the fixed and moveable sections of the rotor.

Shown in Figure 5-25 are power curves for the Mod-2 HAWT with and without vortex generators on the blades [Sullivan 1984]. Without vortex generators, control instability forced a non-optimum pitch setting during operations in below-rated winds, particularly at the "knee" of the power curve. This resulted in a substantial loss in power when wind speeds were between 11 and 15 m/s. Vortex generators over the fixed sections of the rotor (the inboard 70 percent of span) eliminated the control instability and permitted a more-optimum pitch setting, reducing the rated wind speed by almost 2.5 m/s, compared with previous operations. When vortex generators were also added to the tip sections, improvements in the lift coefficient further increased power in below-rated winds.

Similar tests were also made on the 25-kW Carter Model 25 HAWT [Gyatt 1986]. In this rotor the blades are highly twisted, so at low wind speeds the angles of attack along the inboard segments of the blade are well below stall. Thus, while vortex generators increased the maximum power of the Carter Model 25, power output at low wind speeds was reduced by the additional drag of the vortex generators.

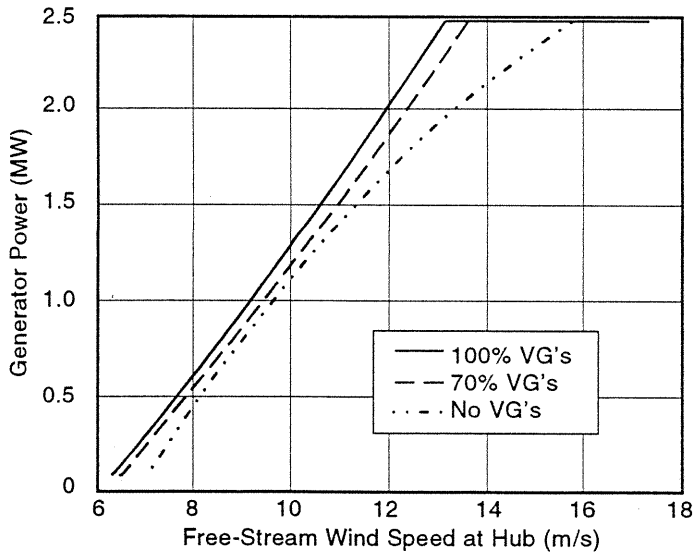

Figure 5-25. Test power curves for the 2.5-MW Mod-2 HAWT with and without vortex generators on the rotor airfoils. [Sullivan 1984]

Field Tests of HAWT Performance

One of the aerodynamicist's few windows for observing and understanding the physical phenomena of wind turbine aerodynamic behavior comes from performance data obtained during field testing of HAWTs. In particular, engineers at the NASA Lewis Research Center and their turbine development contractors have conducted numerous field tests on three generations of medium- and large-scale HAWTs, from the 100-kW 38-m diameter Mod-0 to the 3.2-MW 97.5-m diameter Mod-5B (see Chapter 3). Since these machines all have two-bladed rotors and each has operating characteristics that represent different aspects of rotor aerodynamics, performance data from three of these turbines will be presented here and compared with performance predictions made in accordance with modified strip theory. The specific examples are these:

-- The Mod-0 HAWT (38-m diameter; 100-kW rating) operating at *fixed pitch*. Under high wind conditions the flow over the rotor blades was well into the stall region.
-- The MOD-1 HAWT (61-m diameter; 2-MW rating), which operated in the *vortex ring/windmill brake* state under low wind conditions.
-- The MOD-2 HAWT (91.4-m diameter; 2.5-MW rating) using *partial-span pitch control* as well as *teetering*. This rotor is generally representative of those on second- and third-generation HAWTs.

As discussed in the introduction to this chapter, performance data taken during a field test are stored and plotted using the *method of bins* [Akins 1978], producing a graph of output power versus wind speed or a *power curve*. Comparisons with theory will be made on the basis of the *mean value* of the test data in each bin. The *standard deviation* will also be shown when available.

Mod-0 HAWT Performance

This rotor had tapered and twisted blades with airfoil sections from the NACA 23000 series. Airfoil thickness-to-chord ratios varied considerably, ranging from 0.12 at the tip to more than 0.40 at the blade root, with a rotor solidity of 2.9%. During this series of tests, the MOD-0 wind turbine was operated at fixed pitch, with a tip speed of 55 m/s [Viterna and Corrigan 1981]. Results from these tests are shown in Figure 5-26 and are typical of the performance of fixed-pitch HAWTs. Power increases with increasing wind speed, holds constant, and then decreases somewhat. This process is referred to as *stall regulation*. Strip theory predictions of power agree with the test results over the entire range of wind speeds, including post-stall operations for which an empirical model was developed by the investigators.

Mod-1 HAWT Performance

The Mod-1 rotor had tapered and twisted blades with a solidity of 4.2 percent, half again as much as the Mod-0 rotor. The higher solidity of the Mod-1 turbine resulted in the development of large axial inductions at low wind speeds, so wake expansion effects were considerable. The NACA 4400 series of airfoils was employed for the two rotor blades, with thickness-to-chord ratios varying from 0.09 at the tip to 0.33 at the root. Performance test data [Spera and Janetzke 1981] were measured at a rotor speed of 3.63 rad/s, which produced a relatively high tip speed of 111 m/s. Full-blade pitch was used to hold power constant at 2 MW in high winds, and pitch was held constant in below-rated winds.

Figure 5-27 shows measured and predicted power output for the Mod-1 HAWT as a function of free-stream wind speed. Strip theory power predictions are shown based on both *smooth* and *half-rough airfoil* lift and drag data. Half-rough data are obtained by averaging reference smooth and *rough* airfoil data [Abbot *et al.* 1945]. (Rough airfoil performance is unrealistically low for wind turbine blades.) Smooth airfoil data leads to

predictions which closely match measured power at levels greater than one-half of rated power, where wind turbines produce the majority of their energy output (see Table 5-1).

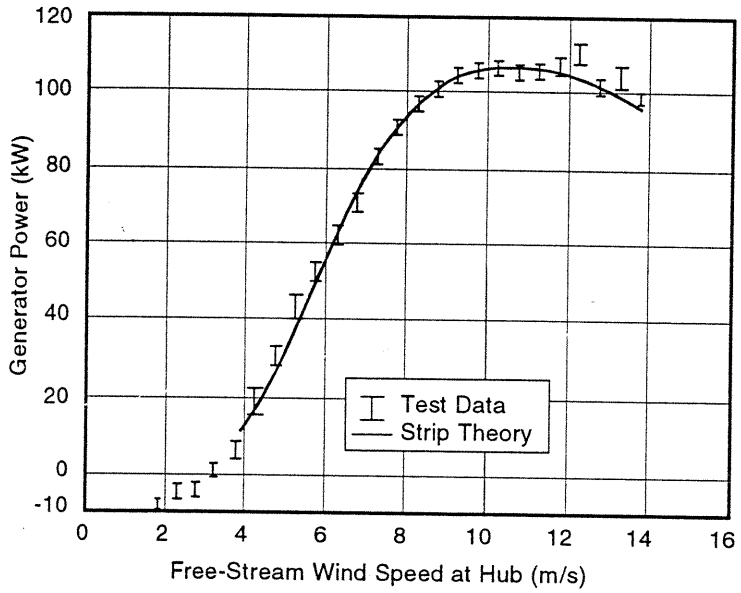

Figure 5-26. Power curve of the 38-m diameter Mod-0 HAWT with fixed blade pitch.

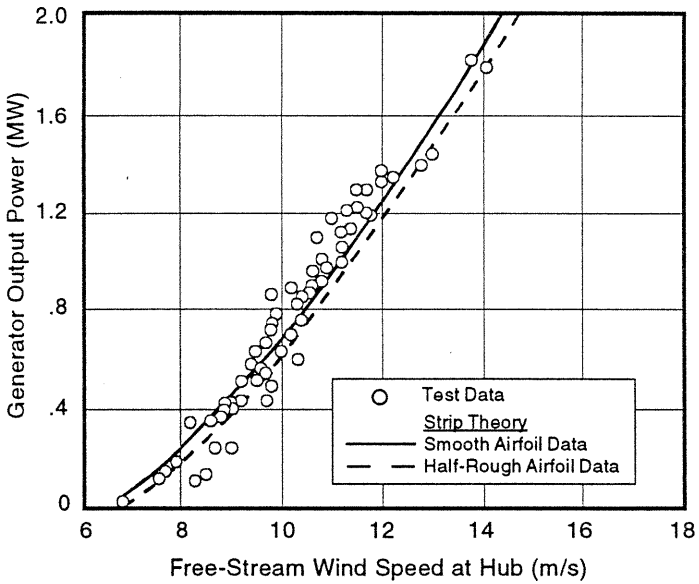

Figure 5-27. Power curve of the 61-m diameter Mod-1 HAWT.

Mod-2 HAWT Performance

The 2.5-MW Mod-2 turbine design had a two-bladed teetering rotor that used airfoils in the NACA 23000 series. It had a rotor solidity of 0.036 and tip speed of 84 m/s, which places these parameters midway between those of the Mod-0 and the Mod-1 rotors. The outboard 30% of each blade had variable pitch for starting, stopping, and controlling power output. In contrast to the wind turbines examined previously, the Mod-2 control system employed pitch change during operation in below-rated winds. The test data presented here are for the rotor without vortex generators, and in this configuration the pitch schedule below rated power was as follows (tips are fully-feathered at a pitch angle of - 90 deg): For power outputs between 0 and 1.0 MW, the tip pitch varied linearly with power, from - 5 deg to - 2 deg; from 1.0- to 2.5-MW the turbine was operated at a fixed blade pitch of - 2 deg.

Figure 5-28 is a plot of test data reported by Boeing [1982] compared with predicted power output obtained using modified strip theory [Wilson and Walker 1984]. A correction for the 0.3-m gaps between the fixed- and variable-pitch portions of the rotor (developed earlier in this chapter) is included in the predicted power. At the "knee" of the power curve, wind turbulence and control system actions generally cause the mean test power of HAWTs to fall below theoretical predictions, unless the effects of these two factors are specifically added to the performance model. Below the knee of the power curve, strip theory predicts the system power with acceptable accuracy.

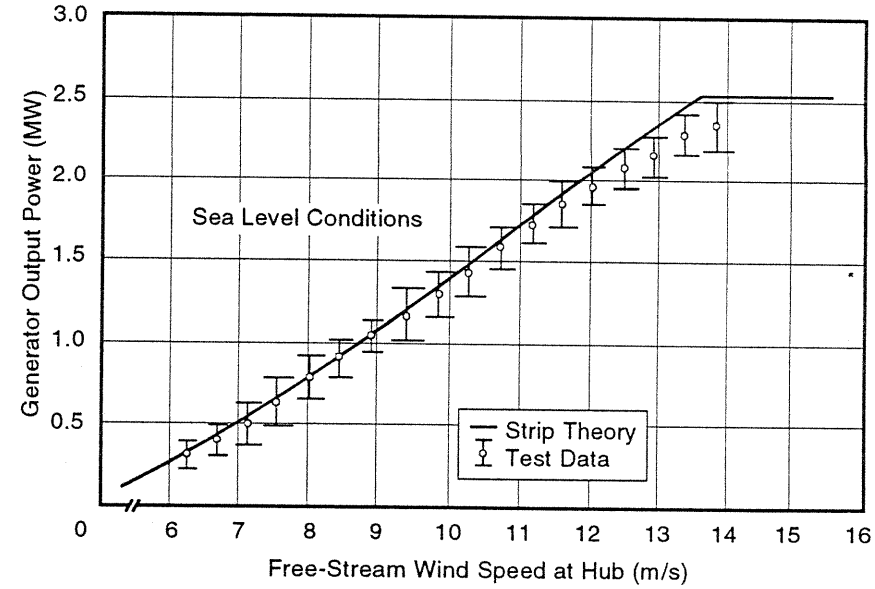

Figure 5-28. Power curve of the 91.4-m diameter Mod-2 HAWT. Test data from [Boeing 1982]; theory from [Wilson and Walker 1984]

Dimensionless Performance Parameters

Shown in Figure 5-29 is a dimensionless plot of power coefficient K_P versus advance ratio J, displaying performance test data for all three of the wind turbines in these examples. Although the three turbines vary in rated capacity from 100 kW to 2.5 MW, their dimensionless performance characteristics are seen to be remarkably similar. The Mod-1 HAWT, with its highly-twisted blades, high tip speed, low solidity, and NACA 44XX-series airfoils, is observed to have superior performance in below-rated winds.

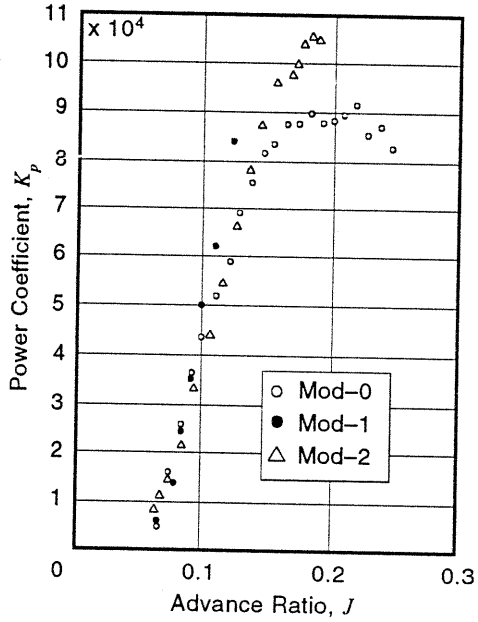

Figure 5-29. Dimensionless performance curves, permitting comparison of test data for the Mod-0, Mod-1, and Mod-2 HAWTs. [Wilson and Walker 1984]

HAWT Aerodynamic Loads

In general, the determination of the loads on a HAWT rotor involves the complex interaction of aerodynamic forces, structural deformations, and wind variability in both time and space. However, the aerodynamic moment obtained from a rigid-body analysis (the first integral in Equation (5-41a)) is a fair estimate of the *steady blade bending load.* The peak (maximum) value of this steady load occurs at rated power for a pitch-controlled rotor. Using the *Glauert optimum rotor* model, upper bounds can be established for steady bending loads, but these will greatly overestimate the actual aerodynamic loadings when the blade design departs appreciably from the optimum configuration. For the Glauert optimum rotor, the circulation is constant along the blade, approaching the following value at higher tip-speed ratios:

$$\Gamma \rightarrow \frac{8\pi}{9}\frac{U^2}{B\Omega} \tag{5-44}$$

The following axial and tangential air loadings are easily obtained from this circulation:

$$p_{a,x} = 0.5\,\rho\,U^2\,\frac{16\pi}{9B}\,r \tag{5-45a}$$

$$p_{a,y} = 0.5\,\rho\,U^3\,\frac{32\pi}{27B\Omega}\left(1 - \frac{3r\Omega}{2U}\,\frac{C_D}{C_L}\right) \tag{5-45b}$$

where x, y = subscripts designating axial and tangential air loadings, respectively

Drag has less effect on the axial loading, and Equation (5-45a) contains only the lift contribution. The aerodynamic flatwise bending moment on a Glauert optimum blade is

$$M_y = \int_s^R p_{a,x}\,r\,dr = 0.5\rho\,U^2\,\frac{8\pi R^3}{27B}\left[2 - 3\,\frac{s}{R} + \left(\frac{s}{R}\right)^3\right] \tag{5-46}$$

where s = blade station, measured from the rotor axis (m)

Again, Equations (5-45) are applicable only at higher tip-speed ratios and can be expected to overestimate air loadings on blades significantly different in shape from the Glauert optimum configuration. Figure 5-30 illustrates the relative sizes of steady flatwise bending moments measured on a Mod-2 HAWT blade [Boeing 1982], an upper bound calculated in accordance with Equation (5-46) for tip-speed ratios greater than 10, and steady bending loads predicted using strip theory. This blade design is far from the Glauert performance-optimized configuration, and Equation (5-46) significantly overestimates the bending load.

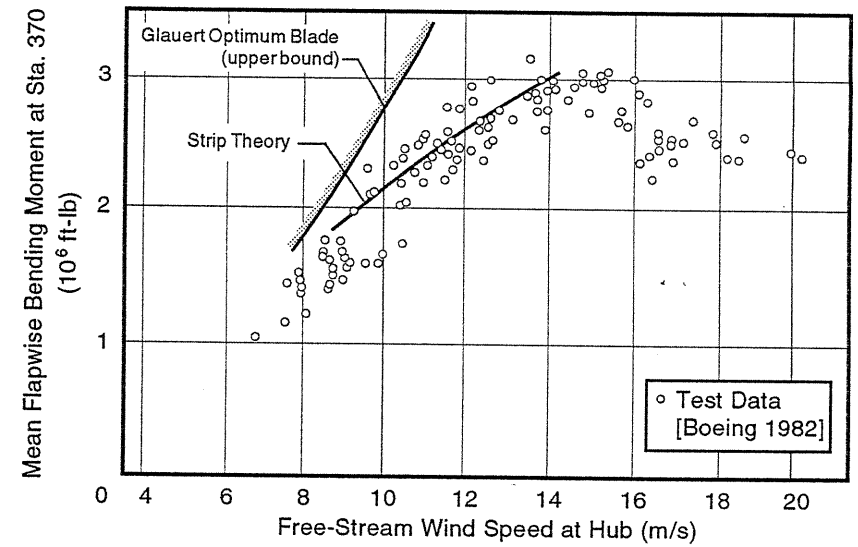

Figure 5-30. Measured and calculated steady flatwise bending moments *vs.* free-stream wind speed at 20 percent span in a Mod-2 HAWT blade.

Aerodynamic Analysis of Vertical-Axis Wind Turbines

Modern VAWTs are almost exclusively of the curved-blade design patented by G. Darrieus [1931]. However, this type of wind turbine did not see extensive development until the 1970s when it was re-invented at the National Research Council of Canada [South and Rangi 1972]. Engineers there and at the NASA Langley Research Center [Muraca *et al.* 1975] and the Sandia National Laboratories [Blackwell and Reis 1974] undertook the analysis, design, construction, and testing of Darrieus VAWTs. In the course of subsequent development projects, many aerodynamic models for the Darrieus rotor have been proposed, and these may be classified into the following three groups:

-- *Streamtube models* [Templin 1974, Wilson and Lissaman 1974, Muraca *et al.* 1975, Shankar 1975, Strickland 1975, Wilson and Walker 1981, Paraschiviou 1981].
-- *Fixed-wake vortex models* [Holme 1976, Wilson 1978, McKie *et al.* 1978]
-- *Free-vortex models* [Fannuci and Walters 1976, Strickland *et al.* 1980]

These models vary considerably in their treatment of the flow, and no single approach is available that covers all significant effects over the entire operating range of a VAWT, such as *dynamic stall, variable induced flow,* and *wake crossing* by the downwind blade.

In streamtube models the induced axial velocity is calculated at the rotor by equating the *time-averaged force* on the blades to the *mean momentum flux* through a streamtube of fixed location and dimensions. Single, tandem, and multiple streamtubes have been used, as illustrated in Figure 5-31 [Touryan *et al.* 1987]. Streamtube models, with some exceptions [Wilson and Walker 1981, Parashiviou 1981], predict fore-and-aft symmetry of flow quantities. Aerodynamic forces are calculated from local angles of attack and local relative velocities, using static airfoil lift and drag coefficients which may include post-stall behavior. Streamtube approaches have met with modest success in predicting the overall torque and thrust loads on Darrieus rotors. Additionally, the computer time needed for streamtube computations is much less than that for any other approach.

Fixed-wake vortex models use a *vortex sheet wake* that is locally independent of time. Forces are determined from circulation using the *Kutta-Joukowski law*. The fixed-wake vortex analysis has a distinct advantage over streamtube methods below stall, in that it has

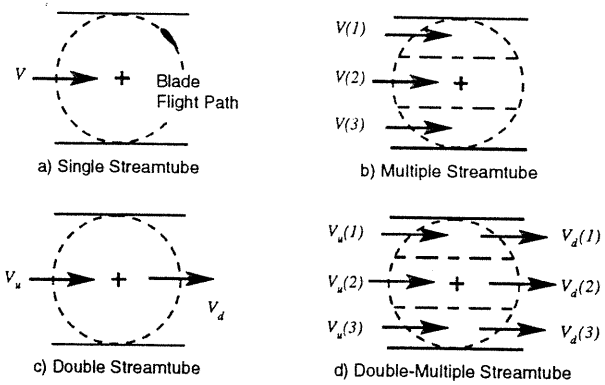

Figure 5-31. Plan view sketches of various streamtube models used for aerodynamic analysis of VAWT rotors. (a) Single streamtube (b) Multiple streamtube (c) Double streamtube (d) Double-multiple streamtube [Touryan *et al.* 1987]

the ability to identify the *crosswind-induced flow*. Its computational time requirements exceed those of streamtube models, but are at least of the same order.

The most complete and accurate method of analysis that has been developed for predicting the aerodynamic behavior of a Darrieus rotor is the *free-vortex* approach. The rotor wake is modeled by discrete, force-free vortices, each of which is convected downstream at a velocity determined by induced velocities from the rest of the system. Unfortunately, the free-vortex approach is also the most complex and has several other disadvantages:

-- Power and load values are approached asymptotically from above as the wake length is increased towards infinity. As a result, the practical requirement of a finite-length wake results in predictions that are too high.
-- Since the wake moves very slowly at high tip-speed ratios, it is always easier to analyze rotors operating at low tip-speed ratios.
-- Overall, free-vortex analysis is quite expensive to perform.

Limiting VAWT Performance

We will first consider the performance limit of a *giromill rotor*, a design also proposed by Darrieus. A giromill consists of straight, vertical, rectangular blades rotating about a vertical axis. The blades are *articulated* in pitch to maximize the extraction of energy from the wind. A necessary condition for maximum energy extraction is that the far-wake velocity be uniform. By virtue of its articulated blades, a giromill will have higher performance than a fixed-pitch Darrieus rotor. Therefore, a performance limit for a giromill is also an upper bound for the performance of a Darrieus VAWT.

Figure 5-32 illustrates the development of an actuator disk model of a giromill. In this schematic plan view, B blades ($B >> 1$) of chord c are situated around the circumference of a rotor of radius R. As a blade moves around the circle, its pitch angle is modulated to keep the circulation constant. At the azimuthal positions of $\psi = 90$ deg and $\psi = 270$ deg, each blade is "flipped" (*i.e.*, its pitch angle changes sign) to produce a circulation of equal magnitude but opposite sign. This change of sign in circulation is necessary to maintain a positive force in the tangential direction. The wake consists of concentrated vortices moving downwind in vortex-street fashion. As $B \to \infty$ and $c \to 0$ while the product Bc is held constant, the discontinuous vortex streets become continuous *vortex sheets*, and the entire flow field becomes steady.

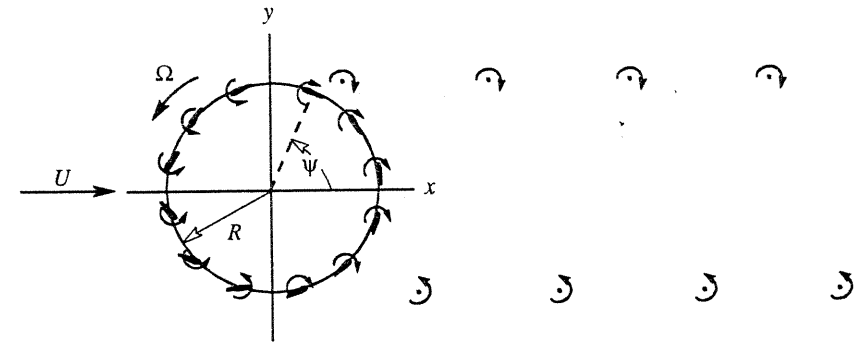

Figure 5-32. Schematic plan view of a vortex-sheet model of a giromill flow field.

The velocity field of the rotor consists of three parts that can be superimposed to obtain the flow field: the free-stream velocity, U; the wake-vortex sheet velocity, v_w; and the bound-vortex sheet velocity, v_b. Analysis of this vortex sheet model of the flow field about a giromill shows that the power and thrust coefficients of a VAWT have the same limits as those of a HAWT, given by Equations (5-15a) and (5-30) [Wilson 1978]. In addition, this analysis also yields a *shear (crosswind) force coefficient,* C_S, as follows:

$$C_S = \frac{S}{0.5\,\rho\,U^2 R H} = -\frac{\pi}{\lambda} a^2 (1 - a) \qquad (5\text{-}47)$$

where H = height of the giromill rotor (m)

Fixed-Wake Streamtube Analysis

In order to analyze the aerodynamic behavior of a VAWT in accordance with the streamtube approach, first consider an airfoil traversing the idealized path shown in Figure 5-33(a). This airfoil is assumed to be symmetrical in cross-section and have negligible drag. Between points A and B the airfoil moves parallel to the free stream and generates

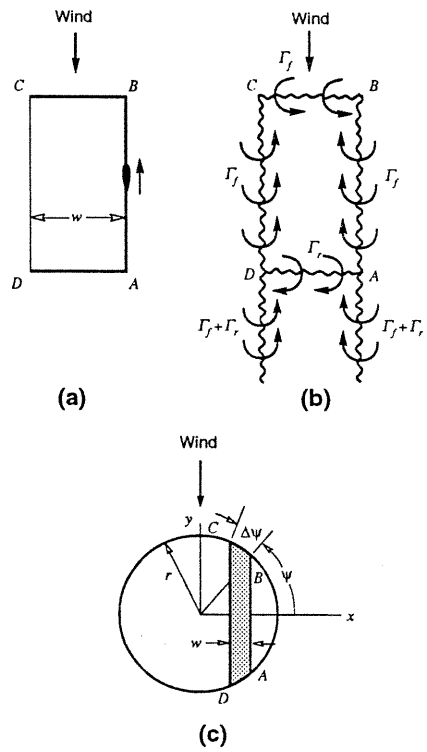

Figure 5-33. Development of a VAWT streamtube model. (a) Plan view of an idealized blade path (b) Resulting circulation in the wake (c) VAWT streamtube

no force. At point B, the airfoil suddenly changes direction and sheds vorticity. It then moves across the wind for a distance w, generating both lift and circulation. Again at point C, the direction of motion is changed and vorticity is shed, opposite in sign to that shed at B. From point C to point D no force is generated. Finally, on the path from D to A, the airfoil once again generates lift and circulation, the latter opposite in direction to the circulation along path BC. The wake system that is generated is illustrated in Figure 5-33(b), in which the local circulation direction is indicated by the arrows and where

Γ_f, Γ_r = magnitudes of front and rear circulation, respectively (m^2/s)

Axial Induction of a VAWT Rotor

We may take certain liberties with the idealized path illustrated in Figure 5-32(a) without changing the wake pattern. In Figure 5-33(c), the width w has been reduced relative to the distance AB, and the paths BC and DA have been made to conform with the path of a Darrieus rotor blade. Thus, we have a streamtube of a Darrieus rotor. Considering the flow in other streamtubes to be similar, we arrive at several significant observations:

- Since flow along BC is influenced only by flow inside the vortex street shed by BC, forces on an airfoil traversing BC are not influenced by adjacent streamtubes.
- As the streamtube gets smaller in width, the wake from BC appears as a semi-infinite vortex street. The resulting induced velocity at the front is due only to the semi-infinite wake of the front caused by Γ_f.
- An airfoil on the rear path DA "sees" an infinite wake caused by the front circulation, Γ_f, and a semi-infinite wake caused by the rear circulation, Γ_r. Thus, the rear induced velocity depends on both the front and rear circulations.

These observations lead to the following equations for the induced velocities:

$$a = a_r - a_f \qquad (5\text{-}48a)$$

$$\frac{a_r}{a_f} = 2 - \frac{\Gamma_r}{\Gamma_f} \qquad (5\text{-}48b)$$

where a_f, a_r = front and rear axial induction factors, respectively

In order to determine the three local induced velocities (a, a_f, and a_r), a third equation is required. Let us use the momentum theorem and equate the windwise momentum change to the mean downwind blade force, which results in

$$a(1 - a) = \frac{B\Omega}{4\pi U^2}\left[\Gamma_f - \Gamma_r\right] \qquad (5\text{-}48c)$$

The circulations in Equation (5-48b) do not include bound circulation. For a symmetrical airfoil with its chord tangent to the path of rotation, the only bound circulation is that from pitching. Using linear aerodynamics with a lift curve slope of C_L' and noting that $(sin\psi)_{rear}$ equals $-(sin\psi)_{front}$, Equations (5-48) may be reduced to the following:

$$a^3 - 2a^2(1+G) + a(1+4G+G^2) - 2G = 0 \qquad (5\text{-}49a)$$

$$G = \frac{\lambda B c C_L'}{8\pi R}\cos\theta \sin\psi \qquad (5\text{-}49b)$$

$$a_f = \frac{1-\sqrt{1-2a}}{2} \qquad a_r = a_f + a \qquad (5\text{-}49c)$$

where θ = inclination of blade norml from the horizontal (rad)

Explicit solutions of the cubic equation may be obtained. For nonlinear aerodynamics, the local circulation (exclusive of bound circulation) is $0.5C_L c V_r$, and iteration is required.

Torque of a VAWT Rotor

Consider an element of a Darrieus rotor blade, as shown in Figure 5-34, acted upon by the local effective wind. The airfoil is assumed to be symmetrical, with its chord line tangent to the circumferential path. As was true for the coned HAWT rotor, the spanwise component of the relative wind does not contribute to lift or drag, so

$$V_e = \sqrt{V_\psi^2 + V_n^2} \qquad (5\text{-}51a)$$

$$\alpha = \arcsin(V_n/V_e) \qquad (5\text{-}51b)$$

where V_e = effective wind speed (m/s)
V_ψ = circumferential (chordwise) wind speed (m/s)
V_n = wind speed normal to the element (m/s)

Referring to Figure 5-34, the circumferential and normal wind speeds can be calculated from the free-stream wind speed, the rotor speed, and the axial induction factors as follows:

$$\text{For } 0 \le \psi \le \pi: \quad V_\psi = r\Omega + U(1-a_f)\cos\psi \qquad V_n = -U(1-a_f)\sin\psi\cos\theta \qquad (5\text{-}51c)$$

$$\text{For } -\pi \le \psi \le 0: \quad V_\psi = r\Omega + U(1-a_r)\cos\psi \qquad V_n = -U(1-a_r)\sin\psi\cos\theta \qquad (5\text{-}51d)$$

As shown in Figure 5-35, the lift and drag forces on an element of blade of length ds produce a differential torque dQ about the axis of rotation that is given by

$$dQ = dQ_{KJ} + dQ_D \qquad (5\text{-}52a)$$

$$dQ_{KJ} = 0.5\rho V_e^2 c C_L \frac{\sin\alpha}{\cos\theta} r\,dz \qquad (5\text{-}52b)$$

$$dQ_D = -0.5\rho V_e^2 c C_D \frac{\cos\alpha}{\cos\theta} r\,dz \qquad (5\text{-}52c)$$

where dQ_{KJ} = *Kutta-Joukowski* (lift) torque contribution (N-m)
dQ_D = drag torque contribution (N-m)
dz = incremental height (m)

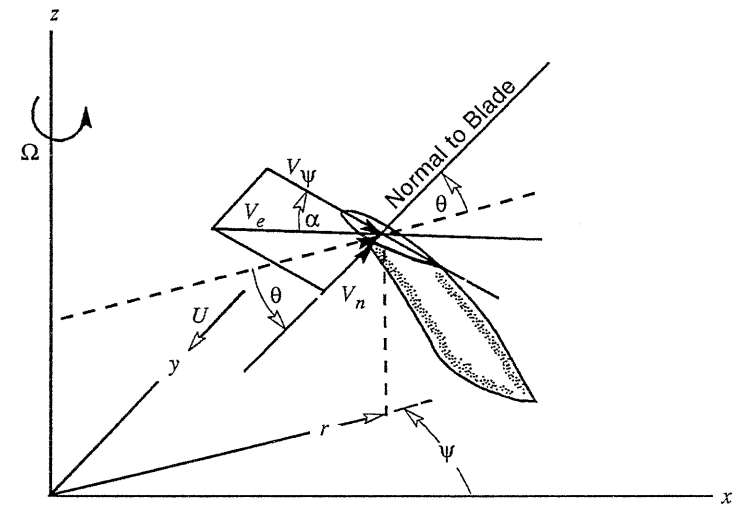

Figure 5-34. Geometry of a Darrieus blade element and the effective wind velocity.

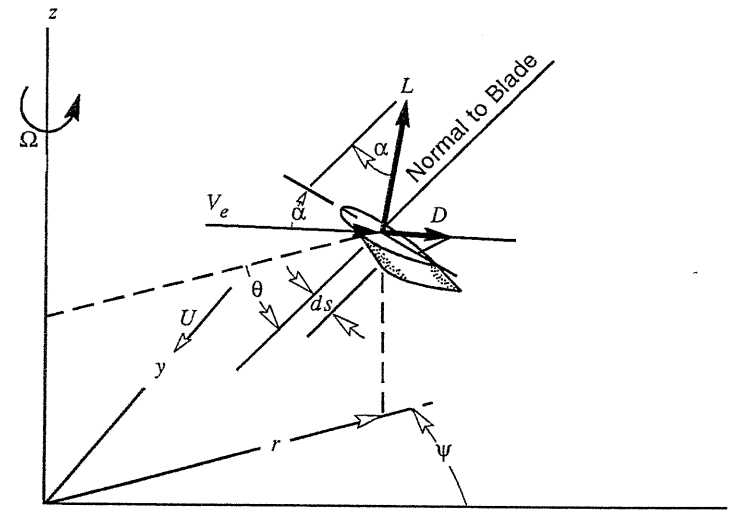

Figure 5-35. Wind velocity and force diagram for a Darrieus airfoil segment.

The torque of a VAWT rotor varies with blade azimuthal position (the so-called *torque ripple*), so rotor power is defined as the average power over one revolution, as follows:

$$P = \frac{B\,\Omega}{2\,\pi} \int_{0}^{2\pi} \int_{-H/2}^{H/2} \left(dQ_{KJ} + dQ_{D} \right) d\psi \qquad (5\text{-}53)$$

where H = height of the area swept by the airfoils (m)

Airfoil Data for VAWT Blades

When using streamtube analysis, the determination of aerodynamic forces is accomplished using available static lift and drag data. Despite the amount of airfoil section properties compiled by the NACA and more recent work by NASA, extensive gaps remain in our knowledge of wind turbine airfoils. Aircraft airfoils are designed to operate below stall, and so the data base is concentrated in the below-stall region. A VAWT blade, however, operates at angles of attack considerably beyond stall, particularly when it is producing peak power. Another variance between VAWT and aircraft airfoils is that a VAWT blade follows a circular path with significant cyclic variations in relative velocity and angle of attack.

The applicability of steady-state airfoil data to the unsteady operating conditions of a VAWT may be questioned. Below stall, however, the use of static lift data appears to be valid. Shown in Figure 5-36 is the variation in lift coefficient during a typical rotor revolution, calculated for a section on a VAWT blade. The VAWT lift curve remains approximately parallel to the theoretical static lift curve for chord-to-radius ratios of 0.10. Typical ratios for current VAWTs are less than 0.08.

A third factor affecting airfoil data is the pitch rate of a VAWT blade, which is equal to the rotor speed Ω. In Figure 5-36, the offset angle between the static and dynamic lift curves, α_p, is caused by pitching circulation. A first-order analysis of the effect of pitching on drag coefficient of a pitching *NACA 0015* airfoil below stall indicates that the offset angle for drag is 40% to 50% less than that for lift [Wilson and Neff 1985].

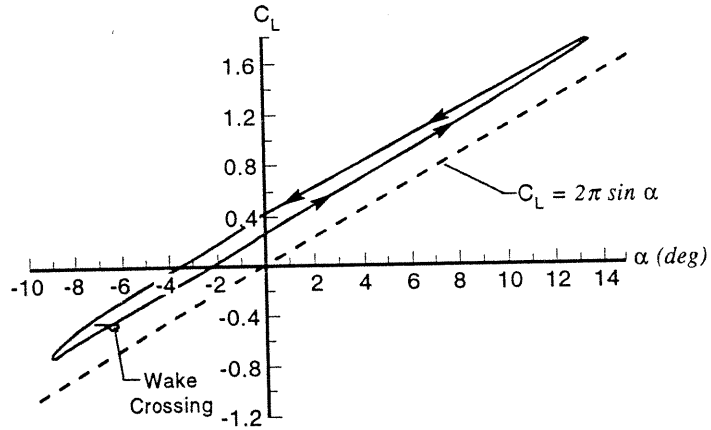

Figure 5-36. Calculated lift coefficient *vs.* angle of attack at a VAWT blade section during one rotor revolution. Tip-speed ratio is 3.5 and the chord-to-radius ratio is 0.2.

Comparison of Theoretical VAWT Performance with Test Results

Theoretical predictions of the performance of the *Sandia/DOE 17-m* VAWT (similar to that in Fig. 3-24) will now be compared with measured performance data [Worstell 1980]. The principal parameters of the Darrieus rotor on this machine are as follows:

Airfoil = NACA 0015; lift and drag data from [Sheldal and Klimas 1981]
R = 8.28 m (at z = 0) c = 0.61 m
H = 17.0 m A = 183 m^2
B = 2 Ω = 4.0 to 5.3 rad/s
N_R = 1.5 to 2.0 × 10^6 at the rotor equator

$$r = 2.790 + \sqrt{30.100 - z^2} \qquad 0 \le |z| \le 4.548 \ m$$

$$r = 12.60 - 1.4826\,|z| \qquad 4.548 \le |z| \le 8.090 \ m$$

Test power coefficients are plotted versus tip-speed ratio in Figure 5-37, together with vortex-model predictions [Strickland *et al.* 1979]. It can be seen that this type of aerodynamic model is quite accurate. However, since an aerodynamic analysis based on vortex theory is the most complex and time-consuming of the methods for predicting VAWT performance, it is generally reserved for validating simpler models.

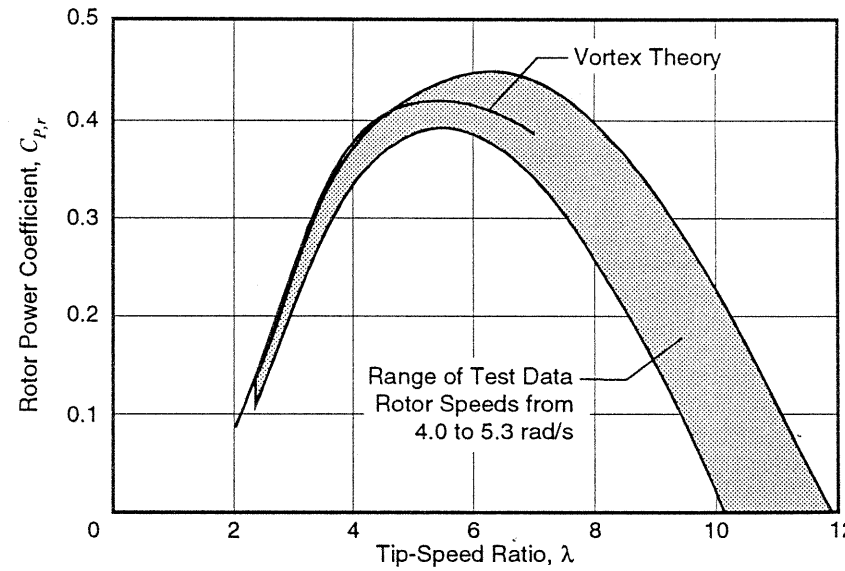

Figure 5-37. Comparison of experimental and theoretical power coefficients for the Sandia/DOE 17-m VAWT. Test data from [Worstell 1980]; theory from [Strickland *et al.* 1979]

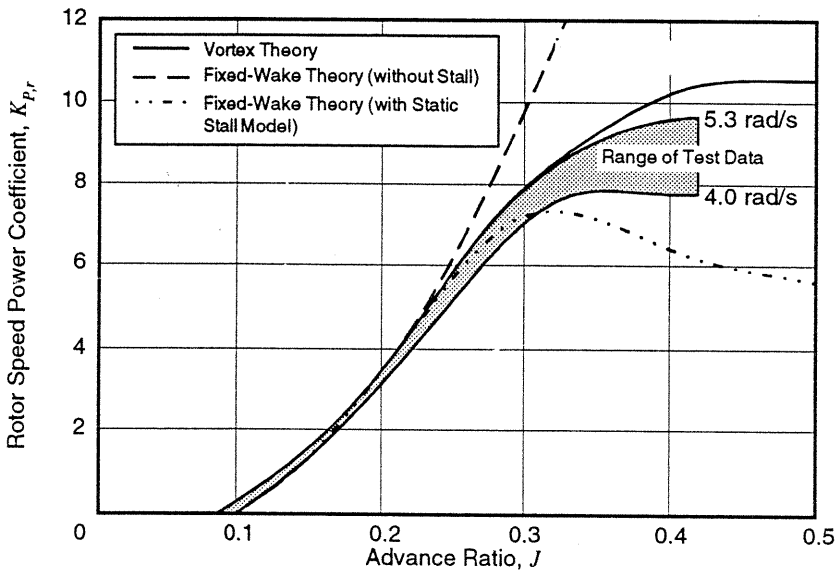

Figure 5-38. Experimental and theoretical dimensionless power curves for the Sandia/DOE 17-m VAWT. Test data and vortex theory are the same as in Figure 5-37. Fixed-wake theory from [Wilson and Walker 1981]

The test data and vortex theory predictions in Figure 5-37 are plotted in a dimensionless power-curve form in Figure 5-38, as rotor-speed power coefficient, K_P, *vs.* advance ratio, J. We note that the region of maximum power coefficient ($J \approx 0.18$ or $\lambda \approx 5.5$) occurs at low power levels, indicating that $C_{P,max}$ is not a critical parameter in determining the annual energy output of this VAWT or in evaluating various aerodynamic theories. Of more importance is performance at higher advance ratios, or (equivalently) tip-speed ratios less than that for $C_{P,max}$. It can be seen in Figure 5-38 that the power curves flatten at higher advance ratios, an effect attributed to increasing amounts of stall. Power levels trend upward with increasing rotor speed, reflecting the benefits of higher Reynolds Number and lower angles of attack.

Two additional theoretical predictions are shown in Figure 3-38. These are based on *fixed-wake theory, with and without static stall* in the airfoil properties [Wilson and Walker 1981]. At high advance ratios (*i.e.* high wind speeds), fixed-wake theory without stall overpredicts the measured power by large amounts. Note, however, that measured peak power levels trend toward the theoretical unstalled performance with increasing rotor speed. When static stall properties are added to the fixed-wake theory, the predicted power curve flattens at higher advance ratios and then drops below the test data. This latter behavior emphasizes the role of stall in reducing VAWT power at high wind speeds, and at the same time indicates that the transient stall experienced by the rotating blade is not as fully-developed as static stall.

A final comparison between experimental and theoretical VAWT performance is shown in Figure 5-39. Here, the 17-m test data are compared with predictions made with three streamtube theories: *multiple streamtube with static stall* [Strickland 1975], *double-multiple streamtube with static stall* [Paraschivoiu 1981], and *double-multiple streamtube with dynamic stall* [Berg 1983]. When static stall data are used, the streamtube and fixed-wake theories give much the same predictions of power, and these are in good agreement with test data at the most energy-productive advance ratios of a VAWT. With the addition of a dynamic stall model, correlation between test data and streamtube theory at high advance ratios becomes equivalent to that of the more-accurate vortex theory.

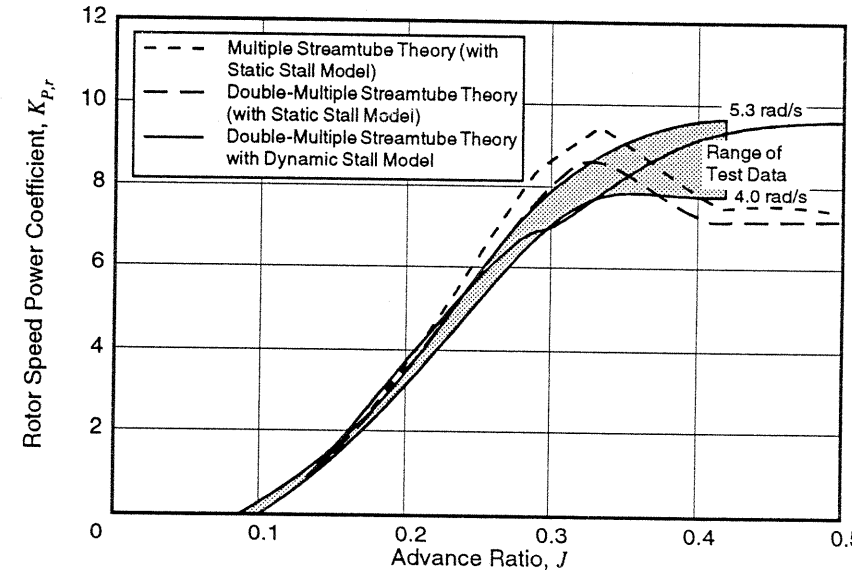

Figure 5-39. Experimental dimensionless power curves for the Sandia/DOE 17-m VAWT compared with streamtube theories. Test data are the same as in Figure 5-37. Theoretical predictions from [Strickland 1975, Paraschivoiu 1981, Berg 1983].

Dynamic-Stall Factors

Relatively early in the development of VAWTs, differences between performance test behavior and theory were attributed to dynamic stall [Strickland *et al.* 1980], which has a measurable effect on HAWTs but appears to be even more important to VAWT aerodynamics. Simply stated, dynamic stall on a blade can produce lift and pitching-moment values that are much larger than static values. These additional forces are brought on by a strong vortex that forms at the leading edge and is quickly convected over the blade and into the wake. Its formation and movement strongly depend on the following factors:

-- type of airfoil, leading edge radius, and thickness distribution;
-- initial angle of attack;
-- rate of increase of angle of attack;
-- excursion of angle of attack past the static stall angle;

The effect of this vortex on airfoil properties begins with a rapid increase in forces and ends with full flow separation and a large drop in lift. It is clear that the dynamic stall process depends both on the amplitude and the history of the angles of attack on the airfoil. There is also a *hysteresis effect*, involving a delay in re-attachment of the flow and recovery of blade forces to their static levels after the event. Stall time delays related to rapid increases in angle of attack have been used to reproduce analytically the flattening of VAWT power curves at high advance ratios [Masse' 1984].

Future Developments of VAWT Aerodynamic Theory

Continued comparison of theoretical and experimental VAWT performance has focused current research on the following:

-- improving the accuracy of predicting peak power output;
-- understanding dynamic stall at high wind conditions;
-- including stochastic wind models in order to predict fatigue loads on blades;
-- correcting the tendency to over-predict power output for operations between maximum rotor power coefficient and the onset of dynamic stall;
-- introducing interactions between adjacent flow regions;
-- eliminating assumptions that are known to be mathematically incorrect.

Local circulation methods [Azuma *et al.* 1983, Masse 1984] are candidates for improved models of the performance of VAWTs.

Aerodynamic Behavior of VAWTs in Operation

More than 600 VAWTs have been placed in commercial service, mostly in California, with generator capacities that range from 120 to 300 kW. All are two-bladed machines. Despite their lack of wind direction sensitivity, yaw control equipment, aerodynamic control surfaces, and teetered hubs, VAWTs still have many operational characteristics, several of which are unique. Starting and stopping, the role of transient aerodynamics, the use of vortex generators, and the effects of rotor solidity are subjects that VAWTs have in common with HAWTs, while the subjects of rotor blade shape and torque ripple are unique to the vertical-axis wind turbine.

Rotor Blade Shape

The blade shape of a Darrieus blade is patterned after the *troposkien* ("spinning rope"), a configuration in which every section of an ideal blade is locally in tension under action of the centrifugal acceleration (including a small correction for gravity loads), without bending stresses. Practical Darrieus blade shapes are composed of mixtures of circular arcs and straight sections that approximate the ideal shape, in order to reduce bending stresses and yet have a shape that can be easily manufactured. The *Sandia/DOE 17-m* research

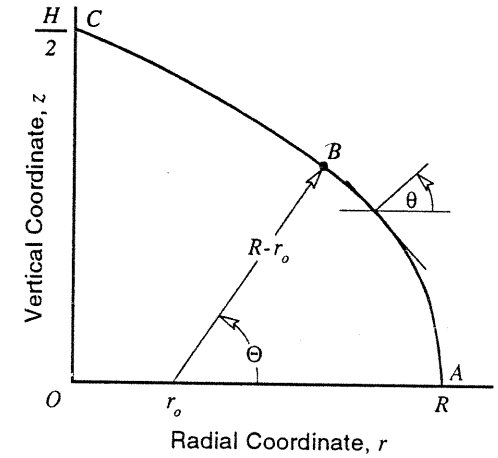

Figure 5-40. General configuration of a Darrieus VAWT rotor blade.

VAWT (as well as several commercial VAWTs that are derivatives of it) uses the blade configuration shown in Figure 5-40. It consists of a circular arc, *AB*, and a straight section, *BC*, instead of the continuously changing curvature of a true troposkien. The ratio of height to diameter, *H/2R*, is very close to unity in this rotor. U.S. commercial VAWTs have employed *aspect ratios* between 1.2 and 1.3, and the Canadian *Eolé* VAWT (Fig. 3-36) has a ratio of 1.5.

On the circular arc or *equatorial section* of the blade, local angles of attack are found to decrease as the radius *r* decreases. By contrast, angles of attack on the straight blade section increase from the junction with the arc toward the axis of rotation. Some of the operational characteristics of a VAWT rotor may be inferred by an examination of these variations in the local angle of attack.

First, consider the performance of a two-bladed Darrieus rotor in high winds (lower tip-speed ratios), during which power output is produced almost exclusively by the circular arc sections of the rotor. Since angle of attack decreases along the circular arc, and since a decrease in angle of attack reduces the amount of stall caused by high winds, the power output of the rotor will increase as the central angle Θ increases (holding blade chord constant). Increasing Θ in turn decreases the rotor aspect ratio. Thus, in broad terms one can say that decreasing the height-to-diameter ratio of a VAWT rotor will increase $K_{P,max}$. Carried to the limit, a VAWT with a circular rotor will have a higher $K_{P,max}$ than one with straight blades of the same length. However, a high value of $K_{P,max}$ is not particularly desirable, since it may force the power train to be too large to be cost-effective.

Next, consider the effect of rotor shape on VAWT performance in low winds (higher tip-speed ratios), when power is obtained from the straight sections of the blades. In low winds equatorial sections have very low angles of attack, to the point where power produced by lift is insufficient to overcome power lost by drag. As the angle Θ is increased, the straight segments of the rotor become longer (with a corresponding increase in aspect ratio) and the low-wind power output of the rotor increases. When the chord varies over different sections of the blade, the previous observations will hold as long as the blade chord remains fixed on each section.

Torque Ripple

Each section of a VAWT blade sees a wide variation in angle of attack during each rotor revolution. As a result, the torque produced by a blade, even in steady winds, is characterized by a cyclic time history termed *torque ripple*. Figure 5-41 shows typical variations in *torque coefficient* with blade azimuthal position, for a 17-m Darrieus operating at several tip-speed ratios. The torque coefficient is defined by

$$C_{Q,b} = \frac{Q_b}{0.5\,\rho\,U^2\,A\,R} \qquad (5\text{-}53)$$

where $C_{Q,b}$ = blade torque coefficient
Q_b = time-varying torque produced by one blade (N-m)

Over the front portion of the path, for about 40 percent of the revolution (ψ from about 30 to 160 deg), a blade produces positive torque. However, torque production on the remainder of the circuit is low or negative, mostly because of the lower angles of attack experienced on the rear path. At a tip-speed ratio of 11, the average torque is negative in this example. The torque ripple is smoothed significantly when the individual torques of two or more blades are added together, because of their phase differences.

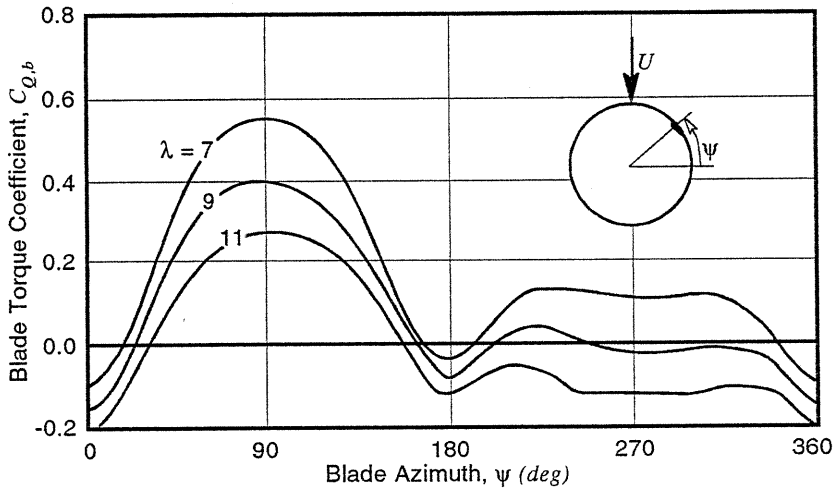

Figure 5-41. Typical variations in torque coefficient with blade azimuth or "torque ripple" produced by a single VAWT blade.

Rotor Solidity Effects

The solidity of a VAWT rotor can be changed by changing the number of blades or the blade chord dimensions. Current VAWTs are two-bladed machines, the two-bladed configuration being lighter and having fewer joints than a three-bladed rotor. Little has been done to determine the effect of blade number while holding other parameters constant. The most significant difference between two- and three-bladed rotors is that the rotor torque ripple, which has a distinctive twice-per-revolution oscillation for a two-bladed VAWT, is

almost eliminated in a three-bladed rotor. With little else examined for the aerodynamics of three-bladed rotors, the subject of the effects of solidity on rotor aerodynamics is focused here on changes in blade chord.

For a VAWT, solidity is expressed in two different ways. The first is the traditional way, as the ratio of the blade planform area to the rotor swept area. Such a determination requires detailed knowledge of blade chord *vs.* blade length and the swept area of the rotor, quantities which are tiresome to determine. A second expression for solidity, not equal to the first, is the term Bc_{max}/R, where c_{max} is the blade equatorial chord. Numerically, the second parameter is usually within 20% of the conventional solidity.

Figure 5-42 shows the effect of changes in Bc_{max}/R on the dimensionless power of a VAWT for various advance ratios. The geometry of the VAWT is that of the Sandia 17-m rotor described earlier, except for the chord dimension which is varied. The changes in rotor solidity (as measured by Bc_{max}/R) affect rotor performance in two ways. Largest of the effects is the fact that the increased chord results in larger aerodynamic forces and therefore in higher power. Although the axial induction increases and reduced local wind speeds offset some of the force increase caused by larger chords, the net effect of increasing the chord is an increase in power coefficient, except at very low advance ratios.

A second (and smaller) effect is caused by changes in *Reynolds number*. At a constant rotor speed, increasing the blade chord directly increases local Reynolds numbers. When the Reynolds number is less than one million, increases in performance with increases in Reynolds number are most noticeable.

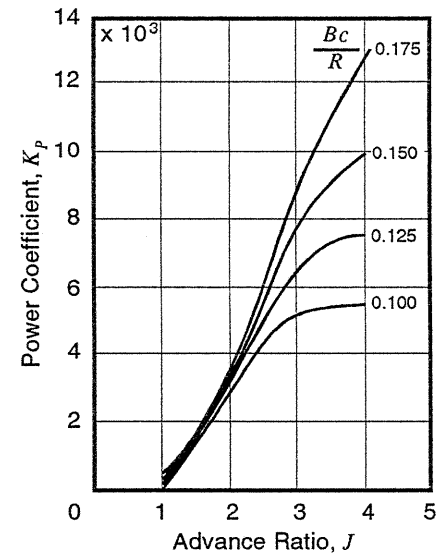

Figure 5-42. Typical effect of rotor solidity on the power coefficient of a VAWT. Rotor shape is that of the Sandia 17-m rotor, but blade chord is a variable.

Vortex Generators

Vortex generators have been employed on VAWTs as well as HAWTs to improve performance. The test power curves shown in Figure 5-43 are from three tests run on the *DAF Indal* 50-kW VAWT [Quinlan 1986]. The blades on this rotor were approximately 9 m long. The first test, without vortex generators, was made to establish the basic power curve of the turbine. A second test was made with vortex generators installed over 3 m of the equatorial section of each blade, on both surfaces. Finally, a third test was run with vortex generators placed over the entire blade length, again on both surfaces.

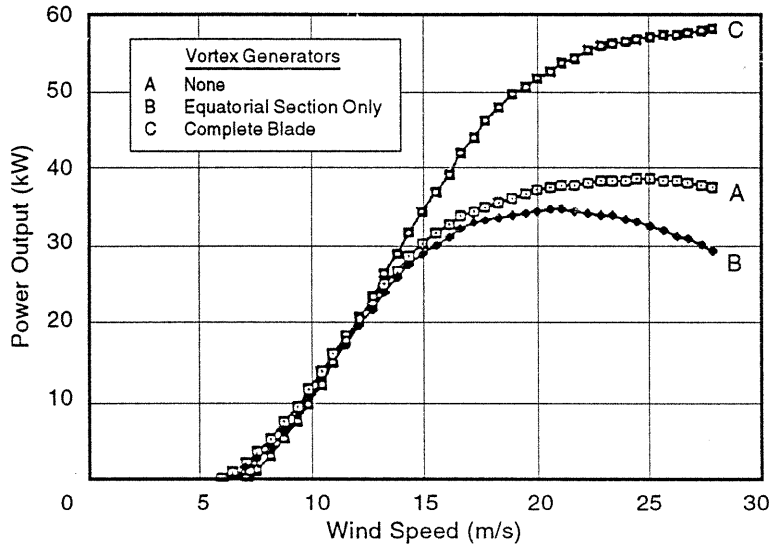

Figure 5-43. Effect of vortex generators on the power output of the DAF Indal 50-kW VAWT. [Quinlan 1986]

As shown in Figure 5-43, the basic power curve (*i.e.*, without vortex generators) exhibits the same flattening at high wind speeds as was observed during the slowest test on the Sandia 17-m VAWT discussed earlier (Fig. 5-38). As a result of placing vortex generators only on the equatorial sections of the blades, there was a reduction in power output over the entire range of wind speeds. At the highest wind speed in the test (22 m/s) the reduction reached over 20 percent. Utilization of vortex generators over the entire blade resulted in a small decrease in power output under low wind conditions, but a substantial increase in power output at high winds. The tip-speed ratio at the transition from power loss to power gain was about 5.

The conclusion drawn from these tests is that the vortex generators on the equator sections of a VAWT rotor will reduce power output, while vortex generators on the upper and lower portions of the blades (which are the regions of highest angles of attack) can increase power output by counteracting the "flattening" of the power curve at high wind speeds.

Starting and Stopping

Darrieus rotors require mechanical power input for starting, although they have been known to start by themselves (several VAWTs have been lost this way). The usual method of starting a VAWT is to run the generator as a motor. Motoring the rotor is required only to bring the VAWT up to a fraction of its rated speed, after which aerodynamic forces are sufficient to bring it up to operating speed. Auxiliary rotors, such as Savonius turbines, were tried on early VAWTs for starting, but this practice was discarded in favor of motor starting.

The process of stopping a VAWT in the absence of aerodynamic control surfaces is presently accomplished almost entirely by means of mechanical brakes. Aerodynamic brakes were attempted on the Canadian Eolé VAWT, but these were not successful, primarily because of their complexity and the fact that they had to operate reliably in the high acceleration environment of the rotor equator. Aerodynamic control surfaces such as flaps and air brakes have not been employed on U.S. VAWTs to date.

References

Abbot, I. H., A. E. von Doenhoff, and L. S. Stivers, Jr., 1945, *Summary of Airfoil Data*, NACA Report 824.

ASME, 1988, *Performance Test Code for Wind Turbines*, ASME/ANSI PTC 42-1988, New York: American Society of Mechanical Engineers.

Akins, R. E., March 1978, *Performance Evaluation of Wind Energy Conversion Systems Using the Method of Bins--Current Status*, SAND 77-1375, Albuquerque, New Mexico: Sandia National Laboratories.

Anderson, M. B., D. J. Milborrow, and N. J. Ross, April 1982, *Performance and Wake Measurements on a 3-m Diameter Horizontal Axis Wind Turbine*, DOE Contract Report No. E/5A/CON/1090/177/020, Cambridge, England: University of Cambridge.

Azuma, A., K. Nasu, and T. Kayashi, 1983, "An Extension of the Local Momentum Theory to Rotors Operating in a Twisted Flow Field," *Vertica*, Vol. 7, No. 1, pp. 45-49.

Berg, D. E., 1983, "Recent Improvements to the VDARTS VAWT Code," *Proceedings, 1983 Wind and Solar Energy Technology Conference*, Albuquerque, New Mexico: Sandia National Laboratories, pp. 31-41.

Betz, A., 1919, "Schraubenpropeller mit geringstem Energieverlust," *Göttinger Nachrichten, mathematisch-physikalische Klasse*: pp. 193-213.

Blackwell, B. F., and G. E. Reis, 1974, *Blade Shape for a Troposkien Type of Vertical-Axis Wind Turbine*, SLA74-0154, Albuquerque, New Mexico: Sandia National Laboratories.

Boeing, 1982, *Mod-2 Wind Turbine System Development Final Report, Vol. II Detailed Report,* NASACR-168007, DOE/NASA/0002-82/2, Cleveland, Ohio: NASA Lewis Research Center.

Bruynes, H., 1951, *Fluid Mixing Device*, U.S. Patent No. 2,558,816, Washington, DC: U.S. Patent Office.

de Vires, O., 1985, "Comment on the Yaw Stability of a Horizontal-Axis Wind Turbine at Small Angles of Yaw," *Wind Energy*, Vol. 9, No. 1: pp. 42-49.

Darrieus, G. J. M., 1931, *U.S. Patent No. 1,835,018*, Washington, DC: U.S. Patent Office.

Drzewiecki, S., 1892, "Sur une méthode pour la détermination des élements mécaniques des propulseurs hélicoidaux," *Comptes rendus de l'Académie des Sciences, Paris, 114*: pp. 820-822.

Dugundji, J., E. E. Larrabee, and P. H. Bauer, 1978, "Experimental Investigation of a Horizontal Axis Wind Turbine," *Wind Energy Conversion*, Vol. V, ASRL TR-184-11, Cambridge, Massachusetts: Massachusetts Institute of Technology.

Eggleston, D. M., and F. S. Stoddard, 1987, *Wind Turbine Engineering Design*, New York: Van Nostrand Reinhold: pp. 30-35.

Ensworth, C. B., 1985, "Comparison of Blade Loads for Aileron and Tip Controls," *Proceedings, Fourth ASME Wind Energy Symposium*, A. H. P. Swift, ed., New York: American Society of Mechanical Engineers, pp. 115-123.

Fanucci, J. B., and R. E. Walters, 1976, "Innovative Wind Machines: The Theoretical Performance of a Vertical Axis Wind Turbine," *Proceedings, Vertical-Axis Wind Turbine Technology Workshop*, SAND76-5586, Albuquerque, New Mexico: Sandia National Laboratories, pp. III 61-95.

Flamm, 1909, *Die Schiffschraube*, Berlin.

Froude, R. E., 1889. *Transactions, Institute of Naval Architects*, Vol. 30: p. 390.

Froude, W., 1878, "On the Elementary Relation between Pitch, Slip, and Propulsive Efficiency," *Transactions, Institute of Naval Architects*, Vol. 19: pp. 47-57.

Glauert, H., 1922a, *An Aerodynamic Theory of the Airscrew*, Reports and Memoranda, AE. 43, No. 786, London: Aeronautical Research Committee.

Glauert, H., 1922b, *Notes on the Vortex Theory of Airscrews*, Reports and Memoranda, No. 869, London: Aeronautical Research Committee.

Glauert, H., 1926, *The Analysis of Experimental Results in the Windmill Brake and Vortex Ring States of an Airscrew*, Reports and Memoranda, No. 1026, London: Aeronautical Research Committee.

Glauert, H., 1935a, *Aerodynamic Theory*, Vol. 6, Div. L, W. F. Durand, ed., Berlin: Julius Springer, p. 324.

Glauert, H., 1935b, "Airplane Propellers," *Aerodynamic Theory*, Vol. 4, Div. I, W. F. Durand, ed., Berlin: Julius Springer, pp. 169-360.

Gohard, J. D., Sept. 1978, *Free Wake Analysis of Wind Turbine Aerodynamics*, TR 184-14, Cambridge, Massachusetts: Massachusetts Institute of Technology.

Goldstein, S., 1929, "On the Vortex Theory of Screw Propellers," *Proceedings, Royal Society*, A 123: pp. 440-465.

Gormont, R. E., 1973, *A Mathematical Model of Unsteady Aerodynamics and Radial Flow for Application to Helicopter Rotors*, USAAMRDL TR 72-67.

Gyatt, G. W., 1986, *Development and Testing of Vortex Generators for Small Horizontal Axis Wind Turbines*, NASA CR-179514, DOE/NASA/0367-1, AV-FR-86/822, Cleveland, Ohio: NASA Lewis Research Center.

Hansen, A. C., 1992, *Yaw Dynamics of Horizontal-Axis Wind Turbines: Final Report*, NREL Technical Report 442-4822, Golden, Colorado: National Renewable Energy Laboratory.

Hansen, A. C., and C. P. Butterfield, 1993, "Aerodynamics of Horizontal-Axis Wind Turbines," *Annual Reviews of Fluid Mechanics*, Vol. 25, Palo Alto, California: Annual Reviews Inc., pp. 115-149.

Holme, O., 1976, "A Contribution to the Aerodynamic Theory of the Vertical-Axis Wind Turbine", *Proceedings,International Symposium on Wind Energy Systems*, Cambridge, England: St. John's College, pp. c4-55 - c4-72.

Jacobs, E. N., and A. Sherman, 1936, *Airfoil Section Characteristics as Affected by Variations of the Reynolds Number*, NACA Report 586, Hampton, Virginia: NASA Langley Research Center.

Jensen, S. A., P. Ingham, and P. A. Moller, 1986, "Aerodynamic Characteristics for Wind Turbine Blades and Air Brakes," *Proceedings, European Wind Energy Association Conference,* Rome, Italy.

Joukowski, N. E., 1912, *Soc. Math. Moscow*, reprinted in *Theorie Tourbillonnaire de l'Helice Propulsive*, Paris.

Joukowski, N. E., 1918, *Travanx du Bureau des Calculs et Essais Aeronautiques de l'Ecole Superieure Technique de Moscou.*

Kawada, S., 1926, Aeronautical Research Institute Report No. 14, Tokyo: Tokyo Imperial University.

Lanchester, F. W., 1907, *Aerodynamics*, London; see Bergey, K. H., 1980, "The Lanchester-Betz Limit," *Journal of Energy*, Vol. 3, No. 6: pp. 382-384.

Lock, C. N. H., H. Batemen, and H. C. H. Townsend, 1926, *An Extension of the Vortex Theory of Airscrews with Applications to Airscrews of Small Pitch, Including Experimental Results*, Aeronautical Research Committee Reports and Memoranda, No. 1014, London: Her Majesty's Stationery Office.

Massé, B., 1986, "A Local Circulation Model for Darrieus Vertical-Axis Wind Turbine," *Journal of Propulsion and Power*, Vol. 2, New York: American Society of Mechanical Engineers, pp. 135-141.

McKie, W. R., R. E. Wilson, and P. B. S. Lissaman, 1978, *Analytical Investigation of Darrieus Rotor Aerodynamics*, Chapter 2, Corvallis, Oregon: Oregon State University.

Miller, D. R., and P. J. Sirocky, 1985, "Summary of NASA/DOE Aileron-Control Development Program for Wind Turbines," *Proceedings, Windpower '85 Conference*, SERI/CP-217-2902, Washington, DC: American Wind Energy Association, pp. 537-545.

Miller, D. R., and R. D. Corrigan, 1984, *Shutdown Characteristics of the Mod-0 Wind Turbine with Aileron Controls*, NASA TM-86918, DOE/NASA/20320-61, Cleveland, Ohio: NASA Lewis Research Center.

Miller, R. H., 1979, "On the Weathervaning of Wind Turbines," *AIAA Journal of Energy*,Vol. 3, No. 5.

Muraca, R. J., S. Stephen, V. Maria, and R. J. Dagenhart, 1975, *Theoretical Performance of Vertical Axis Windmills*, NASA TM TMX-72662, Hampton, Virginia: NASA Langley Research Center.

Parashiviou, I., 1981, "Double-Multiple Streamtube Model for Darrieus Wind Turbines," *Proceedings, Wind Turbine Dynamics Workshop*, NASA CP-2185, DOE Publication CONF-810226, SERI/CP-635-1238, R.W. Thresher, ed., Cleveland, Ohio: NASA Lewis Research Center, pp. 19-25.

Pistolesti, E., 1922, *Vortrage aus dem Gebiete der Hydro- und Aerodynamik*, Innsbruck: .

Prandtl, L., 1919, Appendix to [Betz 1919]: pp. 213-217.

Quinlan, P. J., 1986, Private Communication.

Rankine, W. J. M., 1865, "On the Mechanical Principles of the Action of Propellers," *Transactions, Institute of Naval Architects*, Vol. 6: pp. 13-30.

Savino, J. M., T. W. Nyland, and A. G. Birchenough, 1985, *Reflection Plane Tests of a Wind Turbine Blade Tip Section with Ailerons*, NASA TM-87018, DOE/NASA 20320-65, Cleveland, Ohio: NASA Lewis Research Center.

Shankar, P. N., 1975, *On the Aerodynamic Performance of a Class of Vertical Axis Windmills*, AE TM-13-15, Bangalore, India: National Aeronautical Laboratory.

Sheldal, R. E., and P. C. Klimas, 1981, *Aerodynamic Characteristics of Seven Symmetrical Airfoil Sections Through 180-Degree Angle of Attack for Use in Aerodynamic Analysis of Vertical Axis Wind Turbines*, SAND80-2114, Albuquerque, New Mexico: Sandia National Laboratories.

South, P., and R. S. Rangi, 1972, *A Wind Tunnel Investigation of a 14-ft Diameter Vertical Axis Windmill*, NRC Laboratory Technical Report LTR-LA-105, Ottawa: National Research Council of Canada.

Strickland, J. H., 1975, *The Darrieus Turbine: Performance Prediction Model Using Multiple Streamtubes*, SAND75-0431, Albuquerque, New Mexico: Sandia National Laboratories.

Strickland, J. H., B. T. Webster, and T. Nguyen, 1980, *A Vortex Model of the Darrieus Turbine: An Analytical and Experimental Study*, SAND79-7058, Albuquerque, New Mexico: Sandia National Laboratories.

Spera, D. A., and D. C. Janetzke, 1981, "Performance and Load Data from Mod-0A and Mod-1 Wind Turbine Generators," *Proceedings, Workshop on Large Horizontal-Axis Wind Turbines*, NASA CP-2230, R.W. Thresher, ed., Cleveland, Ohio: NASA Lewis Research Center, pp. 447-467.

Sullivan, T. L., 1984, *Effect of Vortex Generators on the Power Conversion Performance and Structural Dynamic Loads of the Mod-2 Wind Turbine*, NASA TM-83680, DOE/NASA/20320-59, Cleveland, Ohio: NASA Lewis Research Center.

Taylor, H. D., 1947, *The Elimination of Diffuser Separation by Vortex Generators*, Report R-4012-3, East Hartford, Connecticut: United Aircraft Corporation.

Templin, R. S., 1974, *Aerodynamic Performance Theory for the NRC Vertical-Axis Wind Turbine*, LTR-160, Ottawa: National Research Council of Canada.

Touryan, K. J., J. H. Strickland, and D. E. Berg, 1987, "Electric Power from Vertical-Axis Wind Turbines," *Journal of Propulsion*, Vol. 3, No. 6: pp. 481-493.

Viterna, L. A., and R. D. Corrigan, 1981, "Fixed Pitch Rotor Performance of Large Horizontal Axis Wind Turbines," *Proceedings, Workshop on Large Horizontal-Axis Wind Turbines*, NASA CP-2230, R. W. Thresher, ed., Cleveland, Ohio: NASA Lewis Research Center, pp. 69-85.

Wentz, W. H. Jr., M. H. Snyder, and J. T. Calhoun, 1980, *Feasibility Study of Aileron and Spoiler Control Systems for Large Horizontal Axis Wind Turbines*, NASA CR-159856, DOE/NASA/3277-1, WER-10, Cleveland, Ohio: NASA Lewis Research Center.

Wilson, R. E., 1978, "Vortex Sheet Analysis of the Giromill," *Transactions, ASME Journal of Fluids Engineering*, Vol. 100.

Wilson, R. E., and P. B. S. Lissaman, 1974, *Applied Aerodynamics of Wind Power Machines*, Corvallis, Oregon: Oregon State University.

Wilson, R. E., P. B. S. Lissaman, and S. N. Walker, 1976, *Aerodynamic Performance of Wind Turbines*, ERDA/NSF/04014-76/1, Washington, DC: U.S. Department of Energy.

Wilson, R. E., and S. N. Walker, 1981, *Fixed Wake Analysis of the Darrieus Rotor*, SAND81-7026, Albuquerque, New Mexico: Sandia National Laboratories.

Wilson, R. E., and S. N. Walker, 1984, *Performance Analysis of Horizontal Axis Wind Turbines*, Corvallis, Oregon: Oregon State University.

Wilson, R. E., and J. A. Neff, 1985, *A First Order Analysis of the Effect of Pitching on the Drag Coefficient*, SAND85-7003, Albuquerque, New Mexico: Sandia National Laboratories.

Wilson, R. E., L. N. Freeman, and S. N. Walker, 1994, "Parametric Analysis of a Teetered Rotor Model," *Proceedings, Thirteenth ASME Wind Energy Symposium*, W. Musial, ed., New York: American Society of Mechanical Engineers.

Worstell, M. H., 1979, *Aerodynamic Performance of the 17-Meter-Diameter Darrieus Wind Turbine*, SAND78-1737, Albuquerque, New Mexico: Sandia National Laboratories.

Worstell, M. H., 1980, "Measured Aerodynamic and System Performance of the 17-Meter Research Machine," *Proceedings, Vertical Axis Wind Turbine Design Technology Seminar for Industry*, S. Johnston, ed., SAND80-0984, Albuquerque, New Mexico: Sandia National Laboratories, pp. 233-258.

6

Wind Turbine Airfoils and Rotor Wakes

Peter B. S. Lissaman, Ph.D.
Adjunct Professor of Aerospace Engineering
University of Southern California
Los Angeles, California

Introduction

In this chapter we will discuss the detailed characteristics of the *lifting surfaces* which we know as *airfoils*, in order to provide guidance in the selection of airfoil shapes that will perform satisfactorily over the broad operating environment of a wind turbine. In addition, the fundamental fluid-dynamic principles involved in modeling the structure of rotor wakes and integrating wake-induced effects over an array of turbines are presented in this chapter.

Wind turbines operate by the action of the *relative wind* (the natural wind plus wind caused by rotor motion and rotor-induced flow), which creates aerodynamic forces on the rotating blades. These can normally be grouped into *lift-like forces* and *drag-like forces*. Lift forces operate through the generation of *circulation* and do not involve large viscous losses in the flow and the associated loss of *total head*, while drag forces function through *flow separation* on the blade and the loss of total head. In the previous chapter, the relative merits of lift and drag power devices were discussed, with lift being the clear preference for wind turbine rotors. When considering the potential impact of wakes on the total output of a wind power station, a lift-type device is again preferred, since a drag-type unit develops a greater wake and less energy is available to downwind units. Thus, the array efficiency of a cluster of drag-type units will be lower than that of lift-type turbines.

Designing lift-type wind energy conversion systems depends on a knowledge of the properties of airfoils. There is extensive experience in airfoil technology, derived primarily from airplane wing design. It is normally assumed that the properties of airfoils that are desirable for wings will also be desirable for wind turbines. This assumption is only superficially valid, for reasons described later. It must be noted that fixed-pitch wind turbine airfoils generally operate over angles of attack ranging from 0 deg to 90 deg, and thus their *stall* and *post-stall behavior* are important. This situation does not apply for aircraft wings, which seldom require operation at angles in excess of 30 deg.

An excellent review of wind turbine airfoils and their properties is given by Miley [1980]. Included here are many of the airfoils that wind turbine designers have borrowed from the aircraft industry. More recently, Tangler [1987] has described the development of several families of airfoils designed specifically for HAWTs.

Airfoils are designed to generate lift; that is, to create a force normal to the incident flow when immersed in this flow at a small angle to the airfoil's *chord line*. The geometry of this flow and the forces created are shown in Figure 6-1. The angle from the *relative velocity* vector. V_r, to the chord line is the *angle of attack*, α. The lift force is normal to V_r. Generally this lift is produced simultaneously with a streamwise force at right angles to itself, called the drag. These forces are normalized by dividing the force per unit span by the *dynamic pressure* and the chord length to obtain *lift* and *drag coefficients*, C_L and C_D, in accordance with Equations (5-3).

Characteristic Behavior of Airfoils

Reynolds Number

The most significant flow factor influencing the behavior of low-speed airfoils is that of *viscosity*, which indirectly causes lift and directly causes drag and *flow separation*. This influence is characterized by the *Reynolds number* of the airfoil/fluid combination. For the airfoil in Figure 6-1, Reynolds number can be calculated as follows:

$$N_R = \frac{V_r c}{\nu} \approx \left(\frac{r\Omega}{30\ m/s}\right)\left(\frac{c}{0.5\ m}\right) x\,10^6 \approx \left(\frac{r\Omega}{110\ mph}\right)\left(\frac{c}{1.0\ ft}\right) x\,10^6 \qquad (6\text{-}1)$$

where

ν = kinematic viscosity of air (m^2/s)
V_r = relative velocity (m/s)
$r\Omega$ = local tangential velocity (m/s or mph)
c = chord length (m or ft)

Airfoils in use on modern turbines range in representative chord size (typically at 3/4 span) from about 0.3 m (1 ft) on a small-scale turbine to over 2 m (7 ft) on a megawatt-scale rotor. Tip speeds typically range from approximately 45 to 90 m/s (100 to 200 mph), so tangential velocities at the 3/4-span of a HAWT blade can be estimated to range from about 34 to 68 m/s (75 to 150 mph). For turbine airfoils, then, Reynolds numbers range from about 10 million down to 0.7 million. This implies that turbine airfoils generally operate beyond the sensitive, low Reynolds number range (often taken to be below 0.5 million) in which extreme and unusual behavior is caused by anomalous *transition, separation,* and *bubble formation* phenomena. In this sensitive range, very large changes in airfoil behavior

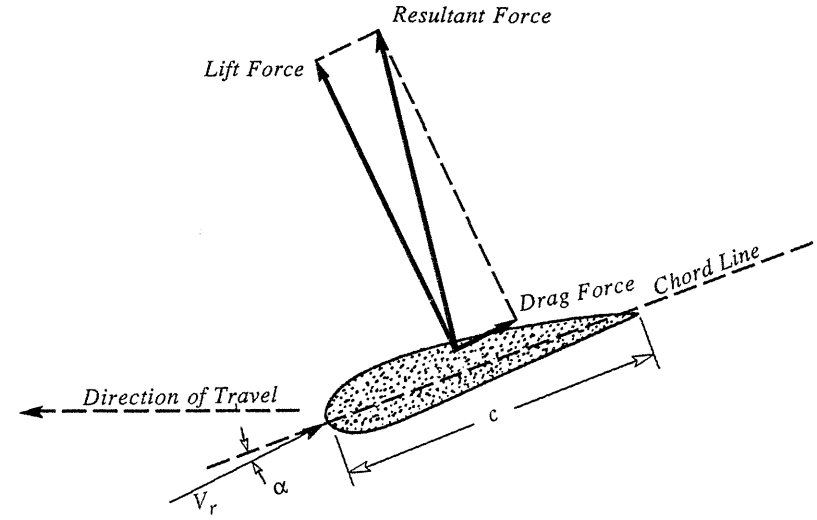

Figure 6-1. Typical airfoil geometry and aerodynamic forces.

can be induced by minor events, like changes in incoming flow turbulence, vibrating the airfoil itself, or roughness on the surface [Lissaman 1983]. Fortunately, this type of irregular airfoil behavior is not usually encountered with wind turbines, so it will not be necessary to discuss it further.

Typical Airfoil Lift and Drag Behavior

Generally, airfoil behavior is characterized by three flow regimes, as illustrated by the wind tunnel test data in Figure 6-2 for a representative quadrant of angle of attack, α. The first of these is the *attached regime*, for angles of attack from about -15 to +15 deg; the second is the *high-lift/stall-development* regime, for angles of attack between about 15 and 30 deg; and, thirdly, the *flat-plate, fully-stalled,* or *deep-stall* regime with attack angles between 30 and 90 deg. These regimes are repeated in the other three quadrants, with approximate symmetry for drag and anti-symmetry for lift.

Attached Flow Regime

In the attached flow regime, the general airfoil behavior is well understood. Although it can be complicated and significantly affected by geometrical and viscous parameters like *thickness, camber, nose radius, trailing edge angle, surface roughness*, and *Reynolds number*, airfoil behavior in the attached flow regime can be very accurately estimated by the wealth of theory and data accumulated in a half-century of refining two-dimensional airfoil theory for application to wings. Methods exist for accurate analytical estimation of the lift and drag forces in this regime, and there is also an extensive literature presenting experimental data. The upper end of the attached flow regime, around an angle of attack

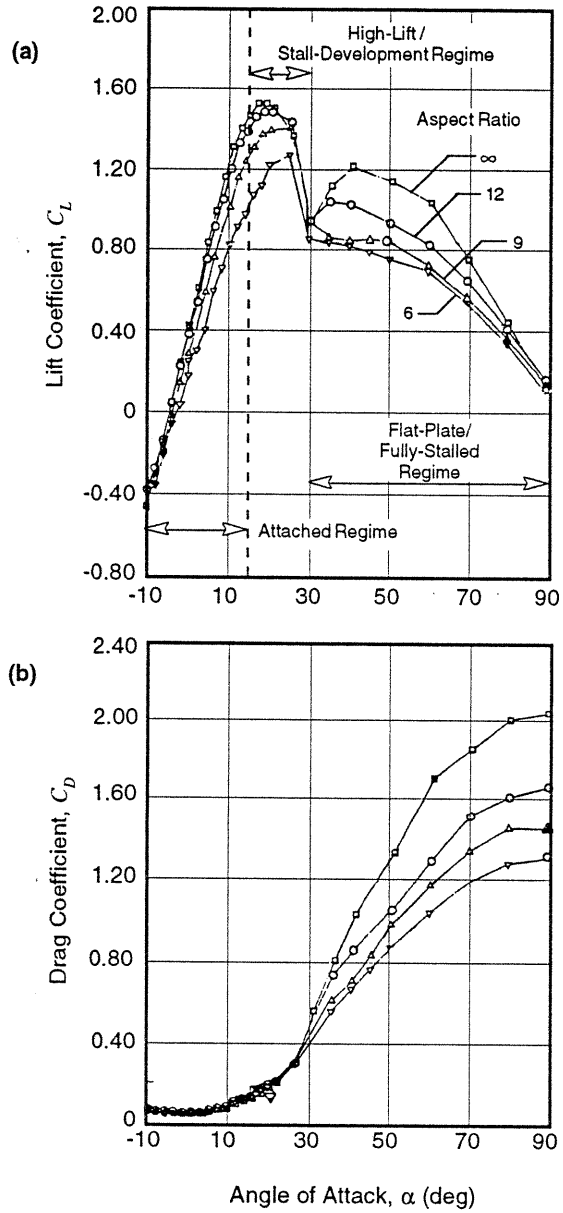

Figure 6-2. Typical variation of airfoil lift and drag coefficients with angle of attack and aspect ratio, illustrating the flow regimes used to characterize airfoil behavior. (a) Lift coefficients for an *NACA 4415* airfoil tested at a Reynolds number of 0.5 million. (b) Drag coefficients for the same airfoil [Ostowari and Naik 1984]

of 15 deg, is the region where separation and incipient stall generally commence. While the initial stages of stall are quite sensitively connected to details of the airfoil shape, the features of incipient stall are well-documented in the standard literature.

A basic insight into the effect of drag in the attached-flow regime on the power of a HAWT can be obtained by taking an approach similar to that used in the fundamental analysis of the performance of monoplane wings, that is, by calculating the ideal power without viscous or *profile drag* losses and then estimating the power losses caused by drag alone. A simple analysis of a constant chord HAWT rotor with a constant drag coefficient at zero lift coefficient indicates that

$$\delta P_V \approx \frac{\rho B c \Omega^3 R^4}{8} C_{D,0} \tag{6-2}$$

where

δP_V = viscous power loss (W)
ρ = air density (kg/m^3)
B = number of blades in the rotor
Ω = rotor speed (rad/s)
R = rotor radius (m)
$C_{D,0}$ = drag coefficient at zero lift coefficient; profile drag coefficient

For tapered blades, the effective chord length is approximately that at about 80% of the rotor radius. As an example, consider a representative small-scale turbine, the *Carter 25* HAWT shown in Figure 4-11(e), for which $B = 2$, $\Omega = 12.6$ rad/s, $R = 4.9$ m, $c = 0.31$ m, and $C_{D,0} = 0.009$. This provides a representative viscous power loss of 1.0 kW at all wind speeds. If we compare this with the rated power of 25 kW, we note that it is about 4% of that value. This estimate can be refined by using a state-of-the-art rotor performance code, taking into account details of chord and twist distributions and the air loading. When the actual drag coefficient is reduced by $C_{D,0}$ at all angles of attack, the improvement in power output is predicted to be roughly constant at 1.0 kW over the operating range, which is equal to the crude estimate above.

At a site with a typical *Weibull wind speed histogram* (Table 2-1), this represents an 8% energy loss from viscous effects. It should be noted that most well-sited turbines produce the majority of their energy when operating near their maximum power coefficient, so this energy loss estimate is accurate to a first order. For turbines generating power in a low wind regime, energy production will be more heavily impacted by airfoil drag.

High-Lift/Stall-Development Regime

This next regime involves airfoil behavior at angles of attack from approximately 15 to 30 deg. Designers of fixed-pitch turbines pay special attention to lift and drag coefficients in this regime, since these have a dominant effect on the peak power produced by the rotor. Here the flow state ranges from initial incipient separation near the trailing edge of the airfoil to massive separation over its entire low-pressure surface. The phenomenon of *dynamic stall* [Hibbs 1986] also takes place in this regime.

Flat-Plate/Fully-Stalled Regime

Airfoil behavior at angles of attack from approximately 30 to 90 deg is similar to that of a simple flat plate. At 45 deg, lift and drag coefficients are approximately equal, and

lift approaches zero near 90 deg. Like a flat plate, the drag coefficients in Figure 6-2(b) show a significant effect of *aspect ratio* (span length divided by chord width), with the low aspect ratio case significantly lower in drag than the two-dimensional (*i.e.*, infinite length) situation.

It is further noted that the post-stall flow over the airfoils of an actual rotor experiences two additional fluid-dynamic effects that are not represented in typical wind-tunnel tests. One is the effect of *spanwise flow* caused by rotational effects. Generally, this will produce a flow towards the blade tip, and the normal expectation is that this postpones stall nearer the axis of rotation. Swept aircraft wings show a similar effect, with the spanwise component of the flow causing the wing tips to stall prematurely. No rational quantitative analysis is available to account for this. The second difference relates to the generally *non-uniform spanwise loading* on an actual rotor blade. A spanwise-constant lift coefficient is seldom achieved, so stall will develop differently at different radial stations along the blade. Again, no acceptable procedure is available to handle the influence of spanwise loading variations on stall. The usual procedure is to assume each section behaves independently, which effectively ignores spanwise interaction of sections.

Aspect Ratio Effects

The data in Figure 6-2 clearly indicate that lift and drag characteristics show a significant aspect-ratio dependence at angles of attack larger than 30 deg. In the fully-attached regime, airfoil section characteristics are not greatly affected by aspect ratio, so that two-dimensional (*i.e.* infinite aspect ratio) data can be used in predicting performance at low angles of attack. However, when two-dimensional data are used, a *tip-loss factor* must be added, as described in Equations (5-35) and (5-36).

The size of the aspect-ratio effects on airfoil coefficients in the attached regime can be estimated using the classical equations for correcting wind tunnel test data measured on a finite-span airfoil, from the work of Munk, Glauert, and Prandtl [Jacobs and Abbot 1932]. In this case we are using these equations in reverse, starting from infinite-span data and obtaining lift and drag curves for a finite aspect ratio. These formulas are as follows:

$$C_L = C_L' \tag{6-3a}$$

$$C_D = C_D' + \frac{C_L^2}{\pi \mu} \tag{6-3b}$$

$$\alpha = \alpha' + \frac{57.3\, C_L}{\pi \mu} \tag{6-3c}$$

where

C_L', C_D' = lift and drag coefficients for an infinite aspect ratio
C_L , C_D = lift and drag coefficients for a finite aspect ratio
μ = aspect ratio

In Equations (6-3b) and (6-3c), minor corrections for the shape of the pressure distribution on the airfoil (rectangular *vs.* elliptical) have been eliminated for convenience. Inspection of these equations shows that finite length increases the angle of attack and the drag coefficient for a given lift coefficient. Conversely, the lift coefficient is reduced for the same angle of attack. From Figure 6-2, it is found that stall occurs at a lower lift

coefficient for low aspect ratios (which is not predicted by Equations (6-3)), and that the same situation (*i.e.*, a lower separated-lift coefficient) persists as the angle of attack increases beyond the stall point.

Post-Stall Modeling of Lift and Drag Coefficients

As previously noted, the airfoils in *fixed-pitch rotors* (used in *stall-controlled* HAWTs and most VAWTs) will operate over all three of the flow regimes in Figure 6-2. In order to accurately predict the peak power of a fixed-pitch rotor, it is particularly important to know the details of lift and drag behavior in the high lift/stall development regime. An empirical model for modifying two-dimensional airfoil data in all three regimes to more accurately represent wind turbine rotor behavior has been developed by Viterna and Corrigan [1981]. This model is based on the following three assumptions:

- -- In the attached flow regime, Equations (6-3) adequately model end effects in terms of the blade aspect ratio, and no tip- or hub-loss models are needed.
- -- In the high-lift/stall-development regime, the *torque force* (sometimes called the *suction force*) on the element, acting in the plane of rotation, does not decrease with increasing angle of attack; rather, it is independent of angle of attack.
- -- In the flat-plate/fully-stalled regime, the dominant parameter is the maximum value of the drag coefficient, and this is determined by the blade aspect ratio.

The equations which implement these assumptions in the *Viterna-Corrigan post-stall model* are as follows:

$\alpha \geq \alpha_s$:

$$C_L = \frac{C_{D,\max}}{2} \sin 2\alpha + K_L \frac{\cos^2 \alpha}{\sin \alpha} \tag{6-4a}$$

$$C_D = C_{D,\max} \sin^2 \alpha + K_D \cos \alpha \tag{6-4b}$$

$$K_L = (C_{L,S} - C_{D,\max} \sin \alpha_S \cos \alpha_S) \frac{\sin \alpha_S}{\cos^2 \alpha_S} \tag{6-4c}$$

$$K_D = \frac{C_{D,S} - C_{D,\max} \sin^2 \alpha_S}{\cos \alpha_S} \tag{6-4d}$$

$$\mu \leq 50: \quad C_{D,\max} = 1.11 + 0.018\, \mu$$
$$\mu > 50: \quad C_{D,\max} = 2.01 \tag{6-4e}$$

where

$C_{D,max}$ = maximum drag coefficient in the fully-stalled regime

To illustrate the application of Equations (6-3) and (6-4), Viterna and Corrigan [1981] analyzed the power output of the historic *Gedser* wind turbine, shown in Figure 3-1. The

blades of this rotor are *Clark Y* airfoils with an aspect ratio of six. Figure 6-3 shows the modification of the unstalled two-dimensional lift and drag curves for this airfoil [Silverstein 1934] to represent an aspect ratio of six, in accordance with Equations (6-3). At the stall angle of 15.9 deg, these curves are coupled with the Viterna-Corrigan model of post-stall behavior. The power curves in Figure 6-4 show the effect of these changes on calculated power, compared to test data from [Lundsager *et al.* 1980].

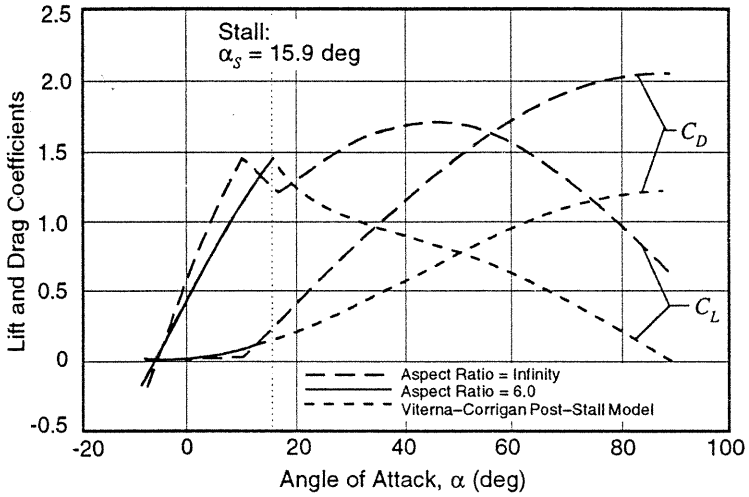

Figure 6-3. Two-dimensional and modified lift and drag curves for Clark Y airfoils.

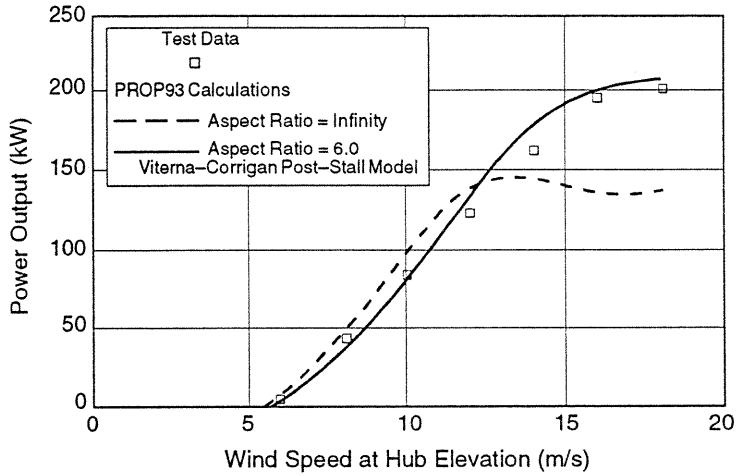

Figure 6-4. Measured output power of the Gedser 200-kW wind turbine compared to power curves calculated by two methods. [Viterna and Corrigan 1981]

Rotor power was calculated using a computer model derived from the original *PROP* code for predicting wind turbine aerodynamic performance [Wilson *et al.* 1976]. The latest version of this is the *PROP93* computer code [McCarty 1993]. Power train losses were estimated using the following general loss model [Spera and Janetzke 1981] and deducted from the rotor power:

$$P_{PT} = -a\,P_{G,R} - (b + s)\,P_R \tag{6-5a}$$

For the Gedser wind turbine:

$$\begin{aligned} a &\approx 0.055 \\ P_{G,R} &= 200\ kW \\ b &\approx 0.040 \\ s &\approx 0.050 \end{aligned} \tag{6-5b}$$

where

P_{PT} = power-train loss (kW)
a, b = empirical constants from tests on the 200-kW Mod-0A wind turbine
$P_{G,R}$ = rated power of the generator (kW)
s = slip in the generator
P_R = rotor power (kW)

The dashed power curve in Figure 6-4 is the result of calculations based on two-dimensional airfoil data and *Prandtl* tip- and hub-loss models. The solid power curve illustrates how the correlation between the calculated and measured peak powers of a fixed-pitch rotor can often be significantly improved by modifying lift and drag curves in accordance with Equations (6-3) and (6-4). This is an important achievement, since the accurate determination of this peak power controls the design of the gearbox and generating equipment and is thus a primary driver of the cost of a fixed-pitch turbine.

Airfoil Aerodynamic Requirements

There are evidently many engineering requirements entering into the selection of a wind turbine airfoil. These include primary requirements related to *aerodynamic performance, structural strength and stiffness, manufacturability,* and *maintainability*. Requirements related to other rotor characteristics like electromagnetic interference, acoustic noise generation, and aesthetic appearance are generally assumed to be of secondary importance. Here we refer only to aerodynamic aspects, although we note that the critical wind turbine performance and reliability features associated with *aeroelastic behavior* (changes in angle of attack caused by blade deflections) introduce a strong coupling between aerodynamic and structural requirements.

Lift and Drag Requirements

The usual assumption, historically established in airplane lifting surface theory, is that high lift and low drag are desirable for an airfoil, and that the *lift-to-drag ratio* (often abbreviated as *L/D*) is a critical consideration. For wind turbine rotors this point of view is not of the same importance as it is for aircraft wing design. General analysis of rotor performance shows that the primary factor is the product of the chord and the lift coefficient, or cC_L. Thus, when other characteristics like tip-speed ratio and diameter are

held constant, operating at a higher lift coefficient will permit the use of narrower blades. Generally, this will not result in lower viscous power losses, since viscous torque is controlled more by the L/D ratio of the airfoil than the actual value of lift.

The principal factor controlling the lift-to-drag ratio of a given airfoil section is the Reynolds number. Since a smaller chord reduces Reynolds number in accordance with Equation 6-1, this is an aerodynamic reason to avoid narrow-chord blades. Another factor relating to the use of narrower blades is the negative effect on structural stiffness, which reduces rapidly as thickness decreases. Stiffness is approximately proportional to the square or the cube of the thickness, and thickness is proportional to the chord.

Drag coefficient is of limited importance in determining turbine performance in the usual operating range of wind speeds and at normal tip-speed ratios. Generally, its effect on the power coefficient varies directly with the cube of the tip-speed ratio. When this ratio is high (in excess of 10, typically) the drag coefficient does become somewhat more significant. This situation occurs in lower wind ranges when it may be more important to maximize energy extraction.

Surface Roughness Effects

An important operating requirement that relates to a wind turbine airfoil is its ability to perform when the smoothness of its surfaces has been degraded by dust, dirt, rain, or insect debris. Field experience with small- and medium-scale units has indicated that very severe performance degradation can occur in these circumstances. Figure 6-5 shows field test power curves for a small-scale (10-m dia.) HAWT with both clean and dirty blades. It appears that this deleterious effect is most pronounced in fixed-pitch stall-controlled rotors, and that it is caused by the surface roughness precipitating blade stall at a relatively low lift coefficient. Consequently, peak power occurs at a lower tip-speed ratio than that for which the stall control was designed. Large-scale rotors are less affected because of their higher elevation (above most insects and dust particles) and because debris thicknesses are smaller fractions of the leading-edge radius and the airfoil thickness.

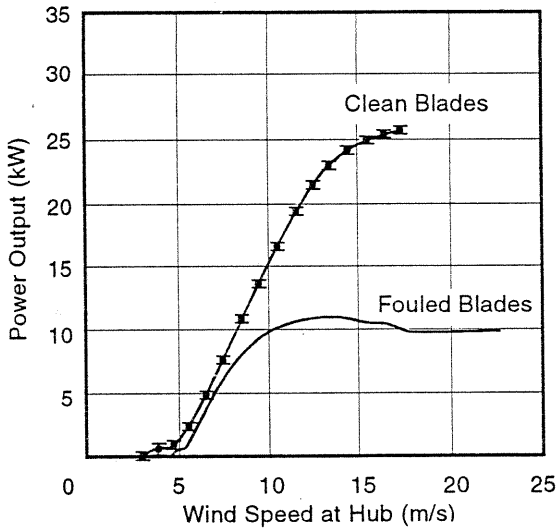

Figure 6-5. Effect of blade fouling by dust, dirt, and insects on the performance of a small-scale HAWT 10-m in diameter.

Airfoil Selection

In the present state of the art there is no unambiguous, rational procedure to determine the ideal airfoil for a given wind turbine rotor, or even for a given radial station on a blade. This is the result of both the very wide range of angles of attack over which a blade operates and the widely different geometrical combinations of airfoil section, chord, and twist possible in the blade design. A further factor relates to the differing spanwise aerodynamic requirements of the general rotor. For these reasons the current approach in airfoil selection is to use a rotor performance computer code [*e.g.*, Wilson *et al.* 1976, Tangler 1987, McCarty 1993] that takes into account (as adequately as possible) all the forces on the rotor that vary with tip-speed ratio and radial position. The aerodynamicist can then vary the rotor geometry until an acceptable performance results. Inherent in this process is the assumption that the analytical models in the code properly account for the effects of these geometric changes on performance.

Standard Aircraft Airfoils

Many different standard airfoils developed for aircraft have been used on wind turbines with no special advantages from any particular choice when only the impact of the basic airfoil properties on power output is considered. Five of these are shown in Figure 6-6. The *NACA 230XX series* and the *NACA 44XX series* airfoils (where the XX stands for the thickness-to-chord ratio, in percent) have been used on many modern HAWT units, with thickness-to-chord ratios varying from about 28% at the root to about 12% at the tip. In some respects, these standard airfoils have unsatisfactory characteristics. For example, airfoils in the NACA 230XX series have maximum lift coefficients that are very sensitive to surface fouling, and their performance deteriorates with increased thickness more rapidly than that of other airfoils.

NACA 63-2XX series airfoils have demonstrated the best overall performance characteristics of the NACA families, and they provide reasonable resistance to roughness losses. Airfoils in the *LS(1)-04XX series* were designed to tolerate surface fouling, but HAWTs with these airfoils (*e.g.*, the *ESI 80* and *Carter 300*) have experienced large power losses induced by roughness. This airfoil series also has a very high nose-down pitching moment which can result in excessive elastic blade twist in thin blades and undesirable performance changes.

For most VAWTs, a symmetrical airfoil such as the four-digit series *NACA 00XX* is normally used, with thickness ratios varying from 12% to 15%.

Current Designs of Airfoils for Wind Turbines

Special airfoils designed for wind turbine applications have been developed during the past 10 years. A class of these for HAWTs is described by Tangler and Somers [1985] and Tangler [1987], while some airfoils specially tailored for VAWTs are described by Klimas [1984]. Typical design goals for new HAWT airfoils are

- -- a stable $C_{L,max}$ at stall, despite blade fouling;
- -- larger lift-to-drag ratios;
- -- limited $C_{L,max}$ at outboard sections, for control of peak power in high winds.

As we noted previously, the numerous different demands made of airfoil sections along the span of a wind turbine blade preclude the possibility of the design of a single airfoil

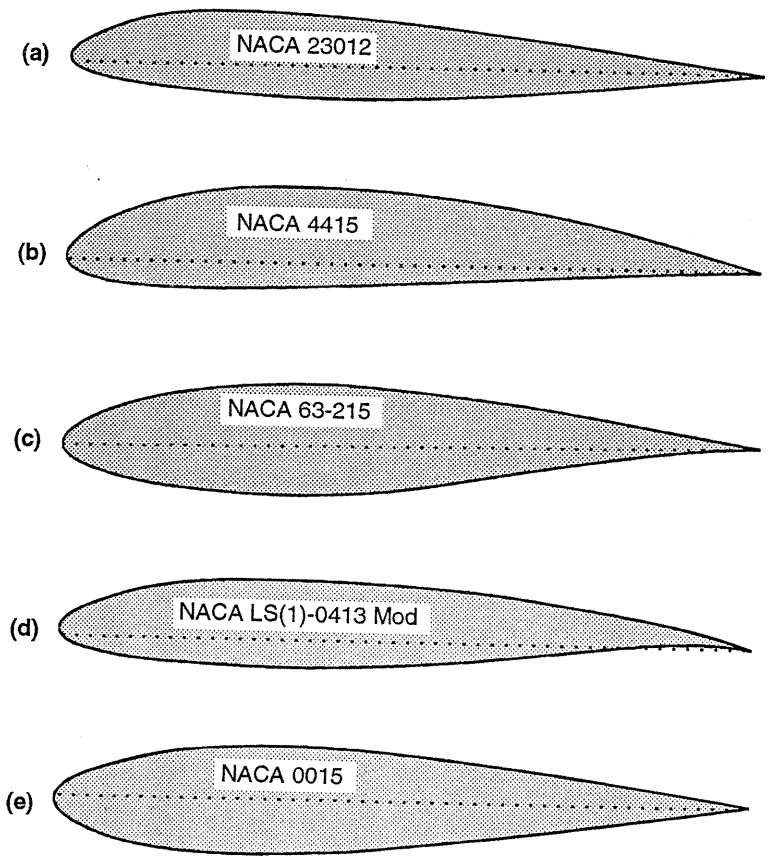

Figure 6-6. Common wind turbine airfoils, designed originally for aircraft. (a) NACA 23012 (b) NACA 4415 (c) NACA 63-215 (d) NASA LS(1)-0413 Modified (e) NACA 0015

which might be "ideal" in all senses. However, if a limited class of wind turbines is defined, it then becomes possible to specify airfoil requirements for the rotors of this class. The spanwise variation in requirements may be accounted for by specifying different lift and drag properties (and consequently different airfoil sections) at different radial locations. The definition of a rotor class provides us with input for which rotor performance codes may be run, so that the relative performance with different airfoil sections may be calculated and evaluated. Airfoil contours are shaped to produce the desired flow characteristics at selected radial stations using state-of-the-art analysis tools such as the *Eppler code* [Eppler and Somers 1980].

HAWT Rotors 10 m to 30 m in Diameter

Tangler and Somers [1986] have applied this concept to the development of airfoils for a large class of modern wind turbines with the following characteristics:

- -- system designs optimized for a site with an annual average wind speed between 4.5 and 6.2 m/s at an elevation of 10 m;
- -- rotor diameters between 10 and 30 m;
- -- fixed-pitch stall-controlled blades;
- -- peak power coefficients at tip-speed ratios of approximately 8.

The contours of three airfoils designed for specific locations in the blades of this class of HAWTs are shown in Figure 6-7 [NREL 1994].

Assuming that the main power generating region of the blade is centered on a station at about 75 percent of the radius (*i.e.*, $r/R \approx 0.75$) we desire the airfoil at this primary outboard station to have a relatively high lift-to-drag ratio (to maximize the power coefficient), a limited maximum lift coefficient (to assure reliable stall control, particularly at a low-wind site), a low sensitivity of stall to surface roughness (to ensure that stall control behavior remains constant), and an appreciable thickness-to-chord ratio (to retain desirable structural stiffness and weight). An airfoil designated the *SERI S805A* has been designed to meet these requirements, with the contour shown in Figure 6-7(b) [Tangler and Somers 1986, Tangler 1987].

In Table 6-1 the basic properties of this new airfoil are compared with those of three conventional wing airfoils of comparable thickness, for a representative Reynolds number of one million. It is noted from these data that the lift-to-drag ratio (and hence the performance) of the SERI S805A is comparable to that of the high-performance standard

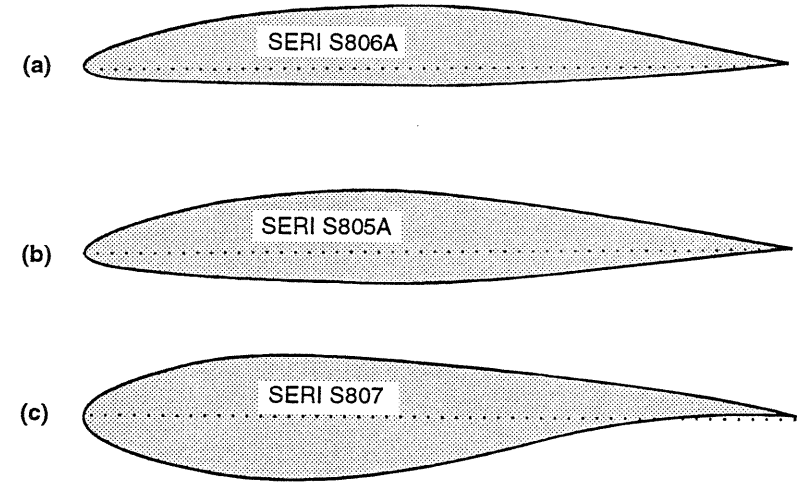

Figure 6-7. Contours of the SERI S805A/S806A/S807 series of airfoils designed specifically for fixed-pitch HAWTs with diameters from 10 m to 20 m. (a) Tip region ($r/R \approx 0.95$) (b) Primary outboard airfoil ($r/R \approx 0.75$) (c) Root region ($r/R \approx 0.40$) [Tangler and Somers 1986, NREL 1994]

airfoils such as the NACA 4415 and the LS(1)-0413 Mod. The SERI S805A also has the lowest $C_{L,max}$, to prevent overpowering the generator of a fixed pitch turbine in high winds. Unlike the NACA 4415, the $C_{L,max}$ of the new airfoil has minimal sensitivity to surface roughness. This can be a pronounced performance advantage, as illustrated in Figure 6-5.

Table 6-1.
Properties of the *SERI S805A* Airfoil Compared to Standard Wing Airfoils
[Tangler and Somers 1986]

Airfoil $N_R = 1 \times 10^6$	Thickness ratio	Max. lift coefficient	Min. drag coefficient	Lift-to-drag ratio at $C_L = 0.7$	Moment coef. at $\alpha = 0$
SERI S805A	0.135	1.2	0.007	90	- 0.05
NACA 4415	0.150	1.4	0.009	85	- 0.08
NACA 23012	0.120	1.3	0.009	70	- 0.01
LS(1)-0413 Mod	0.130	1.5	0.008	86	- 0.10

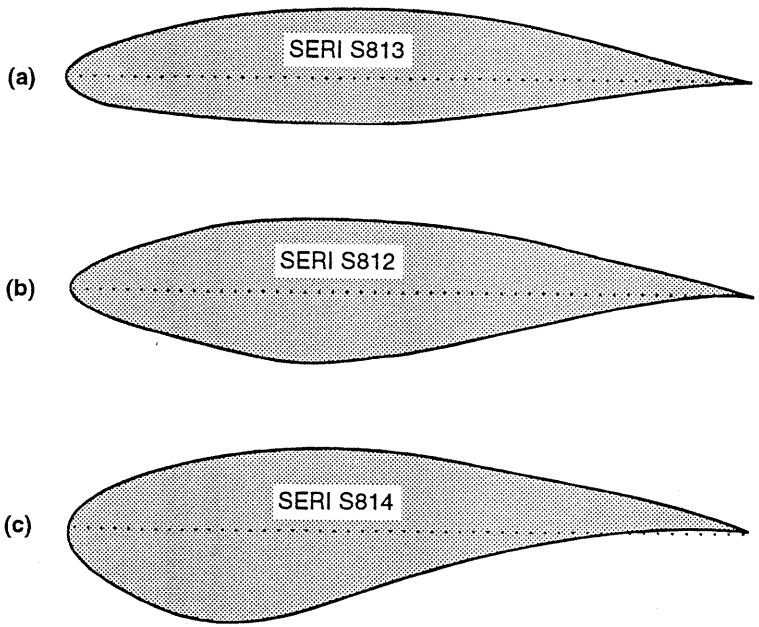

Figure 6-8. Contours of the SERI S812/S813/S814 series of airfoils designed specifically for fixed-pitch HAWTs with diameters from 21 m to 35 m. (a) Tip region ($r/R \approx 0.95$) (b) Primary outboard airfoil ($r/R \approx 0.75$) (c) Root region ($r/R \approx 0.40$) [Tangler 1987, NREL 1994]

Airfoils designed for the root and tip sections must not only address local aerodynamic requirements, but it is also desirable that they produce a monotonic change in aerodynamic properties from root to tip and a "faired" blade surface. The root section should be thicker for structural reasons, and it can accept a higher $C_{L,max}$. The tip section needs to be thinner, with lower values of both minimum drag and $C_{L,max}$. Two airfoil shapes shown in Figure 6-7, the *SERI S807* and *S806A*, have been designed for the root ($r/R \approx 0.40$) and tip ($r/R \approx 0.95$) regions, respectively, to meet these requirements [NREL 1994].

HAWT Rotors 21 m to 35 m in Diameter

It should be noted that designing airfoils specifically for wind turbines may obtain benefits not only by improved aerodynamic performance but also by improved structural performance and lower blade costs. The thickness-to-chord ratio of an airfoil plays a very significant role in its strength and stiffness, and this is particularly important for longer HAWT blades. For this reason, a family of thicker airfoils has been designed for rotors from 21 to 35 m in diameter, on lines similar to those of the SERI S805A/806A/807 family, with the designations *S812, S813,* and *S814* (Fig. 6-8). The thickness-to-chord ratio of the S812 is 0.210, compared to 0.135 for the S805A. Wind tunnel tests confirm that these thicker airfoils also have a limited $C_{L,max}$ (in the range of 1.00) which is insensitive to surface roughness, and low drag. The latter is accomplished by maintaining large areas of *laminar flow*.

Figure 6-9 shows a third set of airfoils designed for HAWTs with diameters of 36 m and larger, tailored for an optimum combination of aerodynamic performance and strength. These are designated as *S816, S817,* and *S818* airfoils [NREL 1994].

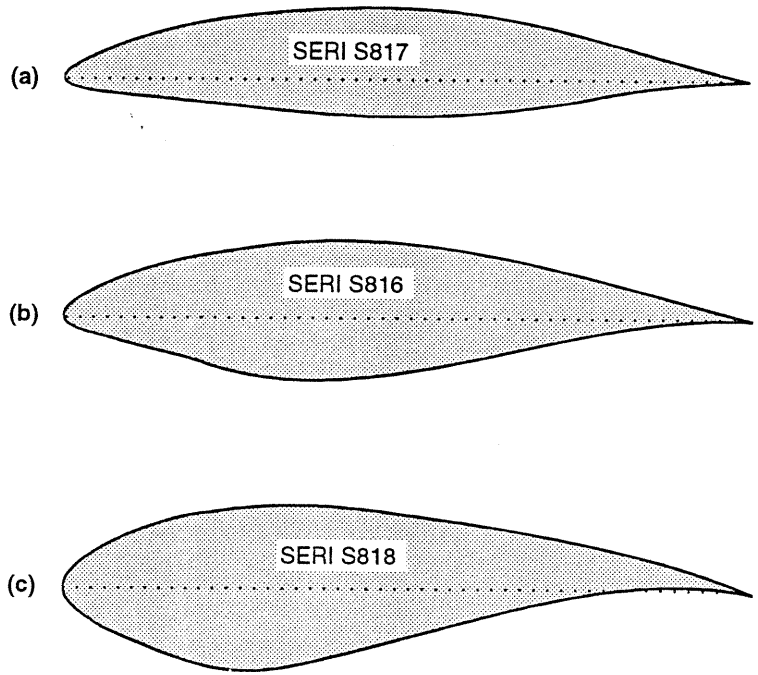

Figure 6-9. Contours of the SERI series of airfoils designed specifically for fixed-pitch HAWTs 36 m in diameter and larger. (a) Tip region ($r/R \approx 0.95$) (b) Primary outboard airfoil ($r/R \approx 0.75$) (c) Root region ($r/R \approx 0.40$) [NREL 1994]

Field Performance Testing of Wind Turbine Airfoils

While idealized, two-dimensional wind tunnel tests are necessary for developing airfoil contours and obtaining lift and drag data with which to predict rotor power output, final evaluation of a wind turbine airfoil must be made on the basis of full-scale field performance tests. Only in the field can the combined effects of spatial and temporal turbulence, variability in steady wind speed, airfoil rotation, hub/tip losses, surface roughness, and manufacturing tolerances be measured. Of course, the variability of the wind complicates the testing, and airfoil-to-airfoil comparisons are more difficult to make. Standardized procedures have therefore been developed for the purpose of increasing the reliability and reducing the uncertainty in field tests of wind turbine performance, emphasizing *power curves* [AWEA 1988] and *energy output* [ASME 1988].

Comparative Power Performance

As an example of a field test conducted to obtain comparative power curves, let us examine the side-by-side performance tests conducted on two stall-controlled, three-bladed rotors installed on identical medium-scale turbines [Tangler *et al.* 1990]. The wind turbines in these tests were *Micon 65/13* HAWTs, rated at 65 kW. One turbine had its original-equipment *Aerostar* blades, with NACA 4415-24 airfoils (Fig. 6-6) and the planform shown in Figure 6-10(a). Candidate replacement blades on the second turbine [Jackson and Migliore 1987] utilize the SERI airfoils in Figure 6-7, and their planform is shown in Figure 6-10(b). Table 6-2 lists comparative data for the two sets of blades. The restrained $C_{L,max}$ in the tip region of the SERI blade permits the length extension and allows the use of 14% more swept area for the same generator rating.

With respect to the prevailing wind at the site, the test turbines had a crosswind spacing of 2.2 diameters, and a meteorological tower with an anemometer at hub height was located 2.0 diameters upwind. Based on the relative positions of the anemometer and the test rotors, data were collected at a sampling rate of 1 Hz, and then averaged for 30 sec, in compliance with standard procedures [AWEA 1988]. Both clean and "dirty" blades were tested. Dirty blade roughness was simulated by strips of tape on upper and lower surfaces near the leading edge. Over 100 hours of operational data were collected for each cleanliness condition, which is a typical duration for a reliable performance test.

The results of these comparative power performance tests are shown graphically by the power curves in Figures 6-11 and 6-12. The significant performance improvements exhibited by the SERI blades compared to the Aerostar blades are attributed to the following three factors, in the order of their relative contributions [Tangler *et al.* 1990]:

- -- larger swept area of the SERI blades allowed by their restrained $C_{L,max}$;
- -- less sensitivity of $C_{L,max}$ to leading-edge roughness in the outboard SERI airfoils;
- -- improved aerodynamic performance at low and moderate wind speeds of the inboard SERI airfoils.

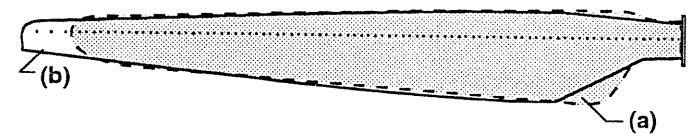

Figure 6-10. Planforms of two blade designs used in comparative field performance tests on *Micon 65/13* HAWTs. (a) Original-equipment *Aerostar* blade with *NACA 4415-24* airfoils (b) Candidate replacement blade with *SERI* airfoils [Tangler *et al.* 1990]

Table 6-2. Blade Data for Side-by-Side Performance Tests on a Micon 65/13 HAWT [Tangler *et al.* 1990]

Parameter	Original Blade	SERI Blade
Rotor diameter	16.0 m	17.0 m
Blade length	7.41 m	7.96 m
Planform area	5.97 m^2	6.17 m^2
Airfoil sections:		
Tip	NACA 4415	S806A
3/4 span		S805A
Root	NACA 4424	S807
Pitch angle	4.2 deg	0.5 deg
Tilt angle	4 deg	4 deg
Cone angle	4 deg	4 deg
Blade material	GFRP	GFRP
Blade weight	3.6 to 3.8 kN	2.8 kN
Natural frequencies:		
1st flapwise	4.05 hz	3.16 hz
1st edgewise	5.80 hz	7.20 hz
Rotor speed	48 rpm	48 rpm

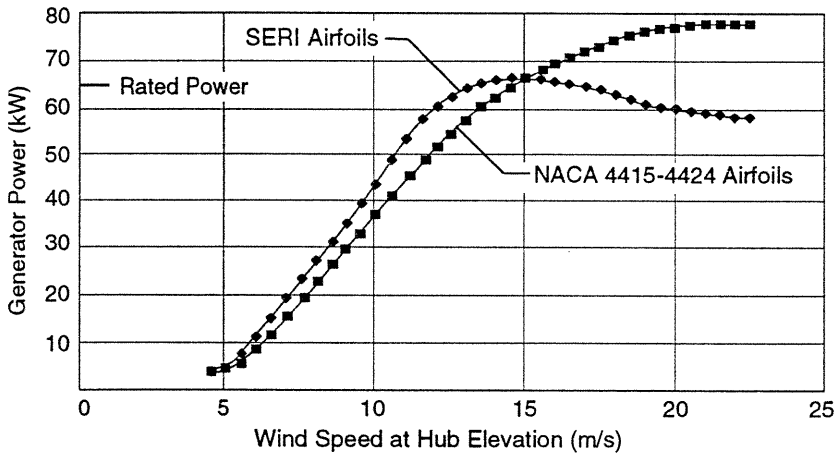

Figure 6-11. Power curves from field tests of clean blades. [Tangler *et al.* 1990]

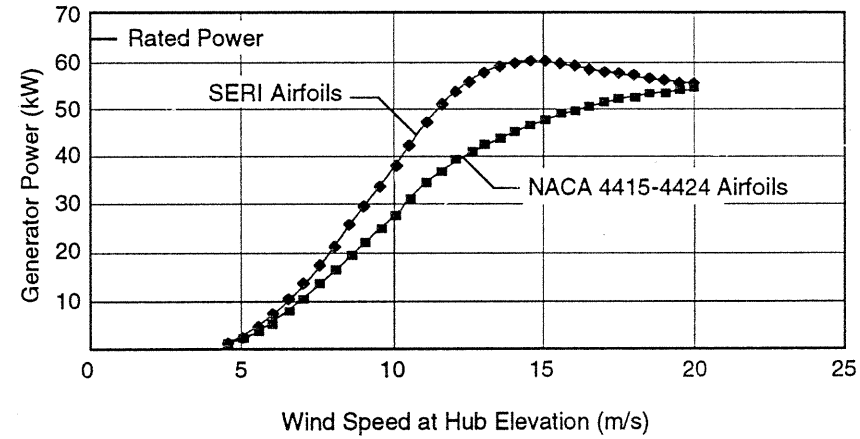

Figure 6-12. Power curves from field tests of dirty blades. [Tangler *et al.* 1990]

Comparative Energy Production

Comparative *annual energy outputs* are calculated by combining power curves, such as those in Figures 6-11 and 6-12, with a specified *wind speed histogram*, as illustrated by the example in Table 5-1. Tests on wind turbines conducted in accordance with standardized ASME procedures [ASME 1989] seek to define relative energy production in terms of an *annual energy ratio*, which is the ratio of the annual energy output of the test turbine to that a specified reference energy production. The latter could be a calculated value (*e.g.* during the design phase) or the result of previous tests.

To illustrate performance comparisons on the basis of annual energy ratios, we will assume (1) the clean original rotor is our reference, and (2) the annual wind speed histogram has a *Weibull distribution* with parameters $C = 8.51$ m/s and $k = 2.48$. The latter are taken from Table 2-1 for an elevation of 25 m, the entry nearest the 23-m hub elevation of the Micon 65/13 HAWTs. Table 6-3 lists the results of annual energy calculations obtained using this wind histogram and the power curves in Figures 6-12 and 6-13.

Table 6-3. Sample Comparative Annual Energy Ratios

Test Rotor Configuration	Gross Annual Energy Output [1] (MWh/y)	Annual Energy Ratio
Original: Clean	194	1.00
Original: Dirty	139	0.72
SERI: Clean	225	1.16
SERI: Dirty	184	0.95

[1] 7.54 m/s mean wind speed at hub elevation, with a Weibull wind speed distribution

The relative energy productions of the two rotors will depend on site conditions, such as the rate of blade soiling by dirt and insects and the frequency of washing. For example, is we assume that the clean condition is present 40% of the time and the dirty condition 60%, a rotor with SERI blades can be expected to produce about 24% more energy under the specified wind regime. This is calculated using the annual energy ratios in Table 6-3, as follows:

$$\frac{SERI\text{-}Rotor\ Energy}{Original\text{-}Rotor\ Energy} = \frac{0.40\,x\,1.16 + 0.60\,x\,0.95}{0.40\,x\,1.00 + 0.60\,x\,0.72} = 1.24 \qquad (6\text{-}6)$$

Actual field test comparisons in Tehachapi and San Gorgonio wind power stations in California have demonstrated improvements in annual energy output from 25% to 30% [Tangler 1993]. In addition to the improvements calculated in accordance with the annual energy ratios in Table 6-3, the SERI airfoils produce more energy because of easier startup of the turbine and longer run times in low winds. These are additional benefits of the lower sensitivity of the SERI airfoils to roughness. At a site with a low annual average wind speed, improvements in annual energy output as high as 40% have been projected.

Tip Shapes of HAWT Blades

One of the many distinctions between HAWT and VAWT blades is that the former have a tip whose effects on lift and drag forces must be taken into account. Two fundamental fluid-dynamic effects occur here. One is the purely *inviscid* effect of the termination of the lifting *vorticity*. This results in a shedding of vorticity near the tip which causes a streamwise vorticity sheet of high intensity in the vicinity of the tip. This inviscid effect modifies the induced *downwash field* in this region. The second effect is a viscous one associated with the highly three-dimensional flow around the tip. Normally, the inviscid and viscous effects interact, with the trailing vortex system inducing flow around the tip while flow separation near the tip (resulting from blade separation) may change the tip air loading and hence affect the trailing vorticity.

These effects in planar wings have been studied extensively. Many wing-tip shapes have been tested in attempts to improve aerodynamic performance, and advantages have been claimed for a number of these. Studies of tip shapes for HAWT rotors have also been made, dating back at least to those that resulted in the semi-circular tapered tips on the

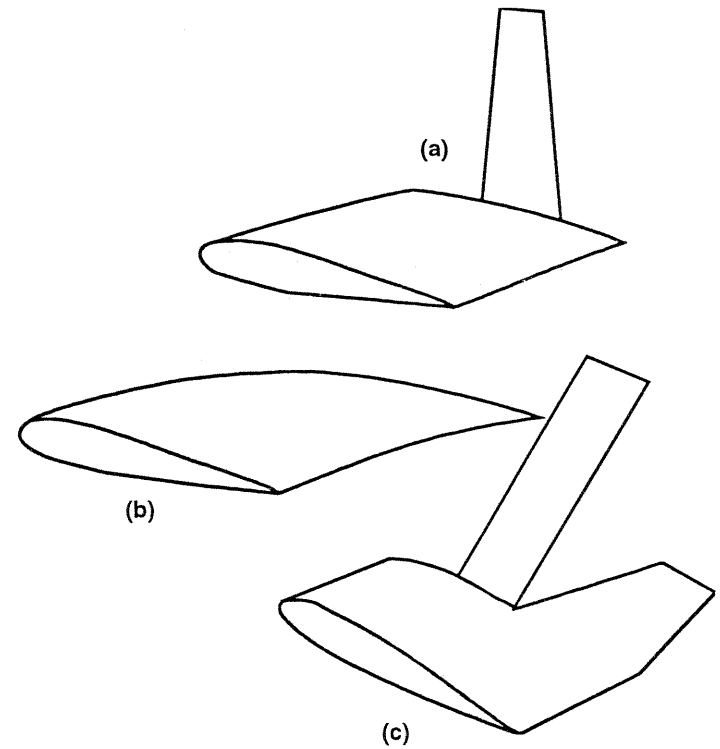

Figure 6-13. Experimental tip devices for improving HAWT rotor performance. (a) Single winglet (b) Shark's fin (c) Double winglet [Gyatt and Lissaman 1985]

pioneering *Gedser HAWT* (Fig. 3-1). A more-recent theoretical study [VanKuik 1986] indicates that tip effects are much more pronounced on wind turbine rotors than on airplane wings and suggests that modifications to HAWT performance models are required.

Gyatt and Lissaman [1985] report field tests on a number of tip shapes intended to improve performance by controlling the shedding of the tip vortex. The test configurations are shown in Figure 6-13 and include one planar swept-back tip and two non-planar tip geometries. These shapes were selected based their promising performance on planar wings, as determined by wind tunnel tests, flight tests, and analytical predictions.

The leading edge of the single winglet, Figure 6-13(a), was positioned normal to the chord plane of the blade on the low-pressure (downwind) side. The "shark's fin," Figure 6-13(b), is a planar tip with a strongly curved leading edge and a swept-back trailing edge. The double winglet, Figure 6-13(c), has two inclined surfaces, with the forward element mounted approximately in a plane at 45 deg to the plane of the blade and the aft element in the plane of the blade. As in the case of the single winglet, the double winglets extended above the low-pressure surface of the main blade.

Comparative performance tests, with and without these tip devices, were conducted on a two-bladed commercial HAWT, 10 m in diameter. Each of the tip devices replaced a length of blade equal to approximately 5% of the rotor radius, so the swept area remained constant during these tests. Modest performance improvements of the order of 3% were predicted for these tips, using the best available non-planar aerodynamic model. However, a small but significant reduction in power of about 3% to 6% was measured. While the theoretical improvement may still be achievable by proper adjustment of the non-planar elements, these tip devices do not appear promising for significantly increasing the power of a HAWT rotor.

Figure 6-14 illustrates a tip shape that has been found to be more desirable for HAWT blades [Tangler 1993]. Its characteristics are

- -- *rounded leading-edge corner*, to eliminate the start of separation caused by large, three-dimensional adverse pressure gradients at a sharp corner;
- -- *finite tip chord* (approx. *c*/2), to maintain a good Reynolds number and lift-to-drag ratio at the tip;
- -- *straight trailing edge*, to provide a pitching moment that is dynamically stable (*i.e.* nose-down).

This tip shape has been used successfully on SERI airfoil blades (Fig. 6-10(b)), both thin and thick.

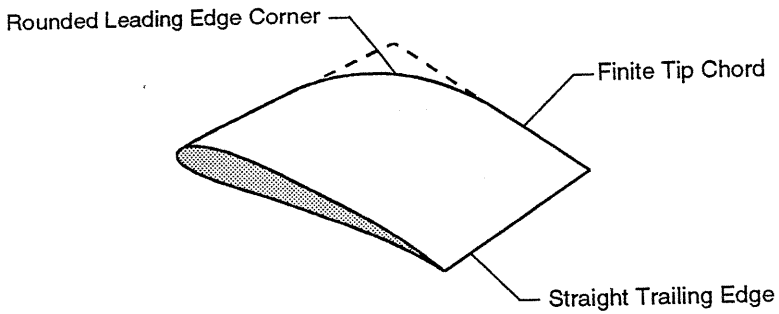

Figure 6-14. Aerodynamically desirable tip shape for a HAWT blade. [Tangler 1993]

Wind Turbine Wake Effects

Modern *wind power stations* consist of numbers of individual turbines arranged on a given site so as to best utilize the local wind energy. This appears to call for the placement of most of the units at the locations of strongest flow. However, such concentrations of turbines will cause shielding of neighboring units, so that downwind turbines are exposed to a lower wind speed. Clearly, the station designer is seeking an optimal situation, in which the most energetic regions of the site are exploited without crowding these desirable areas with so many units that *array interference* (or *wake interference*) prevents them from achieving the best energy capture. It has also been suggested that, in complex terrain, turbines on upwind slopes or near crests of hills and ridges may actually precipitate separation in the lee flow, significantly lowering the surface wind energy on the downwind slope and causing even larger wake deficits.

The extent of the loss due to array interference can be a significant factor in the economics of a wind power station. A representative picture of the loss situation for a 6x6 array of wind turbines is shown in Figure 6-15 [Lissaman and Zalay 1982]. In this hypothetical example, 36 turbines are arranged in a rectangular grid pattern, spaced 10 diameters apart in the direction of the prevailing wind and at various crosswind distances. An important parameter in determining the severity of wake effects on downwind machines is the *ambient turbulence intensity* of the wind, σ_0/U, which will be discussed later. Figure 6-15 gives the total array energy loss as a function of turbulence and crosswind spacing,

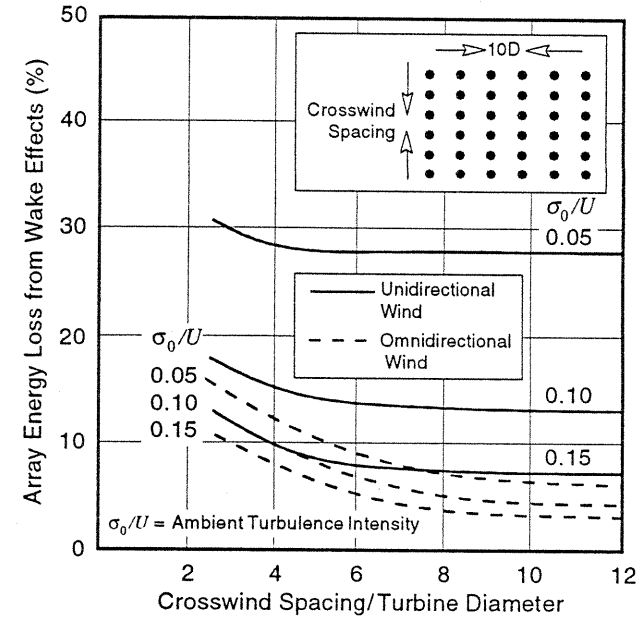

Figure 6-15. General effect of spacing and ambient turbulence intensity on the wake energy losses in an array of wind turbines on flat ground. [Lissaman and Zalay 1982]

as calculated for two wind regimes: all winds from the prevailing direction, and wind flow equally distributed in all directions.

For a typical case, $\sigma/U = 0.15$ and the crosswind spacing is 3 diameters, which gives a wake loss estimate of 10% to 12% for this idealized array. As shown in Figure 4-26, extensive field experience in California wind power stations indicates that array losses are typically about 10%, but can vary from 2% to as much as 30% depending on the terrain, the concentration of turbines, and the wind turbulence.

Another factor is introduced by array interference which can be as significant as the direct energy loss, although it is less quantifiable. This is the extra turbulence generated by upwind rotors, which will increase the turbulence to which downwind units are exposed [*e.g.*, Kelley 1989]. This so-called *generated turbulence* can affect the operation of a downwind turbine by reducing its fatigue life, increasing the probability of catastrophic failure caused by strong gusts, and by exciting blade vibrations and unfavorable control system responses. This is likely to increase the operating and maintenance costs of these machines and possibly cause premature wear-out and/or failure.

Physical Factors Controlling Wake Interference

It is clear that the dominant parameters are the *downwind distance* between units (usually defined in terms of turbine diameters and normally between 6*D* and 12*D*), the amount of *power extracted* from the wind stream by the turbine units (defined in terms of the power coefficient and normally about 0.40, maximum) and the *turbulence* in the wind stream (both ambient and generated). The qualitative effects of these parameters are described below.

Downwind Spacing

Close spacing is always undesirable, but this must be viewed in the context of increasing the total energy production of the site and utilizing the directional nature of seasonal wind patterns. Optimized spacing may call for arrays that are not orthogonally symmetrical, but possess orientation with respect to both prevailing and local wind conditions. Typically, the principal energetic flows are from a prevailing direction, so that an average crosswind direction can be defined from which energetic flows are quite rare. This permits closer spacing crosswind than downwind, as pictured in Figure 4-1.

Power Extracted

The higher the output of a turbine, expressed in terms of its power coefficient, the greater is the downstream wake interference. Interference, as a percent of potential energy production, is approximately independent of wind speed, provided the wind is not very strong or light. In the case of very strong winds (above the turbine's rated speed), upwind turbines operating at rated power will be shedding excess wind power by stall or pitch control. This in turn reduces rotor thrust and the *axial induction factor* (see Chapter 5), so the retarded speed in the wake may still exceed rated speed. Thus downwind units will also operate at rated power, and there will be no array loss. For very light winds, modest axial inductions will retard the wake speed enough so that downwind units will experience winds below the *cut-in speed* and will not operate. In this case, the interference percentage will be very large.

Turbulence Intensity

Turbulence intensity is a measure of the relative unsteadiness of the wind, defined as follows:

$$\sigma/U = \frac{\sigma_0 + \sigma_G}{U} \tag{6-7a}$$

$$\sigma_0 = RMS(u - U) \tag{6-7b}$$

where

σ/U = turbulence intensity
σ_0 = ambient turbulence (m/s)
σ_G = turbulence generated by the rotor (m/s)
$RMS(\ )$ = root-mean-square of ( ) during a given time interval (typically 6 to 12 min)
u = instantaneous free-stream wind speed (m/s)
U = steady (mean) free-stream wind speed during the time interval (m/s)

Ambient turbulence is normally about 0.12 U. Generated turbulence within the first few diameters of distance downstream of a turbine is normally about 0.08 U .

Turbulence causes two opposing effects on the amount of wake interference. It tends to increase *entrainment* of air from the free stream surrounding the wake, thus re-energizing the wake and reducing the *velocity deficit*. At the same time turbulence increases the wake diameter, which causes a given turbine to affect more downwind units. Thus, turbulence spreads the energy loss over a wider area. As shown in Figure 6-15, array energy losses generally decrease with increasing turbulence intensity, indicating that the positive re-energizing effect is dominant. At the same time, however, fatigue loads increase with increasing turbulence.

Atmospheric Stability

Recent research has shown that *atmospheric stability* (see Chapter 8) may be a major parameter in the determination of wake size and structure [Kelley 1994]. Atmospheric stability controls the size of *eddies* within the general wind flow, and therefore the rate of entrainment of air from the free stream and diffusion of turbulence in the wake.

Effect of Turbine Configuration

The description presented so far of wake effects indicates that the interference of a given wind turbine is essentially a consequence of its global or external fluid mechanics and is thus not strongly dependent on the details of the turbine design. This can also be inferred by noting that the principal wake effects continue to be experienced 10 or more diameters downwind of a rotor. At this distance the rotor wake has started to develop the general structure common to all deficit wakes. Although there do appear to be some small distinctions (*e.g.*, in the amount of *generated turbulence*), we need not distinguish between HAWTs and VAWTs. Instead, we can discuss wake interference as a general phenomenon.

Development of Wind Turbine Wake Models

The earliest work on modeling wake interference appears to be by Templin [1974]. This was followed by a paper by Craaford [1975], who handled the subject by considering the effect of the turbines as equivalent to a *ground surface roughness* and estimating the flow retardation in the boundary layer caused by this effect. This approach gives a powerful overview with interesting global results, but it does not provide enough detail of the wake structure for use in the practical design of wind power stations.

Currently, there are three general types of wake models, which are described in detail by Luken and Vermeulen [1986]. The first is the *semi-empirical type* [Lissaman and Bate 1976]. Here a simple analytical relation is used to establish an invariant for the fundamental wake scales of speed and radius. Experimental data are used for modeling the flow profiles in various regions of the wake, and an empirical wake growth rate is used that depends on turbulence. The second type of model [Ainslie 1985] utilizes an axisymmetric boundary-layer *approximation of the Navier-Stokes equations*, with an eddy viscosity model to determine shear stress. Finally, a *full mixing length/eddy viscosity* (K,E) model [Crespo *et al.* 1985] is an advanced type that takes into account surface roughness as well as atmospheric stability. While this last procedure is valuable for analytical research, it is too complicated for design purposes. Various approximations are employed in all three types of models to reduce computer demands.

At the other end of the spectrum from the K,E model is an extremely simple analysis developed by Katic *et al.* [1986]. In spite of its simplicity, wind tunnel tests of a cluster of 37 model turbines indicate that its predictions are as accurate as those made with more-complex models. As noted by these authors, good correlation between model predictions and array test data is a consequence of satisfying the *conservation of wake momentum*, which is the dominant invariant. Overall, a semi-empirical model contains practical manifestations of all the significant fluid mechanic phenomena and can be used for arrays of up to 500 turbines without excessive computer time. Therefore, the basic principles of wake modeling will be discussed using the semi-empirical approach.

Fluid-Dynamic Principles

Considering the turbine to be an *actuator disk*, we note that it essentially removes *total head* from the wind stream in the form of a pressure drop across the rotor disk. Because there is no means of establishing the strong flow curvature required to maintain a pressure difference between the wake and the surrounding free stream, the flow returns very rapidly to the ambient static pressure. As a consequence, the loss of head is manifested in a reduction in speed a short distance downwind of the disk. This is the so-called *velocity deficit*. Standard turbine theory operates under the implied assumption that this deficit extends unchanged from the disk to infinitely far downwind, which is known as the *Trefftz plane concept* (Fig. 5-7). This concept is not adequate for determining flow details in the wake itself, so we will construct a scheme for modeling the wake development downwind.

First, we define the wake as that portion of the flow that has a total head different from the free stream. Because the wake velocity deficit exists within the free stream, there is the characteristic axisymmetric *shear layer* between them, with turbulent transfer tending to reduce velocity differences across the layer. As a consequence, the more-energetic free stream is entrained into the wake. This increases both the mass flow and the total energy in the wake. The net result is an asymptotic return of the wake flow to the undisturbed conditions. However, since the flow in the wake just downwind of the rotor was of lower energy, this return to the free stream state can occur only when the mass of air that passed

through the disk has been infinitely diluted, or when the wake has grown to an infinite diameter with a negligible velocity deficit. It is important to establish an *invariant* for this process, noting that neither mass nor energy flux is conserved in the wake.

If one considers the situation of a single turbine in a uniform flow on flat terrain, it can be seen that the thrust of the rotor must be manifest in the wake, assuming that the turbulent skin friction on the ground plane is not greatly affected by the wake flow. The thrust is equal to the rate of change of the momentum deficit in the wake, or

$$T = \frac{d}{dt}\left[2\pi\rho \int_0^{\infty} (U - V)\, dx\, r\, dr \right] = 2\pi\rho \int_0^{R_w} (U - V)\, V\, r\, dr \qquad (6\text{-}8)$$

where

T = rotor thrust force (N)
$r\,x$ = radial and downwind coordinates measured from the rotor center (m)
U = free stream wind speed at the elevation of the rotor center (m/s)
V = local velocity in the wake; function of the radial coordinate r (m/s)
R_W = effective radius of the wake (m)

Equation (6-8) can be recognized as the general form of Equation (5-9). Any effect of the ground in creating a non-axisymmetric wake has been neglected here and will be accounted for later. Equation (6-8) provides the basic conservation law for the wake development. We now require a "shape" law to define the velocity profile $V = V(r)$ and a "scale" law that will define the effective wake radius, R_W.

Wake Geometry Models

It has been observed that wind turbine wakes develop according to several fairly-well defined regimes at different downwind distances, and these can be idealized as shown in Figure 6-16. First, there is the flow emerging from the rotor disk itself at section *A*. For well-designed blades, air loading produces an almost uniform velocity deficit, removing the same energy at all radii. The wake velocity is assumed to be constant across this section and equal to $(1 - a)U$, where, as before, a is the axial induction factor. The initial wake is considered to behave like an inviscid slug of uniformly-reduced velocity submerged in an outer flow, forming a so-called *co-flowing jet* or *potential core*.

Proceeding downwind from the rotor to section *B*, the velocity deficit profile is "top hat" shaped, and an intense shear layer is developed, attenuating the velocity discontinuity. It is assumed that this shear layer extends itself outward and inward until the inviscid core region is eliminated at section *C*. The wake from *A* to *C* is defined as being in the *initial potential core regime*.

Farther downwind at section *D*, it is assumed that the wake has adopted its asymptotic "bell-shaped" profile, like the radial velocity distribution far downstream of a body of revolution. This is the beginning of the *fully-developed wake regime*. The profile of the wake at *C*, where the shear layer has penetrated to the flow center line, is not the same as the far-wake profile at *D*, so it is necessary to assume that there is a *transitional regime* of a certain streamwise extent that joins these two sections. It now remains to establish simple analytical models for intermediate wake profiles, between the rotor and far downwind, and the transitions from one to another [Lissaman 1976, 1979].

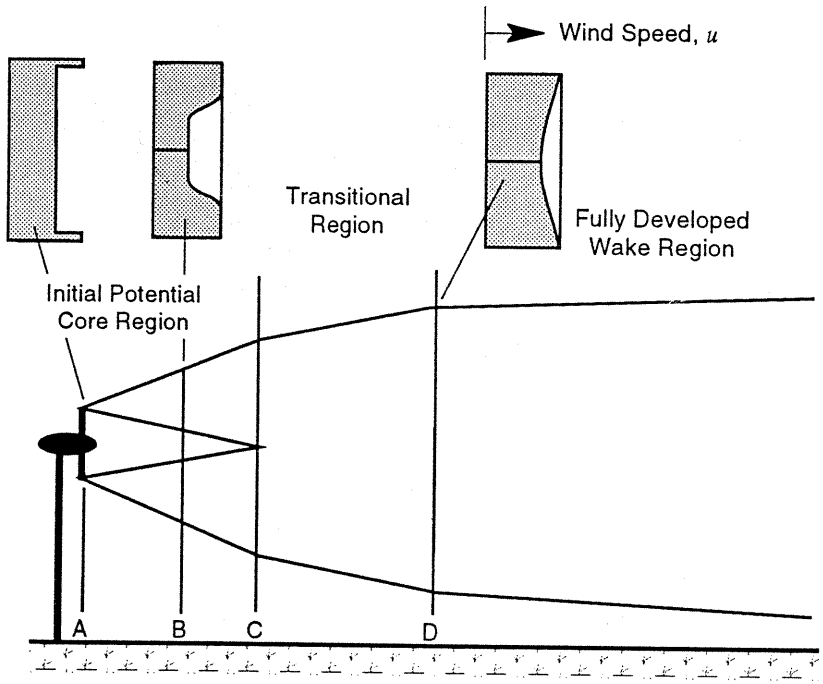

Figure 6-16. Regimes of wake development and associated radial profiles of the velocity deficit.

Initial Potential Core Regime

In this regime, it is assumed that the shear layer, having a profile given by a standard radially-symmetric shear layer model, develops according to the normal shear law where the growth rate of a layer thickness is proportional to the speed difference across it. This will define a profile shape for any downwind station in the regime. The basic conservation of drag is then maintained by selecting the effective radius in Equation (6-8), R_W, to conserve the momentum deficit in the wake. Axisymmetric shear layers like this are shown in Abramovitch [1963] and referenced in Lissaman [1976].

Fully-Developed Wake Regime

A suitable model for the flow profile in the far wake, well-supported by experimental results, is also provided by Abramovitch [1963]. This profile is expressed as a function of radial distance, r, normalized by a radial scale factor. To establish a growth law for the width of the wake in this regime, we assume that the effective wake radius develops temporally and spatially according to the following laws:

$$\frac{dR_W}{dt} = k_W \left(\sigma_0 + \sigma_G \right) \tag{6-9a}$$

$$\frac{dR_W}{dx} = k_W \frac{\sigma_0 + \sigma_G}{U} \tag{6-9b}$$

where k_W = empirical constant

This model produces a turbulent energy level which increases from free stream to a higher level upon passage through the rotor disk, is reinforced by the shear layers immediately downwind of the disk, and then decays to return to the ambient level. Details are given in [Lissaman 1976].

Transitional Regime

The transition law describing flow from the inviscid core to the far wake is based simply on establishing a geometric relationship that will provide a smooth transition from the profile at section *C* to that at section *D* in Figure 6-16.

Ground Effects

A refinement of Equations (6-9) takes into account differences between vertical and lateral ambient turbulence near the ground and accounts for differences in vertical and lateral growth rates. This causes the wake to adopt an elliptical cross-section downwind of its original circular shape. Another ground effect is taken into account by the standard method of *reflection*, so that the actual wake perturbation at a given downwind station now becomes the sum of that in the direct flow and that in the image flow. If the perturbations are linearized, then the thrust invariant is now associated with the thrust of the rotor plus its image. Thus, conservation of the integral for a single wake automatically takes into account the ground effect by the presence of the image perturbation. In other words, the momentum defect "removed" by the ground is "restored" by the addition to the actual wake of the ground perturbation flow of the image.

Integration of Wakes for Array Effect

In most models it is assumed that the wakes of an array of turbines may be directly superimposed. This is a linearizing assumption, based on the physical fact that the wake perturbations caused by a single turbine are relatively small. Normally, velocity deficits are less than 5% of the free-stream velocity by a distance of five diameters downwind of a rotor. Thus it is a good approximation to disregard any interaction between wakes.

The normal procedure for calculating the wake interference for a given array of turbines is therefore straightforward and as follows: For the given wind azimuth the most-upwind unit is selected, and its wake geometry and velocity deficits are calculated for a specified wind speed and turbulence intensity, progressing downwind through the array. The deficit at each turbine is tabulated. Turbine control parameters (such as cut-in and rated wind speeds) may be introduced into the model, as well as different rotor areas and elevations. Then the most-upwind of the remaining turbines is selected and its inflow velocity determined. In general, this will be the vector sum of the free-stream flow and the wake

velocity deficit of the leading upwind turbine. The development of the wake of the second unit is then calculated and its velocity deficits at the locations of all other units determined. These are tabulated with the wake deficits from the most-upwind turbine.

This procedure is repeated until the most-downwind turbine has been reached, and results in the power output of the array for a given combination of wind azimuth, speed, and turbulence. The calculation must be repeated for differing azimuths (to account for the annual distribution of wind directions), wind speeds (to account for the annual wind speed histogram and turbine control characteristics), and ambient turbulence levels (to account for the varying wake expansion). Conceptually, this procedure provides the performance of all the turbines in the entire array viewed as a single wind power system. Output power of the array will be defined as a function of wind speed and turbulence, as it is for a single turbine. Unlike a single turbine, array output power is also a function of wind direction and speed variations across the site, taking into account the array geometry and terrain features.

Repeating this process for each wind azimuth, speed, and turbulence level is a formidable (but not complicated) computational task. The problem of completing the computation for an array within a reasonable time indicates the merits of a simple, linearized physical wake model like the one described. It is believed that models with more fundamental fluid-dynamic features, using more complex rational turbulence models, and employing finite difference techniques would be prohibitively complex for analyzing an array of practical size. Such models can, however, be used to validate the simple wake model for the case of a single turbine and assist in determining any empirical constants.

Analytical Results Obtained with Wake Models

Flat Terrain

From the numerous wake-interference calculations which have been made for the case of a uniform flow over flat terrain, it has been found that the level of ambient turbulence has a very large effect on the array energy loss. Typical of the analytical results for simple arrays on flat terrain are those shown in Figure 6-15. In the course of numerical investigations of this type, it has been determined that the wake structure within its first four of five diameters of downwind length does not have a strong effect on its velocity deficit in regions further downwind, where turbines are likely to be located. Thus, the modelling of the initial potential core regime (Fig. 6-16) does not need to be very refined, provided it gives the proper initial state for the fully-developed wake regime.

In the design of a wind power station the normal method is to start with a reasonable layout for the array, maximizing turbine spacing in the principal flow direction at the expense of closer spacing in the crosswind direction. This assumes that the case of wind at right angles to the prevailing wind direction, although involving large losses, does not occur frequently. Next, the initial layout is examined using the wake interference model to identify turbines that have particularly poor production because they are in sheltered positions and to find more favorable locations for these units. Spacing distances are then perturbed until the maximum (or near-maximum) annual energy production is determined. Thus the array design is approximately optimized by an iterative process.

Some effort has been devoted to defining a theoretically-exact, optimal arrangement for simple arrays on flat terrain. Such arrays could not normally be used directly in design, since each site has its own specific distributions of wind speed and direction. However, the value of optimal-spacing studies lies in determining the sensitivity of array energy output to changes in spacing from the theoretical optimum.

Two examples will illustrate the investigation of this sensitivity to spacing. In the first, turbines are placed in a single windwise row, with the constraint that a given number of units has to be placed on a strip of a given length. This is sufficiently simple that a *variational process* can be used to determine an ideal spacing. The optimal distribution is symmetrical about the center of the strip, with the spacing somewhat larger for the units near the center [Lissaman *et al.* 1982]. This implies that increasing the spacing in the center serves to provide a region of re-energization for the flow, a conclusion supported by Kaminsky *et al.* [1987]. The second example is a square array with a constant wind occurring with equal frequency from all directions. An optimal-spacing study of this case also indicates that it is slightly advantageous to have larger spacing in the interior region, with a heavier concentration of the turbines near the periphery of the square.

The most important conclusion from these optimal spacing studies of simple arrays is that uniform spacing gives an array energy output that is only insignificantly less than that for an optimum spacing, for normal spacings in the range of 6 to 10 diameters. Moreover, this energy difference is smaller than the implied accuracy associated with the approximations in the mathematical models. This provides the valuable practical result that a uniform spacing, at least in the prevailing wind direction, is an excellent initial arrangement which can then be optimized to account for the actual site features and wind characteristics.

Complex Terrain

In the case of a non-uniform wind field caused by complex terrain it is not possible to use the basic invariant of the momentum deficit, which is connected to the thrust of the turbine. In complex terrain the thrust in a plane downwind of the turbine is manifested in pressure perturbations on the sloping ground as well as in the velocity profile in the wake. Thus, the momentum deficit in the wake is not conserved for non-uniform flows. To handle this case we will use the concept of *invariance of the total energy* in the flow after dissipative losses due to entrainment have been taken into account [Lissaman *et al.* 1986].

If there were no losses, as the flow moves into areas of different pressure the wake speed would change in accordance with the *Bernoulli equation* connecting fluid speed and pressure. However, entrainment causes dissipation losses in total head, so that speed cannot be connected to pressure alone. As a first approximation, it can be assumed that dissipation (which is a function of shear gradients and flow distortion) is the same for non-uniform and uniform flows. Thus, our modeling approach for varying ambient pressure is to take the wake field which would exist over flat terrain, calculate the dissipation for this constant-pressure case, and then apply this dissipation to the wake flow speed at each turbine location on complex terrain, the varying pressure case.

For example, consider identical turbines at the two sites shown in Figure 6-17, where site (a) is flat and site (b) has complex terrain. The wake velocities can be expressed as

$$V_f = U_f(1 - d_f) \tag{6-10a}$$

$$V_c = U_c(1 - d_c) \tag{6-10b}$$

where

V_f = wake speed at a given location over flat terrain (m/s)
V_c = wake speed at the same location over complex terrain (m/s)
U_f, U_c = ambient wind speeds for flat and complex terrain, respectively (m/s)
d_f = known wake deficit factor, calculated using flat terrain model
d_c = unknown wake deficit factor for complex terrain

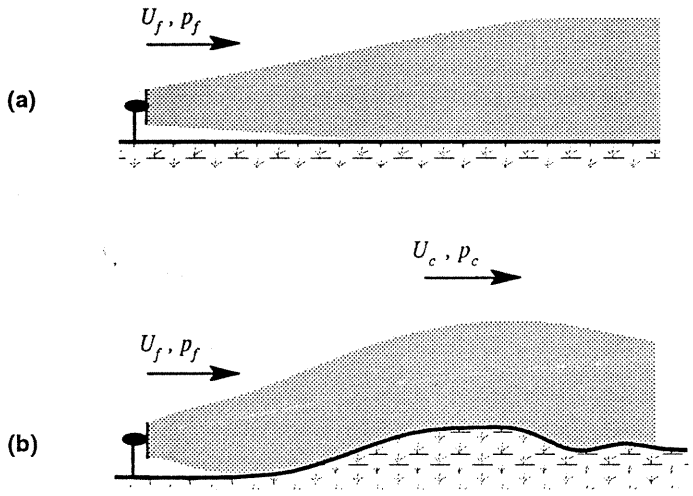

Figure 6-17. Comparison of wake flow conditions over flat and complex terrain. (a) Flat terrain (b) Complex terrain, where the wind speed and static pressure outside the wake are changed by a hill

The total head at the same downwind distance in each site can be written as

$$h_f = p_f + 0.5\rho U_f^2(1 - d_f)^2 \qquad (6\text{-}11a)$$

$$h_c = p_c + 0.5\rho U_c^2(1 - d_c)^2 \qquad (6\text{-}11b)$$

where

h_f , h_c = total head in the wake, for flat and complex terrain, respectively (N/m^2)
p_f , p_c = local static pressure, for flat and complex terrain, respectively (N/m^2)

Now, outside the wake, the wind speeds and static pressures are coupled by the nondissipative Bernoulli equation to give

$$p_f + 0.5\,\rho\,U_f^2 = p_c + 0.5\,\rho\,U_c^2 \qquad (6\text{-}12)$$

If we assume that the dissipation at a given downwind distance is the same for both the flat and complex terrains, then the total head in each wake is also the same, and $h_c = h_f$. This provides a simple result:

$$U_c^2(-2d_c + d_c^2) = U_f^2(-2d_f + d_f^2)$$

which, for small values of d_c and d_f, linearizes to

$$d_c = d_f\left(\frac{U_f}{U_c}\right)^2 \qquad (6\text{-}13)$$

This is an approximation that converges properly for uniform flow with dissipation as well as for non-uniform flow without dissipation, and thus it may be expected to be a reasonable model for the case of non-uniform flow with dissipation.

Measurement of Wake Effects

Wind Tunnel Wake Tests

Wind tunnel tests have been conducted to measure wake deficits behind single turbines. These have established the strong dependence of the wake deficit on the tunnel turbulence, as predicted by the theory expressed in Equations (6-9). They have also shown reasonable correlation with the semi-empirical model in decay law (the functional dependence of deficit with downwind distance) and the actual rate of the decay (the magnitude of the decay constant). A typical example of measured deficits compared with model predictions is shown in Figure 6-18. Both the data and the model indicate that the centerline velocity deficit $(U - V_{min})$ decays at a rate inversely proportional to the downwind distance x. Turbulence intensities in wind tunnels are generally low, even when they are artificially increased by the use of wire grids and boundary layer devices, as was done during these tests. However, it can be seen that even for these low turbulences an increase in the turbulence intensity of only 0.01 significantly increases the wake decay rate.

Because of the difficulty of reproducing the actual nature and scales of the ambient turbulence and other full-scale factors relating to the turbine rotor, the prospects of validating an analytical wake model in a wind tunnel to a higher degree than that shown in Figure 6-18 are quite low.

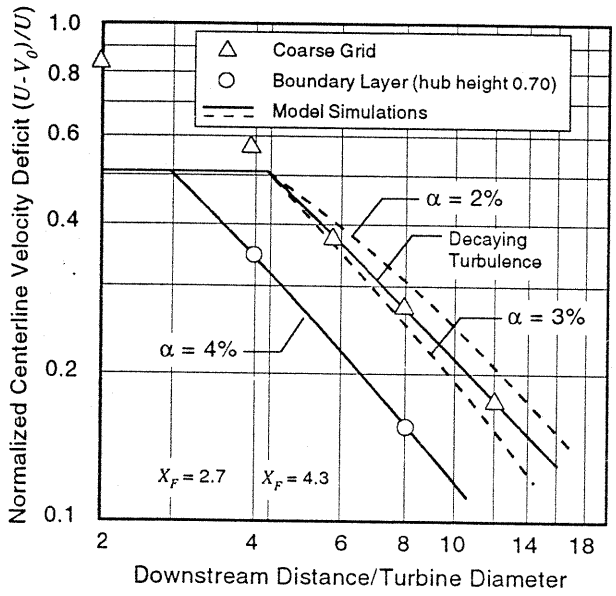

Figure 6-18. Comparison of wind tunnel test data and model predictions of the decay in wake velocity deficit.

Field Tests on a Single Turbine

Comprehensive field tests of the individual factors that cause array interference are extremely difficult to conduct. It is necessary, in principle, to check the different effects separately. These include at least the wake development (velocity deficit, wake radius, and turbulence) downwind of a single turbine as well as the performance of a downwind unit while experiencing wake flow. Further refinements in field testing would include measurements on the wake of one turbine operating within the wake of another. Certain fundamental features of the nature of wind turbine wakes have already been established by full-scale field tests. The results of measurements by Faxen [1978] of the velocity profile behind an operating HAWT are shown in Figure 6-19 and confirm the expected, approximately *Gaussian* profile of the deficit in the far wake.

We can extract some additional information about HAWT rotor wakes from the data in Figure 6-19 if we integrate the deficit volumes under the two profiles and normalize the results. Table 6-4 lists various parameters obtained by this procedure. We note that the ratios of deficit-to-wind speed are not constant for the two test cases, but increase with increasing power. The normalized parameters that are found to be approximately equal for the two cases are the average-to-centerline deficit ratios (0.28, compared to 0.22 for an ideal Gaussian distribution), and the deficit-to-power density ratios. The latter are approximately 0.042 (m/s)/(W/m^2) for the average deficit and 0.0142 (m/s)/(W/m^2) for the maximum.

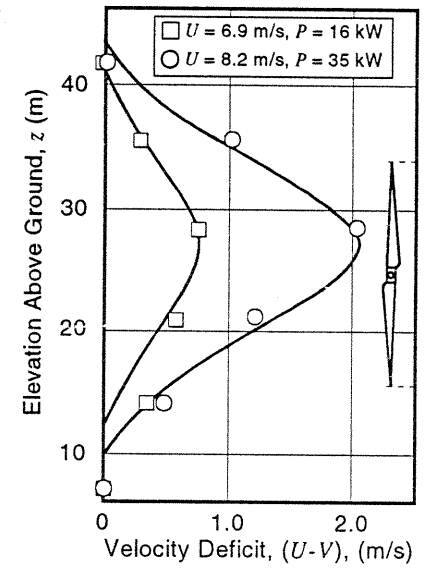

Figure 6-19. Field measurements of the velocity profile downwind of an operating medium-scale HAWT. [Faxen 1978]

Field Tests on Multiple Turbines

Wind speed measurements have been made in the wake of a Mod-2 HAWT (Fig. 3-40) using instruments attached to tethered balloons [Zambrano *et al.* 1982]. Unfortunately, the results of these tests are too scattered to provide definitive corroboration of wake models. To overcome problems with data scatter, the absence of steady-state conditions, and the expected power differences between widely-spaced turbines, Neustadter and Spera [1984] developed an energy method for measuring wake interference losses. In this procedure, the energy output of a test turbine, with and without wake effect, is normalized by the energy output of a nearby control turbine during the same test periods. This corrects for changes in the free-stream wind speed prior to calculating interference losses.

The required arrangement of wind turbines is illustrated in Figure 6-20, using the 3-unit Mod-2 HAWT cluster as an example. The test and control turbines (units 1 and 3, respectively) run continuously while the wake-producing turbine (unit 2) is operated intermittently. Test data are the energy production in 10-min segments for the three turbines over a cumulative operating time of 27 hours. Only the time segments during which the wake envelops the test turbine (wind azimuths from 250 to 280 deg in this case) are used. For the 7-diameter downwind spacing of these tests, the energy deficit was found to be 10.4%, which is compatible with model predictions. The equivalent average wind velocity deficit was only 0.3 m/s, which emphasizes the difficulties of measuring instantaneous power and wind speed and the advantages of measuring energy output.

Table 6-4. Wake Deficit Parameters Derived from HAWT Field Test Profiles
[data from Faxen 1978]

Parameter	Test No. 1	Test No. 2
Turbine:		
Free-stream wind speed (m/s)	6.9	8.2
Power output (kW)	16	35
Power density [1] (W/m^2)	60	132
Wake:		
Wake-to-rotor area ratio	≈ 4.0	≈ 4.0
Centerline velocity deficit (m/s)	0.84	2.09
Average velocity deficit (m/s)	0.23	0.58
Normalized Wake:		
Deficit-to-free stream wind speed ratios		
Centerline	0.122	0.255
Average	0.034	0.071
Average-to-centerline deficit ratio	0.28	0.28
Deficit-to-power density ratios		
Centerline $(m/s)/(W/m^2)$	0.0139	0.0155
Average $(m/s)/(W/m^2)$	0.0039	0.0044

[1] Rotor swept area = 270 m^3

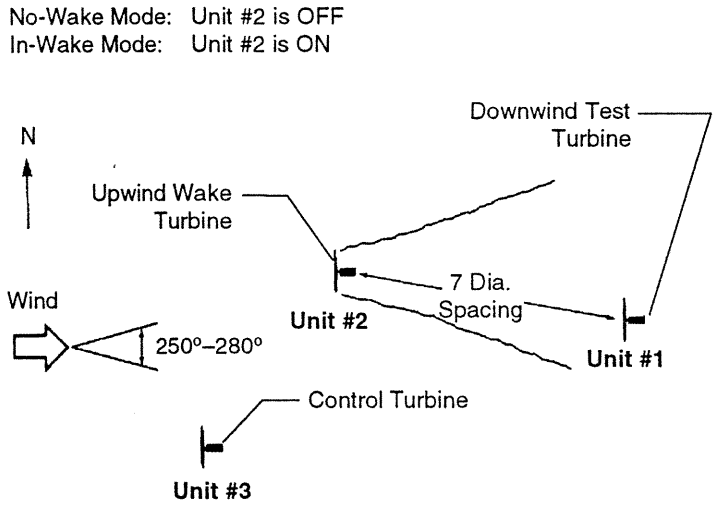

Figure 6-20. Schematic plan view of the Mod-2 HAWT test site near Goldendale, Washington, during wake effect tests using an energy method. Unit 2 is operated intermittently to change the energy output of Unit 1. Energy output of Unit 3 is used as a control, to eliminate wind variability effects. [Neustadter and Spera 1984]

Summary Comments on Wind Turbine Wake Effects

As the demand for wind turbine installations increases and the availability of large sites with high energy flow decreases, it will be necessary to employ arrays of higher density in the good wind areas as well as to install arrays on sites with lower wind speeds. In both cases, an understanding of array effects is critical to maximizing energy production. Since 1976 there has been an extensive research effort devoted to predicting wake interference effects. For uniform flows corresponding to flat terrain, the numerical modeling has reached an adequate state, particularly with semi-empirical models in which constants may be adjusted to conform with the accumulating data base.

For non-uniform flows, however, the situation is still relatively unquantified. Reliable wake-effect data are still needed from commercial wind power stations located in complex terrain. It is noted that modeling the array interference in this case must be based on an adequate modeling of the wind flow itself over complex terrain, and this topic is generally considered to be incompletely understood. One must have an acceptable wind flow model without wind turbines before one can reliably superimpose the turbine array effects. Simple approximate models for wake interference are probably as accurate as the complex-terrain flow models now available. Refinements are required for both, in order to produce an acceptable operational model for the micrositing of wind turbines.

References

Ainslie, J. F., 1985, "Development of an Eddy-Viscosity Model for Wind Turbine Wakes," *Proceedings, 7th BWEA Conference*, British Wind Energy Association, London: Multi-Science Publishing Co.

Craaford, J., 1975, (personal communication).

Crespo A., F. Manuel, D. Moreno, E. Fraga, and J. Hernandez, 1985, "Numerical Analysis of Wind Turbine Wakes," *Proceedings, Workshop on Wind Energy Application*, Delphi, Greece.

Eppler, R., and K. M. Somers, 1980, *A Computer Program for the Design and Analysis of Low-Speed Airfoils*, NASA TM-80210, Hampton, Virginia: NASA Langley Research Center.

Faxen, T., 1978, "Wake Interaction in an Array of Windmills," *Proceedings, 2nd International Symposium on Wind Energy Systems*, Amsterdam.

Gyatt, G. W., and P. B. S. Lissaman, 1985, *Development and Testing of Tip Devices for Horizontal Axis Wind Turbines*, NASA CR 174991, Cleveland, Ohio: NASA Lewis Research Center.

Hibbs, B. D., 1986, *HAWT Performance with Dynamic Stall*, SERI/STR-217-2732, Golden, Colorado: National Renewable Energy Laboratory.

Jackson, K. L., and P. G. Migliore, 1987, "Design of Wind Turbine Blades Employing Advanced Airfoils," *Proceedings, Wind Power '87 Conference*, SERI/CP-217-3315, Washington, DC: American Wind Energy Association, pp. 106-111.

Jacobs, E. M., and I. H. Abbot, 1932, *The NACA Variable-Density Wind Tunnel*, NACA TR 416, Hampton, Virginia: NASA Langley Research Center.

Katic, I., J. Hojstrup, and N.O. Jensen, 1986, "A Simple Model for Cluster Efficiency," *Proceedings, EWEC '86 Conference*, Rome: European Wind Energy Committee.

Klimas, P. C., 1985, *Tailored Airfoils for Vertical Axis Wind Turbines*, SAND 84-0941, Albuquerque, New Mexico: Sandia National Laboratories.

Lissaman, P. B. S., 1976, *Energy Effectiveness of Arrays of Wind Energy Collection Systems*, Report No. AV-R-6110, Monrovia, CA: AeroVironment, Inc.

Lissaman, P. B. S., A. Zalay, G.W. Gyatt, 1982, "Critical Issues in the Design and Assessment of Wind Turbine Arrays," *Proceedings, 4th International Symposium on Wind Energy Systems*, ISBN 0 906085 772, Stockholm.

Lissaman, P. B. S., D. R. Foster, and B. D. Hibbs, 1986, *Operational Model for the Design of Optimum Wind Farm Arrays*, Report No. AV-FR-86/837, Monrovia, CA: AeroVironment, Inc.

Luken, E., and P. E. J. Vermuelen, 1986, "Development of Advanced Mathematical Models for the Calculation of Wind Turbine Wake-Interaction Effects," *Proceedings, European Wind Energy Conference '86*, Rome.

Lundsager, P., S. Frandsen, and C. J. Christensen, 1980, *Analysis of Data from the Gedser Wind Turbine, 1977-1979*, Risø-M-2242, Roskilde, Denmark: Risø National Laboratory Station for Wind Turbines.

Kelley, N. D., 1989, *An Initial Look at the Dynamics of the Microscale Flow Field within a Large Wind Farm in Response to Variations in the Natural Inflow*, SERI/TP-257-3591, Golden, Colorado: National Renewable Energy Laboratory.

Kelley, N. D., 1994, *The Identification of Inflow Fluid Dynamics Parameters That Can Be Used To Scale Fatigue Loading Spectra of Wind Turbine Structural Components*, NREL/TP-442-6008, Golden, Colorado: National Renewable Energy Laboratory.

Miley, J., 1980, *A Catalog of Low Reynolds Number Airfoil Data for Wind Turbine Applications.*

NREL, 1994, *Catalog of SERI Airfoils Designed For Horizontal-Axis Wind Turbines*, (to be published), Golden, Colorado: National Renewable Energy Laboratory.

Neustadter, H. E., and D. A. Spera, August 1985, "Method for Evaluating Wind Turbine Wake Effects on Wind Farm Performance," *Journal of Solar Energy Engineering*, Vol. 107: pp. 240-243.

Ostowari, C., and D. Naik, 1984, *Post-Stall Wind Turbine Studies of Varying Aspect Ratio Wind Tunnel Blades with NACA 44XX Series Airfoil Sections*, Golden, Colorado: National Renewable Energy Laboratory.

Silverstein, A., 1934, *Scale Effect on Clark Y Airfoil Characteristics from N.A.C.A. Full-Scale Wind Tunnel Tests*, NACA Technical Report No. 502, Hampton, Virginia: NASA Langley Research Center.

Spera, D. A., and D. C. Janetzke, 1981, "Performance and Load Data from Mod-0A and Mod-1 Wind Turbine Generators," *Proceedings, Workshop on Large Horizontal-Axis Wind Turbines*, NASA CP-2230, DOE Publication CONF-810752, Cleveland, OH: NASA Lewis Research Center, pp. 447-467.

Tangler, J. L., and D. M. Somers, 1985, "Advanced Airfoils for HAWTS," *Proceedings, Wind Power '85 Conference*, SERI/CP-217-2902, Washington, DC: American Wind Energy Association, pp. 45-51.

Tangler, J. L., and D. M. Somers, 1986, "A Low Reynolds Number Airfoil Family for Horizontal Axis Wind Turbines," *Proceedings, International Conference on Aerodynamics at Low Reynolds Numbers*, London.

Tangler, J. L., 1987, *Status of Special-Purpose Airfoil Families*, SERI/TP-217-3264, Golden, Colorado: National Renewable Energy Laboratory.

Tangler, J. L., 1993, (personal communication), Golden, Colorado: National Renewable Energy Laboratory.

VanKuik, G. A. M., 1986, "The Physics and Mathematical Description of the Achilles Heel of Stationary Wind Turbine Aerodynamics: The Tip Flow Process," *Proceedings, European Wind Energy Conference '86*, Rome.

Viterna, L. A., and R. D. Corrigan, 1981, "Fixed Pitch Rotor Performance of Large Horizontal Axis Wind Turbines," *Proceedings, Workshop on Large Horizontal Axis Wind Turbines*, NASA CP-2230, DOE Publication CONF-810752, Cleveland, OH: NASA Lewis Research Center, pp. 69-85.

Zambrano, T. G., and G. W. Gyatt, 1982, *Wake Structure Measurements at the Mod-2 Cluster Test Facility at Goodnoe Hills*, Report No. AV-QS-A-82/608, Monrovia, CA: AeroVironment, Inc.